

AD-A154 630

EXPERIMENTS ON THE INFLUENCE OF ACTIVE WALLS ON THE
INITIAL AMPLITUDES AN. (U) SOUTHWEST RESEARCH INST SAN
ANTONIO TX J T PARK ET AL. MAR 85 SWRI-6984

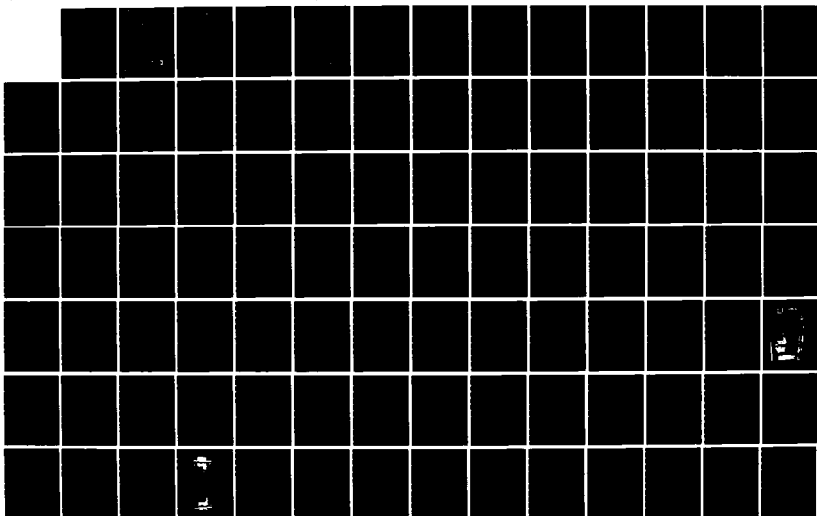
1/2

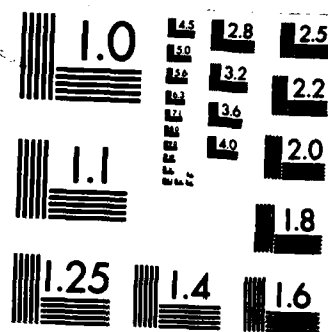
UNCLASSIFIED

N00014-82-C-0199

F/G 20/4

NL





MICROCOPY RESOLUTION TEST CHART
NATIONAL BUREAU OF STANDARDS-1963-A

Report SwRI 6984
Contract N00014-82-C-0198; NR 657-723

2

EXPERIMENTS ON THE INFLUENCE OF ACTIVE WALLS ON THE INITIAL AMPLITUDES AND GROWTHS OF INSTABILITY WAVES

Joel T. Park, H. Stanley Silvas, Jr.,
Steve A. Cerwin, and Harold L. Rogler
Southwest Research Institute
6220 Culebra Road
P.O. Drawer 28510
San Antonio, Texas 78284

March 1985

Final Report for Period 8 February 1982 - 31 January 1985

Approved for public release; distribution unlimited

Prepared for
OFFICE OF NAVAL RESEARCH
800 North Quincy Street
Arlington, Virginia 22217

DTIC
ELECTE
JUN 6 1985
S B D

DTIC FILE COPY

85 4 23 074

REPORT DOCUMENTATION PAGE		READ INSTRUCTIONS BEFORE COMPLETING FORM
1. REPORT NUMBER SwRI 6984	2. GOVT ACCESSION NO. H154 630	3. RECIPIENT'S CATALOG NUMBER
4. TITLE (and Subtitle) EXPERIMENTS ON THE INFLUENCE OF ACTIVE WALLS ON THE INITIAL AMPLITUDES AND GROWTHS OF INSTABILITY WAVES	5. TYPE OF REPORT & PERIOD COVERED 8 Feb 1982 - 31 Jan 1985	
7. AUTHOR(s) Joel T. Park, H. Stanley Silvus, Jr., and Steve A. Cerwin (SwRI) and Harold L. Rogler (United Research Corporation)	6. PERFORMING ORG. REPORT NUMBER	
9. PERFORMING ORGANIZATION NAME AND ADDRESSES Southwest Research Institute 6220 Culebra Road, P. O. Drawer 28510 San Antonio, Texas 78284	8. CONTRACT OR GRANT NUMBER(s) N00014-82-C-0199	
11. CONTROLLING OFFICE NAME AND ADDRESS Office of Naval Research, Code 432 800 North Quincy Street Arlington, Virginia 22217	10. PROGRAM ELEMENT, PROJECT, TASK AREA & WORK UNIT NUMBERS NR 657-723	
14. MONITORING AGENCY NAME & ADDRESS (if different from Controlling Office)	12. REPORT DATE March 1985	
	13. NUMBER OF PAGES 123	
	15. SECURITY CLASS. (of this report) Unclassified	
	15a. DECLASSIFICATION/DOWNGRADING SCHEDULE	
16. DISTRIBUTION STATEMENT (of this Report) Approved for public release; distribution unlimited		
17. DISTRIBUTION STATEMENT (of the abstract entered in Block 20, if different from Report)		
18. SUPPLEMENTARY NOTES Supported by The Office of Naval Research (ONR) under the Compliant Coating Drag Reduction (CCDR) Program		
19. KEY WORDS (Continue on reverse side if necessary and identify by block number) Boundary layer, Displacement, Drag, Electrooptics, Fluid dynamics; Fluid mechanics; Hydrodynamics; Hydromechanics; Incompressible flow; Laminar boundary layer, Optical measuring instruments, Piezoelectricity, Surface waves, Uniform flow, Water tunnels		
20. ABSTRACT (Continue on reverse side if necessary and identify by block number) An active-wall device was developed ^{to determine} for determination of those characteristics of traveling surface waves which are important in drag reduction with compliant coatings. The feasibility of an active wall was demonstrated with a Kelvin-Helmholtz solution for flow over a semi-infinite surface with traveling surface waves. The analysis indicated that wall motion could be adjusted so that freestream disturbances and the secondary flow generated by the leading edge could be modified or eliminated. → (circled)		

Block 20 Continued

to cancel

→ An all solid-state electromechanical device was built which produces short-wavelength traveling surface waves. The active wall was nominally designed ~~for the cancellation of~~ Tollmien-Schlichting waves in a laminar boundary layer. Wave form, wave speed, frequency, and amplitude were independently selectable. The electronic subsystem was a hybrid analog/digital device, and ~~the~~ wall motion was produced by piezoelectric ceramic elements. ~~The~~ surface displacement was measured with an electro-optical instrument developed for this research. Measurements of sinusoidal wall motion ranged in amplitude from 0.6 - 13 um over a frequency span of 10 - 150 Hz. ~~The~~ maximum phase speed was 166 cm/s. *MICRONS*

A low-turbulence water tunnel was designed and assembled for the active-wall experiments. ~~The~~ design velocity was 10 m/s in a test section, whose height, width, and length are, respectively, 15.2, 22.9, and 76.2 cm. ~~The~~ longitudinal relative turbulence intensity in the test section was estimated to be less than 0.2%. The flow characteristics are to be measured in the near future.

Keywords: (to p i)

TABLE OF CONTENTS

	<u>Page No.</u>
PREFACE	1
SUMMARY	3
PUBLICATIONS AND REPORTS	5
PRESENTATIONS	6
APPENDIX A	7
A Noncontacting Electroptic Displacement Sensor for Piezoelectrically Driven Active Surfaces	
APPENDIX B	17
Active-wall Device for the Generation of Small Traveling Surface Waves	
APPENDIX C	61
Design of a Low-Turbulence Water Tunnel	
APPENDIX D	91
Flow Over a Semi-Infinite Plate with Traveling Surface Waviness and Freestream Disturbances	

Page 64 does not contain proprietary
information per Dr. Michael M. Reisch-
man, ONR/Code 432

Accession For	
NTIS GRA&I	<input checked="" type="checkbox"/>
DTIC TAB	<input type="checkbox"/>
Unannounced	<input type="checkbox"/>
Justification	
By _____	
Distribution/	
Availability Codes	
Dist	Avail and/or Special
A-1	



PREFACE

This research project was financially supported by The Office of Naval Research (ONR) as part of the Compliant Coating Drag Reduction (CCDR) Program under Contract No. N00014-82-C-0199. The personal interest and advice of Dr. Michael M. Reischman, ONR Scientific Officer, is gratefully acknowledged. The expert boundary-layer consultation and encouragement from Dr. Harold Rogler of United Research Corporation in Santa Monica, California, is greatly appreciated. The superb design of the mechanical components for this research was provided by Mr. Ed Schroeder. A number of dedicated technicians and other support personnel too numerous to identify by name also contributed to this program.

SUMMARY

The primary purpose of this research was to measure experimentally the initial amplitude and growth of instability waves in a laminar water boundary layer under the influence of an active wall. The research was conducted in support of the Compliant Coating Drag Reduction (CCDR) Program for the Office of Naval Research (ONR). Although the final objective was not met as a consequence of limitation in funds, several goals were achieved in its support. The publications, reports, and presentations for this program are listed in the following sections, and the technical accomplishments are described in detail in the appendices which include all publications and reports.

Appendix D provides the theoretical basis for the feasibility of an active-wall device. The analysis involves a Kelvin-Helmholtz solution for flow over a semi-infinite surface with traveling surface waves. Although the leading edge of the surface generates a secondary flow, wall motion can be adjusted to modify or eliminate freestream disturbances and the secondary flow.

Appendix A describes a noncontacting electrooptic displacement sensor for the measurement of active-wall motion. The sensor monitored surface displacements at a stand-off distance of 23 cm with a two-element position sensitive detector and a two-arm optical triangulation method. The displacement sensor, which was designed for operation in either air or water, demonstrated a resolution of better than $1.3\text{ }\mu\text{m}$ over a range of 1.3 mm. The system was tested with two light sources, an infrared LED (light emitting diode) and a helium-neon laser.

Appendix B presents the results on the development of an active wall which was an all solid-state electromechanical device for the generation of small traveling surface waves. The active wall was nominally designed for the cancellation of Tollmien-Schlichting waves in a laminar boundary layer in water. The active surface area of the prototype device was 51 mm wide by 40 mm long in the flow direction. Wave form, wave speed, frequency, and amplitude of the mechanism were independently selectable. The electronic subsystem was a hybrid analog/digital device, and the wall motion was produced by piezoelectric ceramic elements. Sinusoidal wall motion was measured in air over an amplitude range of 0.6 - 13 μm and

frequency span of 10 - 150 Hz. The maximum wave speed was 166 cm/s. The paper also includes a review of previous active-wall devices.

Finally, Appendix C presents the details on the design of a low-turbulence water tunnel for an active wall experiment. Although the test section was designed for an active-wall experiment, other laminar and turbulent boundary layer experiments can be performed in the facility. The water tunnel was designed for a velocity of 10 m/s (32.8 ft/s) in the test section whose height, width, and length are, respectively, 15.2, 22.9, and 76.2 cm (6 x 9 x 30 in). The top and two sides of the test section were constructed from Plexiglas for flow visualization and laser Doppler (LDA) measurements while the bottom surface is a smooth flat aluminum plate for boundary layer measurements. Estimates indicate that the longitudinal relative turbulence intensity in the test section should be less than 0.2%. Although the tunnel has been assembled, the flow characteristics of the test section have not been measured.

The water tunnel was fabricated and assembled with funds from Southwest Research Institute (SwRI). Most of the water tunnel was constructed from stainless steel. The contraction section is a matched-cubic curve with a polished stainless steel interior, and its contraction ratio is 16.7. The settling chamber contains six fine-mesh screens and stainless steel honeycomb. The facility also includes an in-line aluminum heat exchanger which also functions as a flow straightner.

PUBLICATIONS AND REPORTS

1. Harold L. Rogler, "Flow over a Semi-Infinite Plate with Traveling Surface Waviness and Freestream Disturbances," URC-TR-83-021, United Research Corporation, Santa Monica, California (March 1983).
2. Steve A. Cerwin, "A Noncontacting Electrooptic Displacement Sensor for Piezoelectrically Driven Active Surfaces", in Symposium on Flow-Induced Vibrations, Volume 5, edited by M. P. Paidoussis and A. J. Kalinowski (American Society of Mechanical Engineers, New York, 1984), pp. 1-7.
3. Joel T. Park, H. Stanley Silvas, Jr., and Steve A. Cerwin, "Active-wall Device for the Generation of Small Traveling Surface Waves," Review of Scientific Instruments (to be published May 1985).
4. Joel T. Park, "Design of a Low-Turbulence Water Tunnel," SWRI 6984, Southwest Research Institute, San Antonio, Texas (March 1985).

PRESENTATIONS

1. Joel T. Park and H. Stanley Silvus, Jr., "Experiments on the Influence of Active Walls on the Initial Amplitudes and Growths of Instability Waves," in Drag Reduction Symposium edited by Michael M. Reischman (Office of Naval Research, Arlington, Virginia, 1982) p. 22.
2. Joel T. Park, H. Stanley Silvus, Jr., and Steve A. Cerwin, "Experiments on the Influence of Active Walls on the Initial Amplitudes and Growths of Instability Waves," FY83 Compliant Coating Drag Reduction Program Review, Naval Research Laboratory, Washington, D.C., sponsored by Office of Naval Research (October 1983).
3. Joel T. Park, H. Stanley Silvus, Jr., and Steve A. Cerwin, "An Active-Wall Device for the Generation of Small Traveling Surface Waves," FY84 Compliant Coating Drag Reduction Program Review, Naval Research Laboratory, Washington, D.C., sponsored by Office of Naval Research (October 1984).

APPENDIX A

A Noncontacting Electrooptic Displacement
Sensor for Piezoelectrically Driven Active Surfaces

by

Steve A. Cerwin
Southwest Research Institute

in Symposium on Flow-Induced Vibrations, Volume 5
edited by M. P. Paidoussis and A. L. Kalinowski
(American Society of Mechanical Engineers, New York, 1984)
pp. 1-7

A NONCONTACTING ELECTROOPTIC DISPLACEMENT SENSOR FOR PIEZOELECTRICALLY DRIVEN ACTIVE SURFACES*

S. A. Carwin
Southwest Research Institute
San Antonio, Texas

ABSTRACT

A noncontacting electrooptic displacement sensor for the measurement of the motion of a piezoelectrically excited active wall is described. The active wall was constructed and studied as part of a program conducted for the Office of Naval Research to investigate the drag reduction properties of an actively driven surface in turbulent water flow. The sensor employed a two arm optical triangulation method with a two element position sensitive detector to monitor the surface displacements from a stand-off distance of 23 cm (9 inches). Designed to operate in either an air or water medium, the displacement sensor demonstrated better than $1.3 \mu\text{m}$ ($50 \mu\text{-inch}$) resolution over displacement ranges of approximately 1.3 mm (.05-inch). The system was implemented in two different configurations: one using an infrared LED light source and the other a visible red helium-neon laser source. In both cases, the light source was modulated, and a phase locked detector was used to reject unwanted ambient light. Spot size was an adjustable parameter and was set to 1 mm (.04-inch) for this application. The displacement monitor was articulated in three axes on precision translation stages to cover a 5 cm x 13 cm (2-in. x 5-in.) area. The system was successfully used to monitor accurately displacements on the order of $25 \mu\text{m}$ (.001-inch) peak-to-peak on an active wall driven by piezoelectric transducers over an acoustic frequency range from DC to 150 Hz.

INTRODUCTION

This paper describes a noncontacting electrooptical displacement sensor developed to monitor the motions of a piezoelectrically excited active wall with peak-to-peak displacements on the order of $25 \mu\text{m}$. The active wall was devised in a program conducted for the Office of Naval Research† to investigate the drag reduction properties of an actively driven surface in turbulent water flow. The active portion of the wall was constructed by stretching a thin, diffusely reflecting mylar membrane over an array of piezoelectric pushers spaced at an interval of 1.25 mm. A cross sectional view of the wall construction is given in Figure 1. Because each of the piezoelectric elements could be driven independently, proper adjustment of the phase and amplitude of individual drive wave-

*Supported by the Office of Naval Research Contract N00014-82-C-0199

†ONR Contract N00014-82-C-0199

the present research was completed, Carpenter and Garrad¹⁸ shown that the Landahl-Kaplan membrane model is quantitatively incorrect; however, they have not computed the correct stability curves. Included in Table II are numerical results for both parallel and non-parallel flow calculations. Non-parallel calculations¹⁶ are in better agreement with experiment.

For selection of dimensional wave parameters, some physical property must be identified. Since water boundary layers are very thin, thickness is probably the limiting factor in boundary layer measurements. A reasonable boundary layer thickness with sufficient resolution appears to be approximately 2 mm. Distance from the leading edge of a flat plate for a laminar boundary layer in a zero pressure gradient is related to boundary layer thickness¹⁹ by

$$\delta/x = 6.017 (Re_x)^{-1/2}. \quad (3)$$

Dimensional properties for T-S waves and a membrane are summarized in Table III in comparison to the boundary-layer stability experiments of Strazisar et al.,²⁰ for water.

On the basis of information in Table III, frequency, wavelength, wave speed can be selected for the active wall; however, amplitude cannot be determined from stability theory. Normal velocity at the wall should be large enough to influence the flow favorably, the amplitude should not cause transition. From Eq. (1) normal velocity at the wall is

lements which are driven electronically, in contrast to Kendall's⁷ active wall which was driven mechanically by a cam and electric motor. For pure sinusoidal motion, coordinates of the wall are given by

$$y = a \sin [\alpha (x - ct)] \quad (1)$$

where α is the wave number, $2\pi/\lambda$. In the present application, parameters of the wall motion are selected on the basis of boundary layer theory.

Currently, no active-wall boundary-layer calculations are available for the selection of parameters, a , λ , and c . However, cMurry et al.,¹³ in a direct numerical simulation have shown that both linear and nonlinear T-S waves are dampened by a vertical velocity component at the wall which is out phase by 90° . With no other supporting data available, wavelength and wave speed were selected from calculations of the Orr-Sommerfeld equation.^{14,15,16}

Several criteria could be used in selection of the wave parameters. One criterion is the critical Reynolds number, and another is derived from the wave characteristics of the Landahl-Kaplan¹⁷ membrane model that most significantly affect the neutral stability curve. Nondimensional characteristics of the membrane model are listed in Table II. Circular frequency ω or $2\pi f$, wave number α , and wave speed c are nondimensionalized by the freestream velocity U_∞ and the boundary layer thickness δ (thickness at 99.9% U_∞). Wave speed is related to frequency and wavelength by

$$c = \lambda f = \omega / \alpha. \quad (2)$$

air device may only be applicable for air flows. A summary of the wave characteristics of these active walls is presented in Table I.

Other devices have also been successful in cancelling Tollmien-Schlichting waves and increasing transition Reynolds number. For example, Liepman and Nosenchuck¹⁰ were able to increase transition Reynolds number in a water tunnel through active control of wall heating. Milling¹¹ generated and cancelled T-S waves in a water channel with a pair of vibrating ribbons, and Thomas¹² performed similar experiments in a wind tunnel.

Objectives of the present active-wall research are much broader. In addition to the possibility of drag reduction, the active wall will provide information on the interaction of small traveling surface waves with the boundary layer. Such information may identify the required wave characteristics of a passive compliant coating for drag reduction. The results to be described in this paper include development of performance criteria, details of the mechanical and electrical designs, and measurement of active-wall performance characteristics.

. BOUNDARY LAYER THEORY

Conceptually illustrated in Fig. 1, the active wall consists of a set of actuators which are covered with a flexible surface. These actuators are driven sequentially so that a traveling surface wave with amplitude a , wavelength λ , and phase speed c , is generated. In the present active wall, the actuators are piezoelectric

INTRODUCTION

Compliant coatings have been investigated over the last 25 years as a means of drag reduction in water. The first compliant coating was developed by Kramer,^{1,2} who speculated that dolphin's speed is enhanced by its pliable skin. Since Kramer presented his experimental data on the drag reducing properties of compliant surfaces, many theoretical and experimental results have been published on the physical mechanisms involved. To date, these results have been rather inconclusive according to reviews by Bushnell et al.^{3,4} In many experiments drag increased with compliant walls, and in those cases where drag reduction occurred, results have not been repeatable by others.

A compliant coating of sufficient pliability will interact with the flow. Speculation is that the boundary layer flow may interact with a Kramer-like coating so that drag is reduced. However, very pliable coatings will form relatively large waves^{5,6} that increase drag. Since the physics which may allow drag to be reduced is not known, an active-wall device was designed and constructed for a controlled investigation of the possibility of drag reduction for small traveling surface waves. Similar research was done by Kendall,⁷ who used an active wall to provide insight into the air-sea interaction problem for a turbulent boundary layer. Wehrmann⁸ successfully cancelled Tollmien-Schlichting (T-S) waves in an air boundary layer with an active wall. An interesting active wall concept based on electrostatics was developed by Weinstein and Balasubramanian⁹ for short wavelengths; however,

Active-wall device

for the generation of small traveling surface waves

Joel T. Park, H. Stanley Silvis, Jr., and Steve A. Cerwin

Southwest Research Institute, San Antonio, Texas 78284

(Received 23 March 1984; accepted for publication 1 Feb 1985)

An all solid-state electromechanical device has been developed which produces short-wavelength traveling surface waves. The active wall was nominally designed for the cancellation of Tollmien-Schlichting waves in a laminar boundary layer in water. The primary purpose of the device was determination of traveling surface wave characteristics which are important for drag reduction with compliant coatings. Wave form, wave speed, frequency, and amplitude are independently selectable. Sinusoidal wall motion, measured in air with an electro-optical displacement sensor, ranged from 0.6 to 13 μm over a frequency span of 10 to 150 Hz. Roll-off frequency at the -3 dB point was 120 Hz, while the maximum phase speed was 166 cm/s. The electronic subsystem is a hybrid analog/digital device, and the active wall employs piezoelectric ceramic elements to produce surface motion.

PACS numbers: 47.80.+v, 47.35.+i, 47.15.Fe, 47.25.Fj

APPENDIX B

Active-wall Device for the Generation
of Small Traveling Surface Waves

by

Joel T. Park, H. Stanley Silvus, Jr., and Steve A. Cerwin
Southwest Research Institute

to Appear in Review of Scientific Instruments
(May 1985)

an adjustable parameter and is controlled by the Q of the 5 kHz bandpass amplifier, design of the output low pass filter, and (somewhat) on the selection of carrier frequency.

ACTIVE WALL MEASUREMENTS

Actual measurements made on the prototype active wall are given in Figures 6, 7 and 8. In Figure 6, the amplitude response of an individual element of the active wall is plotted as a function of applied driving voltage at a fixed frequency of 40 Hz. Figure 7 shows the frequency response of the same element plotted as a function of drive frequency for an applied voltage of 150V peak-to-peak. For both Figure 6 and 7 the raw data obtained from the displacement monitor was corrected by the amplitude and frequency response calibrations of Figures 4 and 5. Figure 8 shows the longitudinal phase response of the active wall when set up to produce a traveling wave. The data were taken by translating the displacement monitor along the length of the active wall (transversing from element to element) at a fixed standoff distance. The wall demonstrated excellent phase linearity over a distance of approximately 30 mm (1.2 in.).

CONCLUSIONS

In summary, a methodology for producing noncontacting displacement measurements through air and water path distances to surfaces possessing very small absolute displacements has been described. Actual measurements have been performed on a piezoelectrically driven active wall with successful results.

ACKNOWLEDGMENTS

The author wishes to acknowledge sponsorship of the Office of Naval Research for the reported work, the many helpful discussions on measurement technique with Mr. H. Stanley Silvas, Jr, and Dr. Joel T. Park, and construction of the project hardware by Mr. Harold F. Donoho, Jr.

REFERENCES

1. Park, J. T., Silvas, H. S., Jr., and Cerwin, S. A., "An Active Wall Device for the Generation of Small Traveling Surface Waves," Review of Scientific Instrumentation (submitted for publication).
2. King, J. D., and Cerwin, S. A., "System for Inventorying Road Surface Topography (SIRST)," U. S. Department of Transportation, Federal Highway Administration, Final Report Contract No. DOT-FH-118498, FHWA/RD-82/062, Aug. 1982.

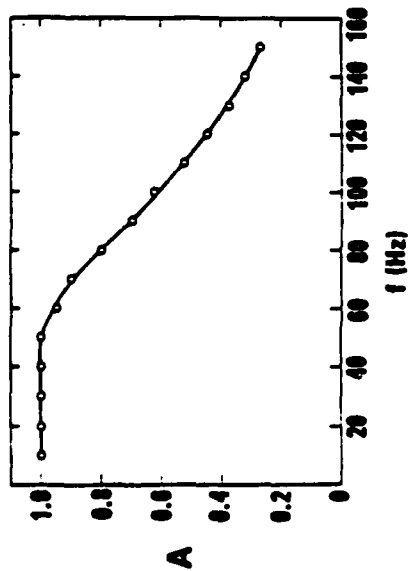


Figure 5. Amplitude Response For Electro-Optical Sensor

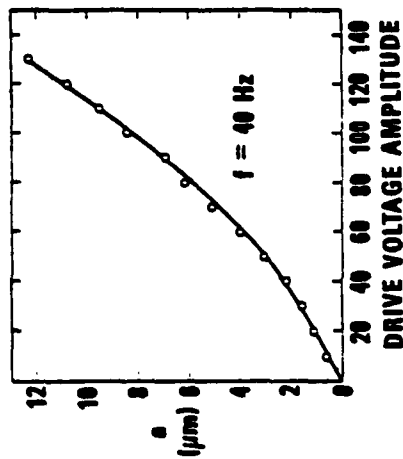


Figure 6. Wave Amplitude Calibration For Active Wall

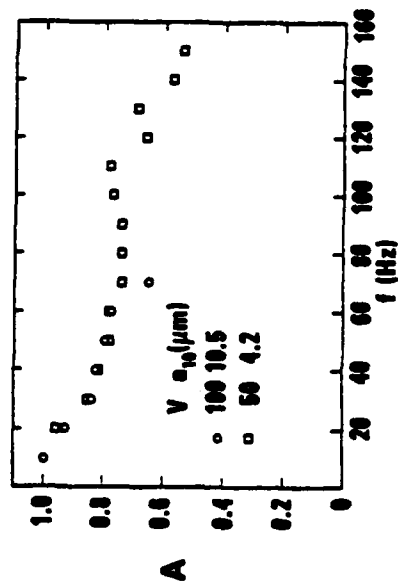


Figure 7. Wave Amplitude Response For Active Wall

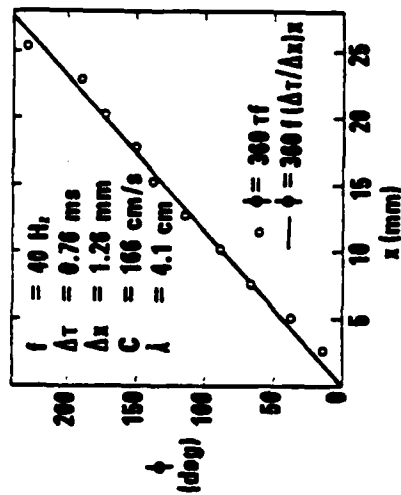


Figure 8. Phase Response For Active Wall

Figure 4 is a typical response plot of the displacement sensor taken with the calibration fixture. The fixture was immersed in a transparent water tank for this test, with the reference surface set 15 cm from the entry point of the light beam. The infrared LED was used for the light source and the spot projection was directed into the tank normal to the top wall surface. The received light was collected through the adjacent tank side wall by the receiving lens which was oriented at 45° to the tank side wall. This resulted in a water path angle of 32° by virtue of refraction at the water/air interface. Linearity and resolution over the 25 μm peak-to-peak range is extremely good, as evidenced in Figure 4. Responsivity of the displacement sensor in this configuration was measured to be 61.58 $\mu\text{m}/\text{volt}$.

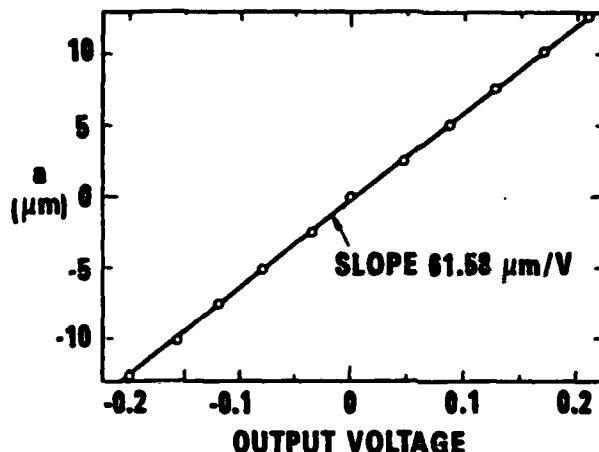


Figure 4. Displacement Calibration For Electro-Optical Sensor

Calibration data were taken in a total of four different configurations: in both air and water, and with both LED and laser light sources. The laser source has three distinct advantages and two distinct disadvantages for this application. First, the laser provides a much more intense source of light and operates at a wavelength which has little loss in water. The LED source, at 933 nm, is attenuated by the absorption band in water near 944 nm, presenting a signal strength problem for long water path distances. Second, the laser can be focused to a much smaller spot on the target surface, providing superior spatial resolution. The LED source cannot be focused efficiently to a spot much smaller than the physical diameter of the active area without incurring significant losses in intensity. Finally, the He-Ne laser operates in the visible red (as opposed to IR for the LED), making alignment of the system an easier task.

The disadvantages of using a laser are expense and stability. Most commercially available lasers in this power range, although relatively inexpensive in themselves, cannot be directly modulated. An acousto-optical modulator was used to provide the required 5 kHz subcarrier, and the cost of the modulator was more than that of the laser itself. Secondly, the laser must have a stabilized output relatively free from the noise components associated with the intermodulation products of multiple optical frequencies. These products commonly occur in the frequency range of 1 to 100 kHz, which is in-band to the 5 kHz subcarrier frequency. The noise components appear as sidebands about the 5 kHz subcarrier frequency and thus cannot be filtered easily. The analog division process removes most of the amplitude modulated noise components, but improvements in signal to noise ratios can be gained through the use of stabilized lasers.

The frequency response of the displacement monitor was measured by inserting an analog multiplier between the detector preamplifier and the remainder of the signal processing electronics. Light input to the detectors was held constant while the frequency of an external oscillator connected to the control input of the multiplier was varied. The frequency response curve is given in Figure 5 and shows reasonably flat response out to about 60 Hz with a roll off of approximately 8 dB/octave after the breakpoint. Response of the displacement sensor is

The sum of the two detector half outputs is a constant with respect to spot position and contains spot intensity and diameter information. The difference function is also influenced directly by spot intensity and diameter which is undesirable, as errors in the displacement measurement will occur if factors influencing spot intensity or detector sensitivity (e.g. LED or laser brightness, target surface reflectivity, water path attenuation, temperature, etc.) are variable. As the intensity and diameter data appear in both the difference and sum function, dividing the difference by the sum cancels errors associated with variable intensity or sensitivity. This method assumes uniform intensity within the spot, and no difficulties were encountered with nonuniform illumination or reflectance in this application. For details on a distance measurement system based on a similar principle but with provisions to cancel errors associated with nonuniformly reflective surfaces, the interested reader is referred to the system developed for profiling roadway surfaces [2].

A block diagram of the signal processing electronics for the displacement sensor is given in Figure 3. Design of the circuitry is straightforward and models the foregoing signal processing algorithm. A 5 kHz crystal controlled oscillator is used to drive the light modulator and to act as reference for the phase sensitive detectors. The outputs of the two detector halves are individually preamplified and filtered through active 5 kHz bandpass filters. DC restoration is accomplished through phase sensitive detectors and subsequent amplification by DC amplifiers. The DC voltages thus obtained (denoted by E1 and E2) are proportional to the light values impinging on each detector half. E1 and E2 are then processed by the differential and summation amplifiers and the resultant difference and sum are fed into the Y and X inputs of the analog divider. The quotient is $(E1-E2)/(E1+E2)$ and is taken as the displacement signal after high frequency noise component are removed by an active low-pass filter. The signal processing circuitry was packaged in a compact (12 cm x 18 cm x 25 cm) enclosure and was completely self-contained. The light source, lens systems, and detector assembly were mounted on a precision XYZ fixture for positioning over selected areas of the active wall.

Specification for some of the component parts implemented in the laboratory system are as follows:

LED Source:	Type TIES12 (Texas Instrument) 0.91 mm (0.036-inch) diameter 50 mw @ 933 nm
LED Projection lens Assembly:	72 mm focal length 50 mm diameter
Detector:	Type PIN Spot-2D (United Detector Technology) two element discreet active surface: 2.54 x 2.67 mm (0.1 x 0.105-in.)
Detector Lens Assembly:	47 mm focal length 45 mm diameter
Laser source:	Helium-Neon Type Spectra-Physics model 138, 1.0 mw @ 633 nm
Laser Modulator:	Acoustooptic Type Anderson Labs Model PLM-5VS 40 mHz center acoustic frequency 100% square wave modulation @ 5 kHz

SENSOR CALIBRATION AND FREQUENCY RESPONSE

The electrooptic displacement sensor was calibrated with a fixture constructed specifically for the task. The calibration fixture was fabricated by using a precision micrometer and ball configuration in conjunction with a 10:1 mechanical reduction arm to provide precise control over the reference surface. Thus 0.010-inch (254 μ m) of travel on the micrometer head (which was readable to 0.0001-inch or 2.54 μ m) produced 0.001-inch (25.4 μ m) of travel at the reference surface. Precision ball bearings were used for the fulcrum.

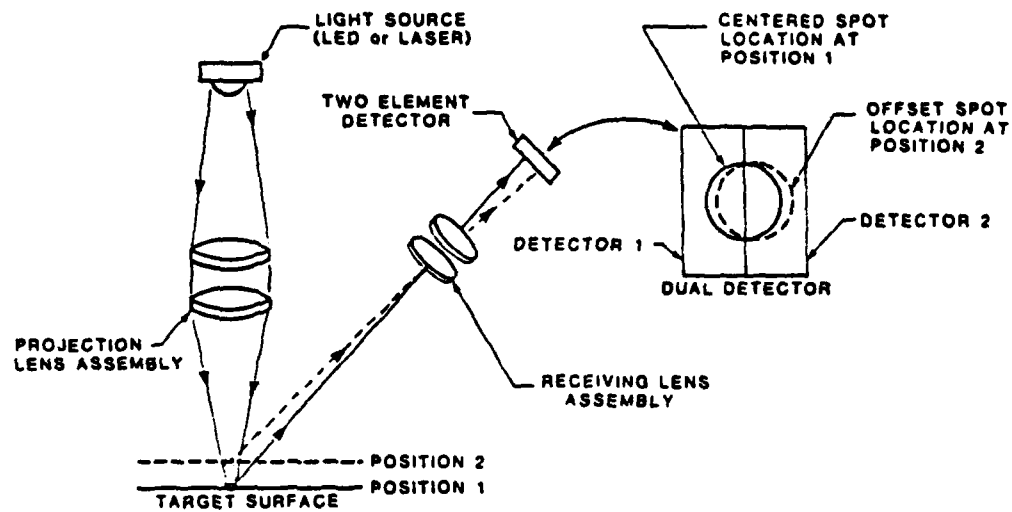


Figure 2. Optical Displacement Measuring Technique

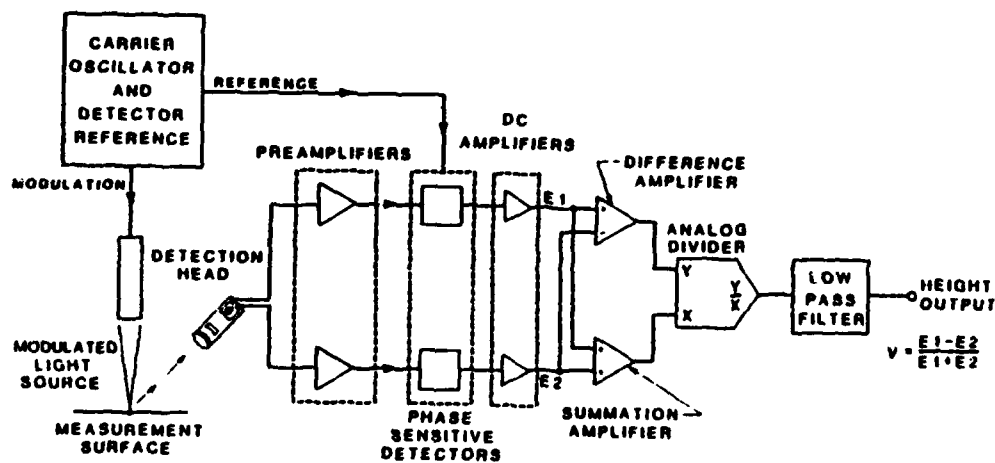


Figure 3. Electro-Optical Displacement Sensor

forms provided stationary or traveling surface waves programmable in direction, amplitude, frequency, and in the case of traveling waves, wave speed. Details of the entire active wall program are being presented elsewhere [1] and the remainder of this paper describes the electrooptical displacement sensor and subsequent measurements performed on the active wall.

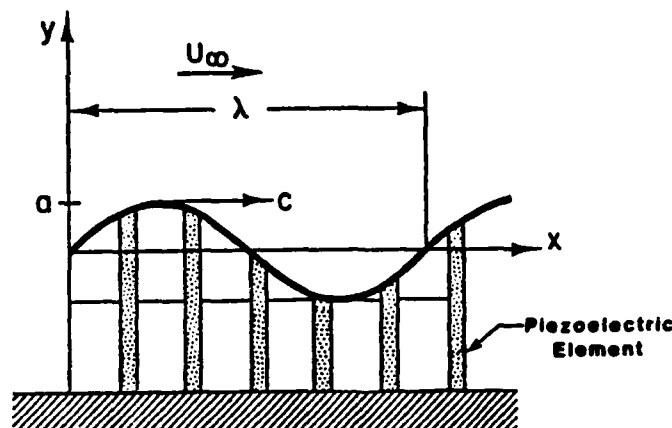


Figure 1. Illustration of Piezoelectrically Driven Active Wall.

PRINCIPLES OF OPERATION

The methodology used for the measurement technique is an adaptation of a technique developed by the author to profile roadway surfaces from a moving vehicle [2] and is illustrated in Figure 2. Two variations of the method can be implemented by choice of light source: a 1 mw Helium-Neon laser operating in the visible red at 633 nm or a high power (100 mw) light emitting diode (LED) operating in the near infrared at 933 nm. In both cases the light source is 100% amplitude modulated at a frequency of 5 kHz for use with phase sensitive detection so that a high signal-to-noise ratio and rejection of ambient light can be achieved. For the infrared version, the LED is modulated directly by the drive current, and for the visible red version, an acousto-optic modulator is used to modulate the laser. The light source is projected onto the target surface by a lens assembly oriented normal to the target surface to form a spot 1mm in diameter, a spot size small enough to resolve individual piezoelectric elements.

A portion of the light scattered from the diffusely reflecting target surface is collected by a receiving lens assembly oriented at 45° to the target surface. The lens assembly images the illuminated spot onto the center of a two element PIN photodiode detector with unity magnification. This target surface position, denoted as POSITION 1 in Figure 2, is the reference (or zero), position about which displacements are measured. At this position, the spot image is exactly centered on the two detector halves thereby causing the outputs of the two halves to be equal. By virtue of the 45° geometry, a positive or negative displacement of the target surface from the reference position causes a corresponding lateral shift of the spot image on the face of the dual detector. An example of a negative displacement is shown as POSITION 2 and is represented by the dashed lines for the target surface, light path, and spot image on the dual detector. Shifting the image of the spot on the face of the detector causes more area of the spot to fall on one half of the detector than the other, thus producing unequal outputs. The displacement signal is extracted by computing the difference and sum of the outputs of the two detector halves, then dividing the difference by the sum. The difference between the two detector halves as the image of the spot is translated from one detector half to the other, (beginning with the spot completely one half), is simply the difference in areas of a circle divided by a chord. The function is "S" shaped, with extremely good linearity for small displacements about center.

$$v = dy/dt = -a\omega \cos [\alpha(x - ct)]. \quad (4)$$

Then, amplitude is

$$a/\delta = \sqrt{2} (\sigma_v/U_\infty) / (\omega\delta/U_\infty) \quad (5)$$

where σ_v is the standard deviation of the normal velocity at the wall. The normal relative intensity, σ_v/U_∞ , at the wall should be higher than the relative turbulence intensity which is 0.1% in the better water tunnels.^{20,21,22} For an adequate rms signal-to-noise ratio, σ_v/U_∞ should be an order of magnitude larger; consequently, from an instrumentation viewpoint σ_v/U_∞ would be measured in the flow with an accuracy of 10% for an rms signal-to-noise ratio of 10. With a normal velocity component of 1% and a nondimensional frequency of 0.5, nondimensional amplitude should be 0.028. For a boundary layer thickness of 2 mm, amplitude should then be 57 μm . However, on the basis of other design considerations which are to be described subsequently, a design goal of 25 μm was selected.

Some experimental evidence is available on the required amplitude of the normal wall motion. Wehrmann⁸ was able to cancel T-S waves in a wind tunnel with an rms normal velocity of $3 \times 10^{-3}\%$ which is an order of magnitude smaller than the relative turbulence intensity of a good wind tunnel.²³ In the strip heater experiments of Liepmann et al.²², an equivalence between wall heating and wall motion was derived for a water boundary layer. For their experiments, the rms normal wall motion was related to the maximum

wall overheat, ΔT , in $^{\circ}\text{C}$ by

$$\sigma_v/U_{\infty} = 10^{-4} |\Delta T|. \quad (6)$$

The overheat was typically 3°C ; therefore, the equivalent rms wall motion was 0.03% which was the same order of magnitude as the 0.04% longitudinal turbulence intensity of the water tunnel.²²

Eight driving elements per wavelength were arbitrarily selected as adequate for generation of a sine wave. Wehrmann⁸ used ten in his active wall while Kendall⁷ claimed little distortion with four. On the basis of cost and the rationale of the previous discussion, the design criteria summarized in Table IV were chosen. Comparison of Tables III and IV indicates that the design criteria meet or exceed conditions likely to be encountered in a water flow experiment.

II. PRINCIPLES OF OPERATION

A. Piezoelectric Actuators

One of the major design goals for an active wall is that amplitude, frequency, and speed of the surface wave should be independently controllable. Most schemes for generating active-wall motion permit arbitrary control of only one or two of these parameters. For example, only wave speed could be varied in Kendall's⁷ experiments

For the present active wall, piezoelectric ceramic materials were selected as the most suitable electromechanical conversion actuators. A schematic cross section of a piezoelectrically actuated active wall is shown in Fig. 1 in which a number of piezoelectric elements with long dimensions vertical are standing on a

rigid base. Each element has a different voltage applied to it so that different degrees of elongation (greatly exaggerated in the figure) exist at each element. A thin membrane attached to the tops of all of the piezoelectric elements provides for interpolation to produce relatively smooth curvature of the wall surface and, of course, prevents fluid penetration into the volume occupied by the piezoelectric elements.

In operation, all of the piezoelectric elements are driven by electrical signals of the same amplitude and frequency; however, the signal applied to each successive element proceeding from left to right in Fig. 1 is delayed in phase by a progressively increasing amount so that a sinusoidal disturbance is produced on the active-wall surface. Additionally, at a selected time interval, the instantaneous signal value on each element is shifted to the next element to the right so that the sinusoidal disturbance propagates from left to right.

A piezoelectric material changes physical dimensions in response to an applied electric field; conversely, when a piezoelectric material is mechanically stressed, it generates a proportionate electrical signal. Hence, piezoelectric materials may be used as electrical-to-mechanical or mechanical-to-electrical transducers. For the active wall, the electrical-to-mechanical conversion capability is utilized. Figure 2 illustrates a rectangular piezoelectric ceramic slab having dimensional proportions that dictate operation in the longitudinal-extension mode; that is, length is at least three times width, and width is substantially greater

than thickness. Further, the two large faces (defined by length and width) are covered with metallic electrodes between which an electrical drive voltage is applied.

In Fig. 2 a system of coordinate axes is defined, and these axes are labeled. The direction of polarization is designated axis 3, and the principal mechanical axis is designated 1. The remaining axis in the mutually perpendicular triplet is designated 2. As indicated in Fig. 2, when an electrical drive voltage is applied between electroded faces of the piezoelectric element, elongation (or contraction, which is negative elongation) occurs along the principal mechanical axis. Whether elongation is positive or negative depends upon polarity of the applied drive voltage.

Relationships between electrical drive and mechanical response are described by a series of piezoelectric constants characteristic of the particular material employed. In the case of a longitudinal-extension element such as illustrated in Fig. 2, the constant of proportionality is the piezoelectric strain constant d_{31} which is the ratio of strain (i.e., ratio of elongation to length) to impressed electric field (i.e., ratio of applied voltage to thickness). The impressed electric field is in the 3 direction and mechanical response is in the 1 direction; hence, the subscript 31. Expressed mathematically, the relationship^{24,25} between mechanical response and impressed electric field is

$$\sigma = d_{31}\epsilon \quad (7)$$

where σ is strain, ϵ is electric field, and d_{31} is piezoelectric strain constant.

By definition,

$$\sigma = \Delta l / l \quad (8)$$

and

$$\epsilon = V / t \quad (9)$$

where Δl is elongation, l is element length, V is applied voltage, and t is element thickness. From Equations (7), (8), and (9)

$$\Delta l = (d_{31} l V) / t . \quad (10)$$

From Equation (10) piezoelectric strain constant, element length, and applied voltage should be maximized while element thickness should be minimized for the required elongation, but practical constraints on piezoelectric element dimensions and on magnitude of applied voltage exist. Further, only a limited range of piezoelectric strain constants is available.

Current technology limits the size of sheet piezoelectric materials to a maximum length of 76 mm and a minimum thickness of 0.25 mm. Thus, the limiting values of length and thickness (76 mm and 0.25 mm, respectively) and a width of 25 mm (i.e. one-third of the length to insure longitudinal-extension mode of operation) were selected for element dimensions. Further, a lead zirconate titanate (PZT) ceramic, PZT-5H from Vernitron, Inc., Bedford, Ohio, was chosen because it has the highest available piezoelectric strain constant (d_{31}) with a value of 274 pm/V. With these parameters and a peak applied voltage of 300 V, peak elongation or amplitude was estimated to be 25 μ m from Eq. (10).

B. Mechanical Assembly

The active-wall model was built in cells which were fabricated as shown in Fig. 3. Each cell contained two piezoelectric elements with dimensions 76-mm long X 25-mm wide X 0.27-mm thick. Two such elements were placed side by side for an assembly that was 51-mm wide. A 0.03-mm thick metal-foil electrode with an integral electrical connection tab was placed on each side of the pair of piezoelectric ceramic plates with the connecting tabs from opposite faces extending from opposite sides of the assembly. A silicone rubber insulator 0.46-mm thick was placed on each side of the assembly to complete an individual cell. The silicone rubber insulators between piezoelectric elements provided not only electrical insulation, but also a compliant interface to insure independence of operation of adjacent piezoelectric elements. Total cell thickness was 1.25-mm. Elongation is parallel to the 75-mm dimension of the cell, and fluid flow is parallel to the thickness of the cell as shown in Fig. 3.

Individual cells were stacked with large face to large face in a box-like container as shown in Fig. 4. Because each cell had a layer of silicone rubber on each side, in the assembly two thicknesses of silicone rubber were located between pairs of piezoelectric elements. Directions of elongation and fluid flow relative to the overall structure are also shown in Fig. 4. The box was constructed of Plexiglas.

The top surface, which acted as the interface between the flowing fluid and the cavity containing the piezoelectric elements,

was a thin film of adhesive-backed, shrinkable plastic film (model airplane covering) that had an opaque white finish. The film was adhered to the top edges of the plastic box and then was thermally shrunk to make it contact the tops of the elements. The resulting active-wall area was 51 mm wide (transverse to the fluid-flow direction) and 40 mm long in the fluid-flow direction.

C. Electronic Control

1. Master Control Circuit

The basic system for generating drive signals for the individual piezoelectric actuator cells involves phase shift of a sine wave while its other characteristics are maintained constant. Phase shift was achieved with digital shift registers. The low-level signal-generating circuits were divided into two functional categories: (1) the master control circuit and (2) the individual channel circuit. The master control circuit provided an interface between the analog output of an external laboratory signal generator and a digital signal that could be passed from one channel to the next. The control system contained 32 identical channel circuits in cascade.

Figure 5 illustrates the master control circuit in block diagram form. The input signal is derived from a commercially available laboratory function generator that provides sinusoidal output with continuously variable amplitude and frequency. The input signal is converted periodically to an 8-bit offset-binary digital word whenever an electronic command is received from the timing generator. The analog-to-digital converter block also

includes a sample-and-hold circuit so that the input signal does not change during the conversion period.

System timing was controlled by a variable-frequency square-wave oscillator that was an integral part of the master control circuit. By establishing system timing, this oscillator controlled wave speed of the traveling wave on the active-wall surface. That is, a given sample of the input signal advanced from one piezoelectric element in the active-wall array to the next every time a clock pulse occurred. Wave speed, then, was the distance that the wave advanced along the active-wall surface (i.e., the cell-to-cell spacing Δx of 1.25 mm) divided by the time interval Δt_s between clock pulses. Since the highest frequency that the power amplifier could safely accommodate was 150 Hz and the minimum number of samples per cycle was 8, the minimum design sampling interval was 833 μs , and the maximum wave speed was then 1.5 m/s. Whenever the sampling interval was longer than the 833- μs minimum, wave speed was reduced proportionately.

When the output of the variable-frequency oscillator changed logic state in a selected direction, the timing generator issued a convert command to the analog-to-digital converter. At this point the input signal was sampled and was converted to digital form. The timing generator then waited until analog-to-digital conversion was complete. After a valid digital word was established on the 8-line digital output, a simultaneous clock pulse was issued by way of a buffer to all 32 individual channel circuits.

Frequencies in the range of 10 Hz to 150 Hz could be accepted by the electronic system. Going beyond the upper limit would result

in overstress of the transistors in the power amplifier. Wave speed could range from 10 cm/s to a maximum that was numerically equal to the input frequency. For example, at an input frequency of 100 Hz the maximum wave speed was 100 cm/s. This upper limit insured that waves on the active surface would contain at least 8 piezoelectric cells per wavelength. If lower resolution could be tolerated, then the wave speed limit could be exceeded without danger of damage to the circuit.

2. Individual Channel Circuit

The circuit associated with an individual channel of the active-wall driver is illustrated in the block diagram of Fig. 6. The 8-line digital input originates at the output of the master control circuit analog-to-digital converter (for channel 1 only) or at the output of the previous channel (for channels 2 through 32). Each channel incorporated a single-stage digital shift register with the capability of storing and simultaneously transferring 8 lines of digital information. As previously noted, the output of the shift register in a particular channel became the digital input for the subsequent channel. Upon receipt of a clock pulse, which entered an individual channel on the clock input line and propagated to the next channel by way of the clock output line, the 8-bit digital word present on the 8-line digital input was stored in the shift register, and the digital word that was in the shift register prior to the clock pulse was stored in the next channel shift register and so on. Thus, a given sample of the analog input signal moved without distortion or attenuation from channel to channel when commanded to do so by clock pulses.

When a digital word appeared at the output of a particular shift-register stage, a proportionate analog current was produced by a digital-to-analog converter. This current was converted to a voltage by a buffer amplifier, and the resulting voltage was applied to a power amplifier which, in turn, drove the piezoelectric ceramic element in the active-wall cell corresponding to that channel. Thus, as sequential clock pulses occurred, the analog signal impressed on a selected piezoelectric element replicated the master control circuit input signal delayed by an integral number of clock-pulse intervals.

At frequencies well below primary resonance, electrical characteristics of a piezoelectric element are essentially equal to those of a capacitor. Driving any kind of reactive load with a power amplifier results in a nonlinear load line for the power semiconductor devices in the output stage. Consequently, current through the power device is high when voltage across the device is also high; therefore, substantial instantaneous heating occurs which must be dissipated. Permissible combinations of voltage across a transistor and current through it are illustrated graphically in Fig. 7 by the safe operating areas (SOA) from manufacturers' specifications for bipolar transistors and vertical metal-oxide-silicon field-effect transistors (VMOSFET) with the same voltage rating. The load line for a 0.44- μ F capacitor, which simulates the total capacitance of an active-wall cell, driven at 150 Hz by a 600-V peak-to-peak sinusoid, is also plotted in Fig. 7. As the figure indicates, the VMOSFET is the most suitable power amplifier in the present application.

To develop the greatest possible voltage across the capacitive load from minimum power-supply voltage requires use of a bridge amplifier configuration such as that illustrated in Fig. 8 in which details of the bias circuits have been eliminated for clarity. The bridge circuit was implemented with complementary-symmetry transistors so that all of the bias networks in Fig. 8 are referred to the power supplies, and the drive voltages required by the upper and lower transistors are relatively low in amplitude and equal. The transistors ultimately used in the individual channel circuits of the active-wall driver had voltage ratings of 350 V which would have facilitated developing 700 V peak-to-peak across the capacitive load. However, the maximum voltage available from suitable commercial power supplies was 300 V, and this placed a 600-V peak-to-peak limitation on the signal that could be developed across the capacitive load.

In the circuit shown in Fig. 8 a positive-swinging voltage applied to the gate (G) of p-channel VMOSFET Q1 causes that transistor to cut off, while the same positive-going voltage applied to the gate of n-channel VMOSFET Q3 causes that transistor to turn on. A signal of the same amplitude, but inverted (i.e., shifted 180° in phase), is applied simultaneously to the gates of VMOSFET's Q2 and Q4 producing similar action so that Q1 and Q4 are simultaneously turned off while Q2 and Q3 are turned on. In this case the right-hand end of the capacitive load is pulled to the positive supply by Q2 while the left-hand end of the capacitive load is pulled to the negative supply by Q3. During the

posite half-cycle of the sinusoidal input voltage, roles of the VMOSFET pairs reverse; that is, Q1 and Q4 are turned on thereby pulling the left-hand end of the load to the positive supply and the right-hand end of the load to the negative supply. At the same time, VMOSFET's Q2 and Q3 are turned off so that no current flows through them. Thus, voltage across the load varies sinusoidally from +2 V (where V is the voltage of either the positive or negative power supply) to -2 V during the opposite half-cycle of the input signal; consequently, peak-to-peak voltage appearing across the capacitive load is 4 V. In the individual channel power amplifiers constructed for this program, the value of V is 150 V, so that the maximum voltage developed across the load is 600 V peak-to-peak. A low-voltage zener diode was incorporated in each gate circuit so that the gate-to-source voltage could not exceed rated value during power-supply turn on.

VMOSFET's are enhancement-mode devices which means that when the gate and source are at the same potential (i.e., zero bias), no drain current flows through the transistor. As the gate-to-source voltage is increased in the same polarity as the drain-to-source voltage, a threshold is reached at which the transistor suddenly starts conducting and transconductance (i.e., gain) increases dramatically. The latter characteristic implies that small additional increases in gate-to-source voltage will cause large changes in drain current; hence, unless gate-to-source voltage is carefully controlled, destructive currents may flow through the transistor. The problem is compounded because substantial device-to-device

variation occurs in threshold-voltage and transconductance characteristics. Hence, a fixed bias network may leave one device turned off, but may cause destructive currents to flow through another device from the same manufacturing lot. These problems were overcome by providing an adjustment in each bias circuit and developing a safe procedure for setting the operating point of each transistor in the bridge power amplifier.

II. ACTIVE WALL MEASUREMENTS

Motion of the active wall in air was measured with an electro-optical displacement sensor which employed a two-arm optical triangulation method and a two-element position-sensitive detector to monitor displacements at a point from a stand-off distance of 3 cm. Sensor response was very linear over the range of $\pm 13 \mu\text{m}$ with resolution less than $0.5 \mu\text{m}$ and sensitivity of $61.5 \mu\text{m/V}$. Frequency response had a low-pass characteristic with a -3 dB roll-off frequency of 90 Hz. Since the active wall was designed for an upper frequency limit of 150 Hz, measurements of the active wall were corrected with amplitude-response data. Additional details are discussed by Cerwin.²⁶

The active wall was mounted on an x-y translator with micrometer adjustments so that the surface of the active wall could be located normally and longitudinally relative to the displacement sensor with a resolution of $2.5 \mu\text{m}$ over the 24.5-mm travel ranges of the micrometers. The active wall was calibrated for amplitude and frequency response at a station between the first and second row of elements. At a frequency of 40 Hz, the input voltage amplitude to the elements was varied between 10 and 150 V with resulting

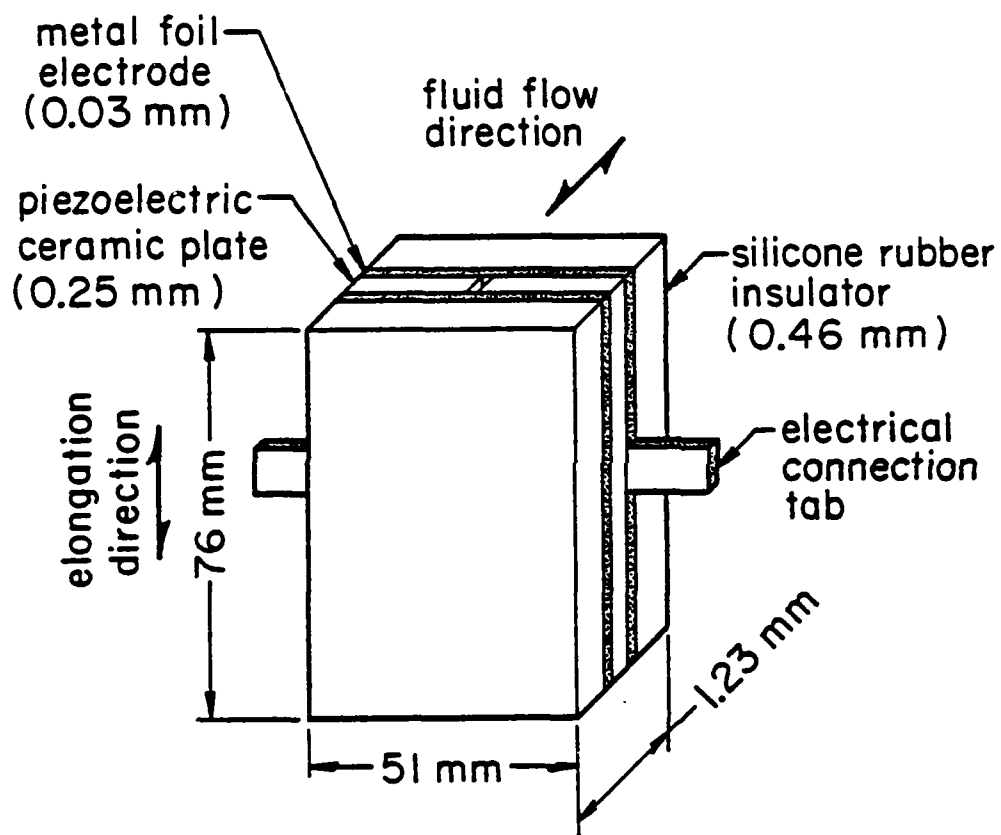
acement amplitude variation between 0.62 and 12.9 μm , respectively. Distortion of the sine wave impressed on the elements occurred to occur between 80 and 90-V amplitude. Calibration results are plotted in Fig. 9 and the amplitude response curve of the active wall is presented in Fig. 10 for two input voltage amplitudes normalized at 10 Hz. The roll-off frequency at -3 dB is 10 Hz for the 50-V input amplitude.

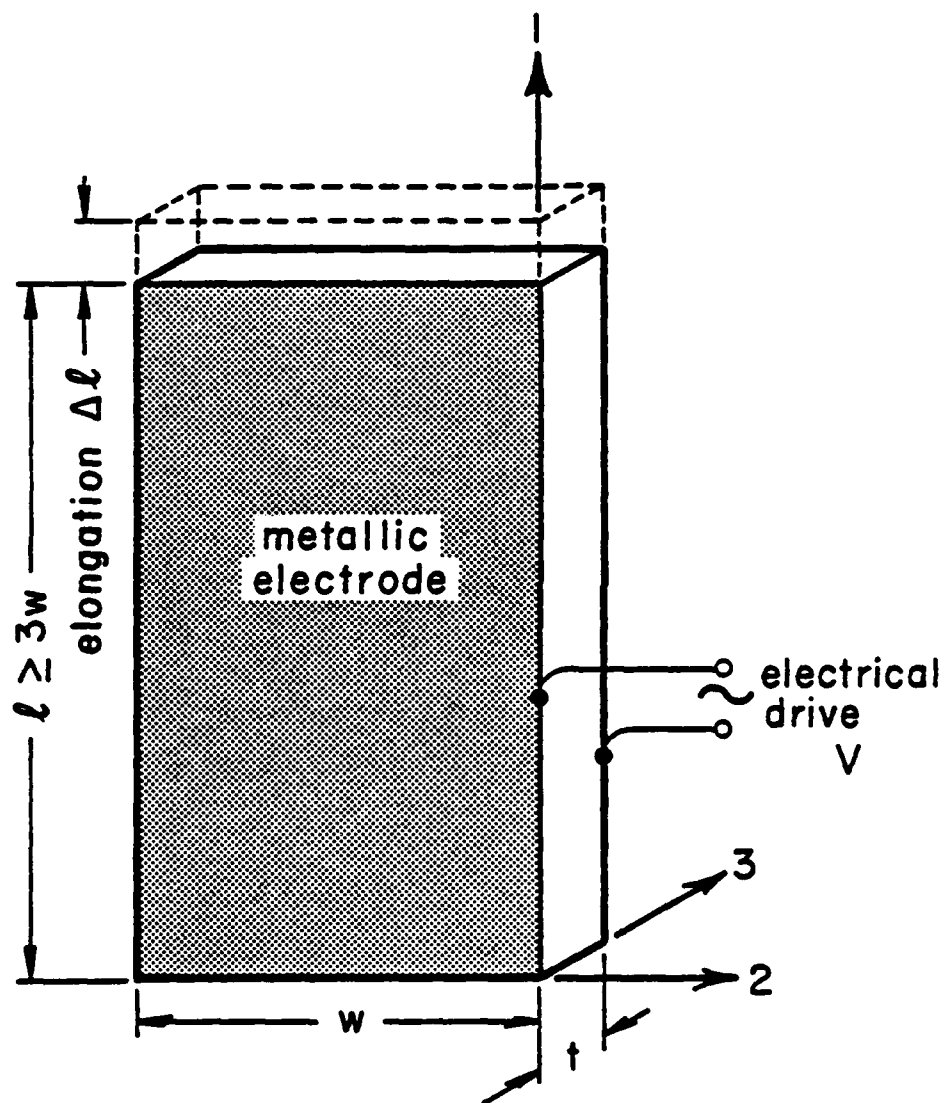
From data in Fig. 9 and physical dimensions of the ceramic elements, the piezoelectric strain constant d_{31} was computed from Fig. 10). The mean value of d_{31} for a single element over a voltage range of 10 to 140-V peak at 40 Hz was 259 pm/V at a standard deviation of 54 pm/V which is within 5.5% of the manufacturer's specification. Displacement measurements were also taken at ten different elements at 100-V peak and 40 Hz. The d_{31} for these measurements was 264 pm/V with a standard deviation of 51 pm/V.

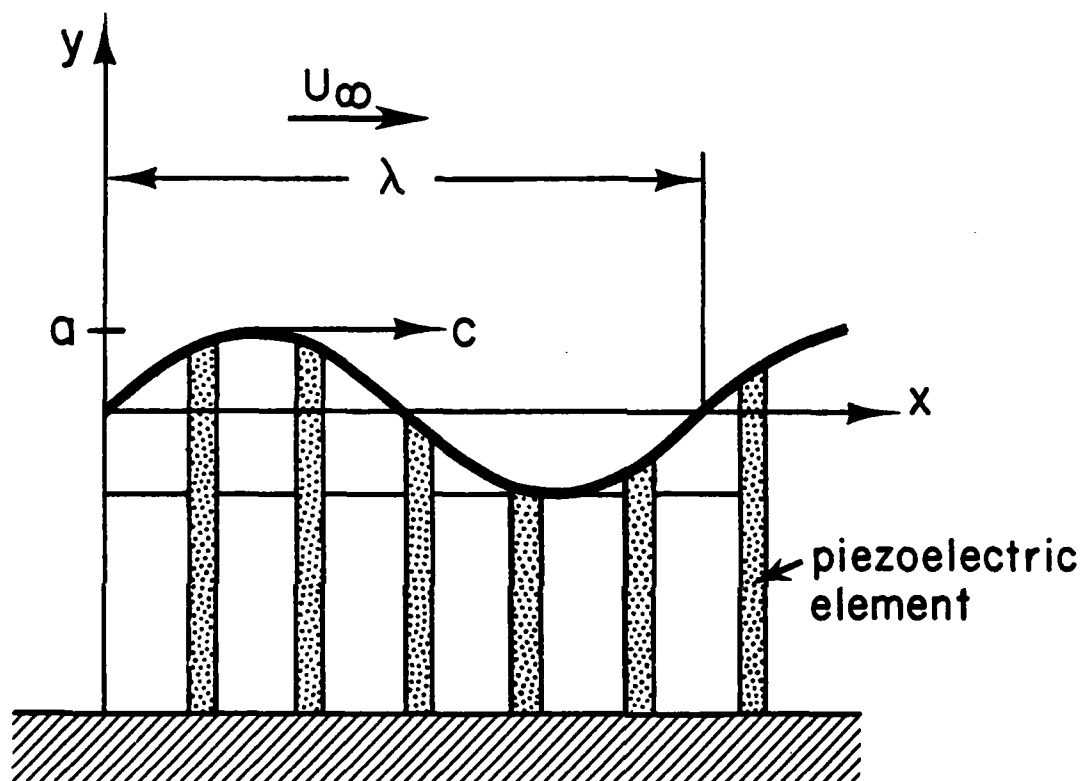
Since the displacement sensor is a point measurement device, a relation between longitudinal locations on the active wall was measured to demonstrate that the surface waves were traveling. The phase shift ϕ in degrees which is designed into the active wall is given by

$$\phi = 360f (\Delta\tau_S/\Delta x)x \quad (11)$$

where Δx is the spacing between elements, $\Delta\tau_S$ is the sample interval of the clock in the master control circuit of Fig. 5, and $c = \Delta x/\Delta\tau_S$.







- FIG. 1. Schematic diagram of active wall.
- FIG. 2. Longitudinal extension of piezoelectric element.
- FIG. 3. Typical active-wall cell configuration (not to scale).
- FIG. 4. Isometric drawing of active-wall assembly (not to scale).
- FIG. 5. Block diagram of master control circuit.
- FIG. 6. Block diagram of typical channel circuit.
- FIG. 7. Comparison of load line and safe operating areas for bipolar and VMOSFET power transistors.
- FIG. 8. Simplified schematic diagram of bridge power amplifier.
- FIG. 9. Wave amplitude calibration of active wall for a frequency of 40 Hz.
- FIG. 10. Wave amplitude response of active wall: \bigcirc 100 V input, 10.5 μm amplitude at 10 Hz; \square 50 V input, 4.2 μm amplitude at 10 Hz.
- FIG. 11. Phase response of active wall at $f = 40$ Hz, $\Delta\tau_s = 0.76$ ms, $\Delta x = 1.25$ mm, $c = 166$ cm/s, and $\lambda = 4.1$ cm: straight line, control settings; \bigcirc electro-optical displacement measurements.

TABLE IV. Design criteria for active wall.

Quantity	Symbol	Value	Units
Maximum frequency	f	150	Hz
Minimum wavelength	λ	10	mm
Maximum wave speed	c	1.5	m/s
Maximum amplitude	a	25	μm
Active length	L	40	mm
Cell spacing	Δx	1.25	mm
Number of cells	$L/\Delta x$	32	
Number of cells/wavelength	$\lambda/\Delta x$	8	

TABLE III. Physical dimensions of membrane and Tolmien-Schlichting waves in a water laminar boundary layer.

Source	δ (mm)	x (cm)	U_{∞} (cm/s)	f (Hz)	λ (cm)	c (cm/s)
Non-Parallel ^a	2	7.7	70	27	1.1	30
Parallel ^a	2	10.1	91	30	1.2	36
Membrane	2	27.6	251	100	1.3	126
Experiment ^{a,b}	4.1	14.5	32	6.5	2.0	13
Experiment ^{b,c}	1.5	14.0	234	95	0.9	83

^a At Critical Reynolds Number

^b Reference 20

^c At $Re_{\delta} = 3720$ and maximum instability

TABLE II. Nondimensional characteristics of membrane and Tolmien-Schlichting waves in a laminar boundary layer.

Source	$\delta U_\infty / \nu$	$\omega \delta / U_\infty$	$\alpha \delta$	c / U_∞
Non-Parallel Theory ^a	1400	0.48	1.15	0.42
Parallel Theory ^b	1820	0.42	1.05	0.40
Membrane Model ^c	5000	0.5	1.0	0.5

^a Reference 16 at critical Reynolds number

^b Reference 14 at critical Reynolds number

^c Reference 17 at reference Reynolds number

TABLE I. Summary of wave characteristics for various active walls.

Author	a (mm)	λ (mm)	L (cm)	Δx (mm)	c (m/s)	f (Hz)	v_{max} (cm/s)
Kendall ^a	3.18	102	122	25.4	3	30	59
Weinstein & Balasubramanian ^b	0.02	1.8	40	...	0	2,000	25
Wehrmann ^c	0.001	42	4.2	4.2	2.1	50	0.032
Present Work	0.013	10	4	1.25	1.2	120	1

^a Reference 7

^b Reference 9

^c Reference 8

- 26 S. A. Cerwin, in Symposium on Flow-Induced Vibrations, Volume 5, edited by M. P. Paidoussis and A. J. Kalinowski (American Society of Mechanical Engineers, New York, 1984) pp. 1-7.
- 27 G. D. Kuhn, P. Moin, J. Kim, and J. Ferziger, in Laminar Turbulent Boundary Layers, edited by E. M. Uram and H. E. Weber (The American Society of Mechanical Engineers, New York, 1984) pp. 61-71.

- 14 R. Jordinson, J. Fluid Mech. 43, 801-811 (1970).
- 15 M. D. J. Barry and M. A. S. Ross, J. Fluid Mech. 43, 813-818 (1970).
- 16 W. S. Saric and A. H. Nayfeh, Phys. Fluids 18, 945-950 (1975).
- 17 M. T. Landahl and R. E. Kaplan, in Recent Developments in Boundary Layer Research, Part I, AGARDograph 97 (North Atlantic Treaty Organization, Paris, 1965) pp. 363-394.
- 18 P. W. Carpenter and A. D. Garrad, University of Exeter, Technical Note 83/1, 1983.
- 19 A. M. O. Smith, Improved Solutions of the Falkner and Skan Boundary-Layer Equation, S. M. F. Fund Paper No. FF-10 (Institute of the Aeronautical Sciences, New York, 1954).
- 20 A. J. Strazisar, E. Reshotko, and J. M. Prah1, J. Fluid Mech. 83, 225-247 (1977).
- 21 R. J. Hansen, D. L. Hunston, C. C. Ni, M. M. Reischman, and J. W. Hoyt, in Viscous Flow Drag Reduction, edited by G. R. Hough (American Institute of Aeronautics and Astronautics, New York, 1980) pp. 439-452.
- 22 H. W. Liepmann, G. L. Brown, and D. M. Nosenchuck, J. Fluid Mech. 118, 187-200.
- 23 G. B. Schubauer and H. K. Skramstad, J. Aero. Sci. 14, 69-78 (1947).
- 24 B. Jaffe, W. R. Cook, and H. Jaffe, Piezoelectric Ceramics (Academic Press, New York, 1971).
- 25 "IRE Standards on Piezoelectric Crystals: Determination of the Elastic, Piezoelectric and Dielectric Constants - the Electro-mechanical Coupling Factor, 1958", Proc. IRE 46, 764-778 (1958).

- 1 M. O. Kramer, J. Aero. Sci. 24, 459-460 (1957); ASNE J. 72, 25-33 (1960).
- 2 M. O. Kramer, ASNE J. 73, 103-107 (1961).
- 3 D. M. Bushnell, J. N. Hefner, and R. L. Ash, Phys. Fluids 20 (10) Pt. II, S31-S48 (1977).
- 4 D. M. Bushnell, in Viscous Flow Drag Reduction, edited by G. R. Hough (American Institute of Aeronautics and Astronautics, New York, 1980), pp. 387-390.
- 5 R. J. Hansen and D. L. Hunston, J. Fluid Mech. 133, 161-177 (1983).
- 6 M. Gad-el-Hak, R. F. Balckwelder, and J. J. Riley, J. Fluid Mech. 140, 257-280 (1984).
- 7 J. M. Kendall, J. Fluid Mech. 41, 259-281 (1970).
- 8 O. H. Wehrmann, Phys. Fluids 8, 1389-1390 (1965).
- 9 L. M. Weinstein and R. Balasubramanian, in Second International Conference on Drag Reduction (British Hydromechanics Research Association Fluid Engineering, Cranfield, England, 1977), pp. E5-55-E5-76.
- 10 H. W. Liepmann and D. M. Nosenchuck, J. Fluid Mech. 118, 201-204 (1982).
- 11 R. W. Milling, Phys. Fluids 24, 979-981 (1981).
- 12 A. S. W. Thomas, J. Fluid Mech. 137, 233-250 (1983).
- 13 J. T. McMurray, R. W. Metcalfe, and J. J. Riley, in Proceedings of the Eighth Symposium on Turbulence edited by X. B. Reed, Jr., G. K. Patterson, and J. L. Zakin (University of Missouri-Rolla, Rolla, Missouri, 1984) pp. 328-338.

ACKNOWLEDGEMENTS

This project was financially supported by the Office of Naval Research (ONR) as part of the Compliant Coating Drag Reduction Program under Contract No. N00014-82-C-0199. The personal interest and advice of Dr. Michael M. Reischman of ONR is gratefully acknowledged, and the expert boundary-layer consultation and encouragement from Dr. Harold Rogler of United Research Corporation in Santa Monica, California, is greatly appreciated.

Recent numerical calculations by Kuhn et. al.,²⁷ indicate that drag reduction may be possible in a turbulent boundary with small traveling surface waves. However, these calculations imply that wavelength must be less than 1 mm in water with $\lambda/a = 40$. With the materials in the present active wall, wavelength can be reduced to approximately 3 mm by removal of one insulator sheet from each cell and reduction in the number elements per wavelength to four where the number of elements per wavelength is controlled electronically through selection of wave speed and frequency.

With application of multilayered monolithic ceramic technology, wavelength could be reduced to 0.25 mm, but such technology is not yet commercially available. When multilayer devices become available, a single piezoelectric element could consist of ten layers of ceramic separated by metal electrodes on the order of a few molecules thick. Since the thickness in Eq. (10) would be reduced by a factor of ten, voltage could be reduced by an equal factor for the same amplitude.

Significant advantages of the present device within its limitations are that amplitude, wave speed, and frequency can be controlled independently. Additionally, the wave forms are not limited to sinusoids. Since the drive system is electronic, a traveling surface wave of essentially arbitrary shape can be produced so that compliant-wall or active-wall theory based on nonsinusoidal surface waves could be tested with the device described in this paper.

Phase shift measured on the active wall by the displacement sensor is

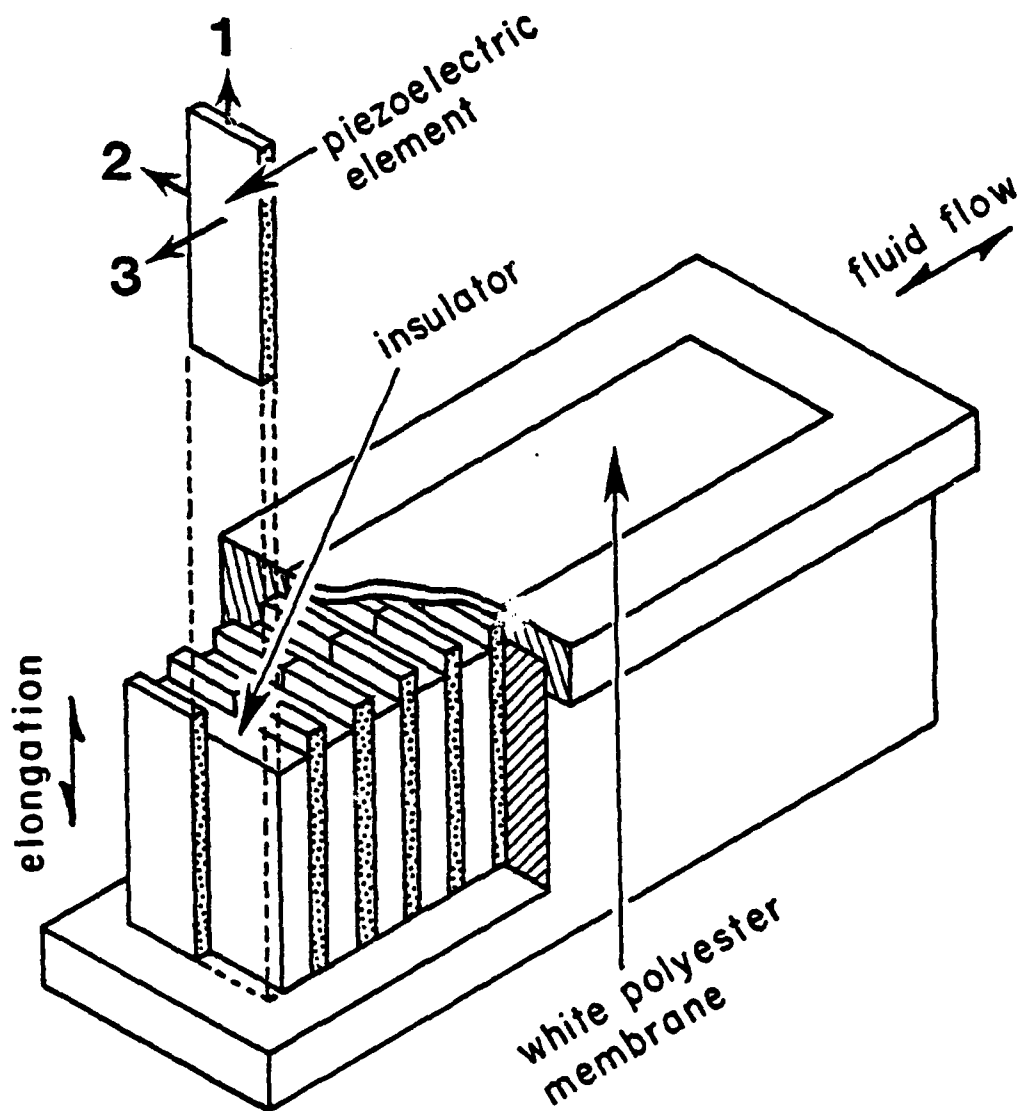
$$\phi = 360 \tau f \quad (12)$$

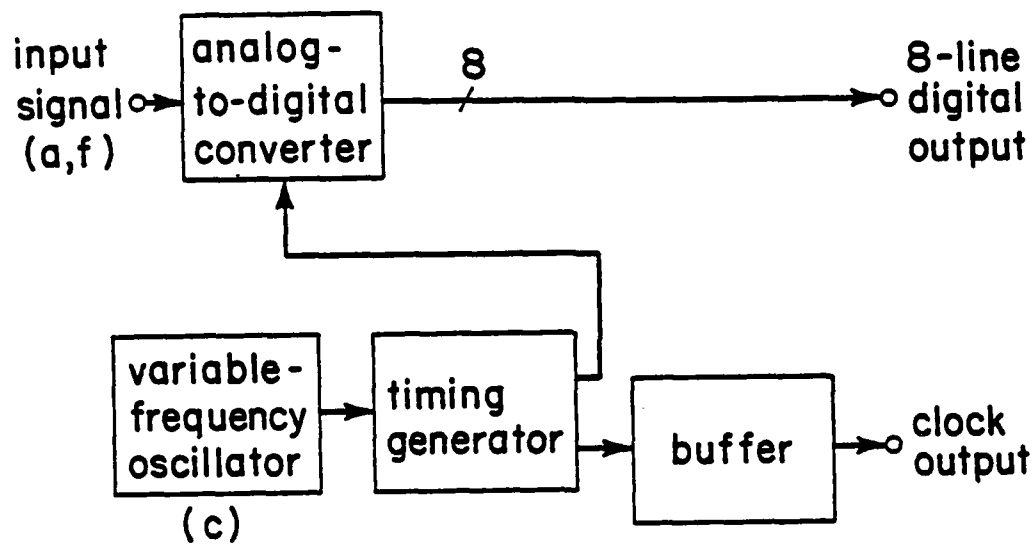
where τ is the measured phase delay in seconds at station x relative to $x = 0$. As Fig. 11 indicates, measured phase shift from Eq. (12) is in agreement with design values determined from Eq. (11).

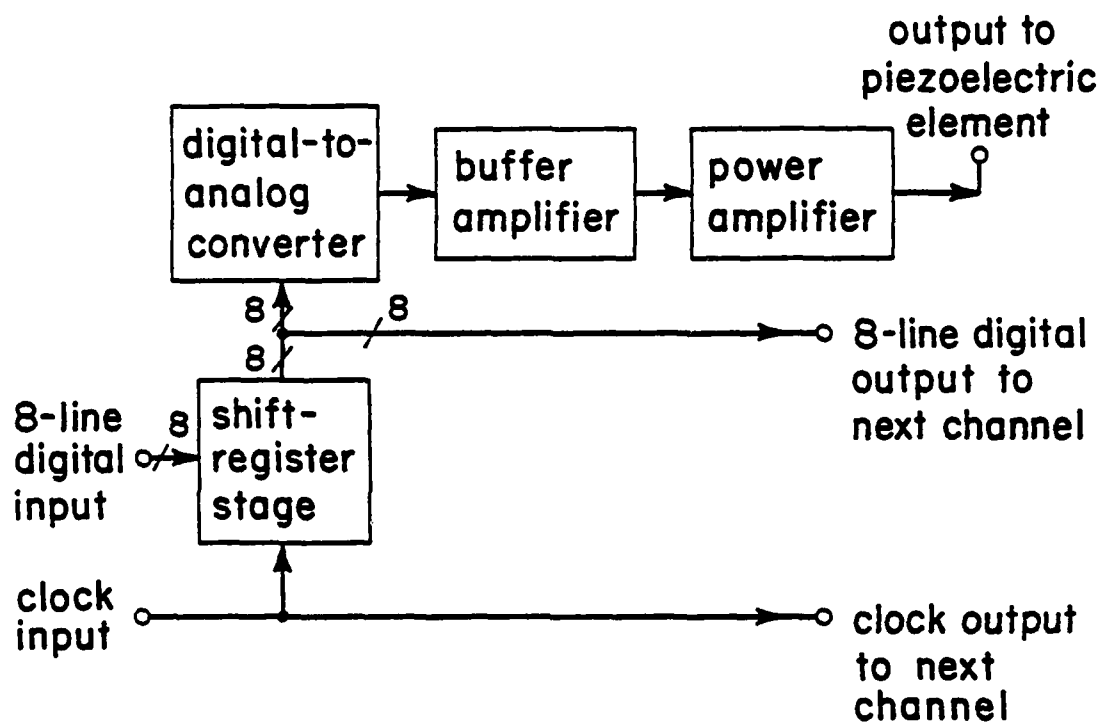
IV. CONCLUSIONS

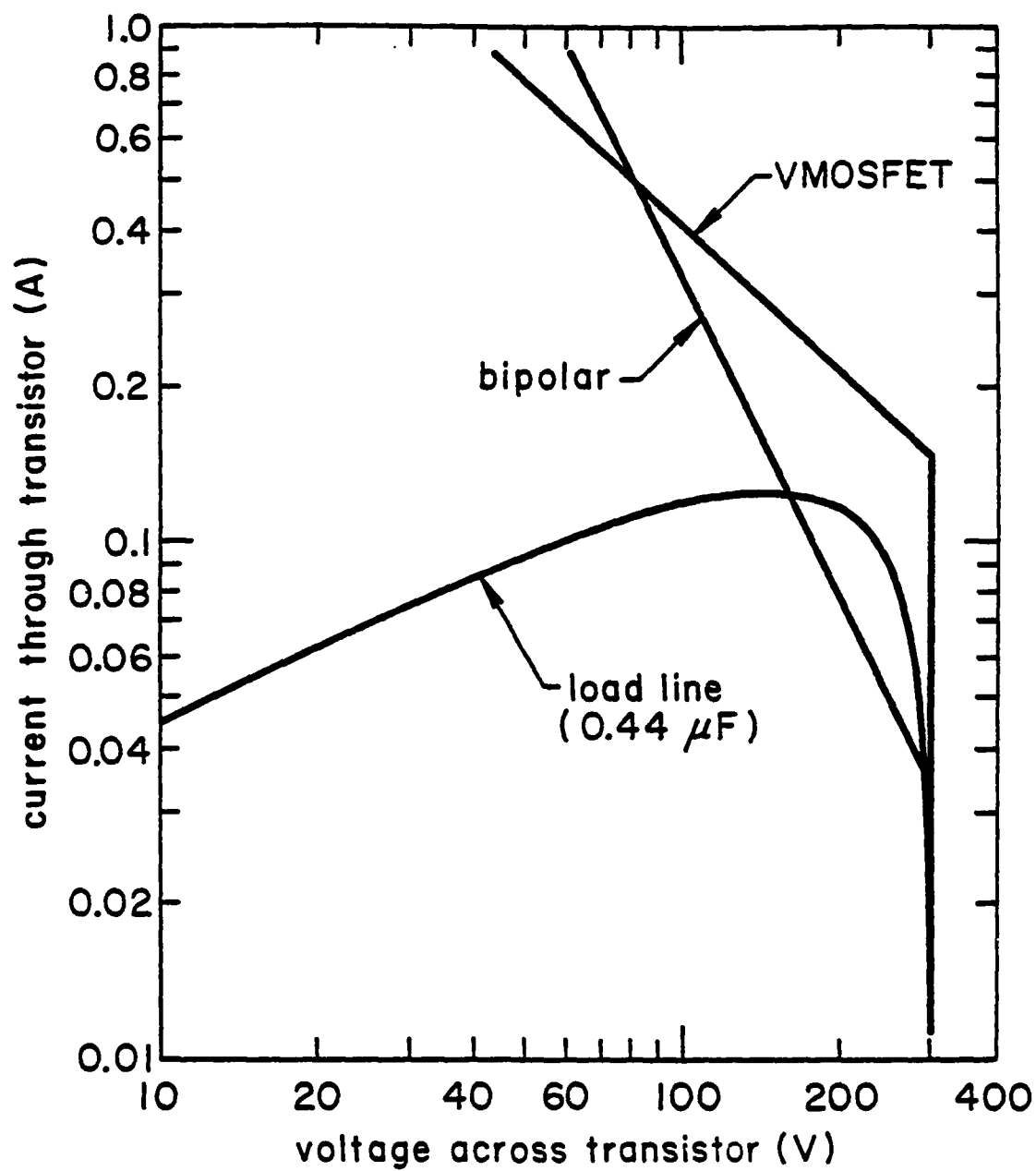
An active wall which generates short-wavelength traveling surface waves has been successfully designed and tested. The active wall essentially meets the design requirements outlined in Table IV, although the maximum displacement amplitude was approximately half of the design value.

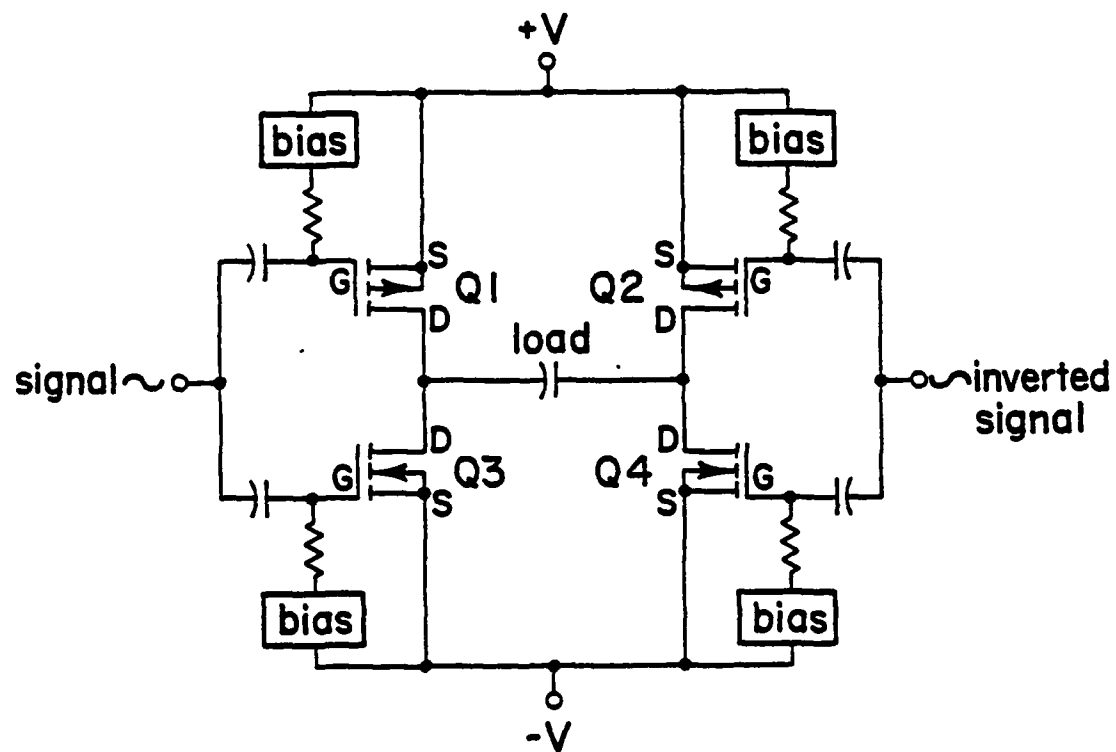
The electronic drive produced a 300-V amplitude signal across a 4.0-k Ω resistive load or 0.44- μ F capacitor. For the resistive load the power amplifier had flat frequency response; however, with a capacitive load response was identical with that of a current-fed parallel resonant circuit with a center frequency of 30.5 Hz and a quality factor (Q) of 2.56. In the present work, this anomaly was not a problem, but it should be corrected in future applications. Although response of the amplifier circuit driving piezoelectric ceramics was similar to that observed with a capacitive load, distortion caused by saturation of the ceramic elements appeared in the signal to the elements between 80 and 90-V amplitude. A possible solution to this problem may be in selection of a piezoelectric ceramic with a lower d_{31} constant but with more favorable values of large-signal characteristics.

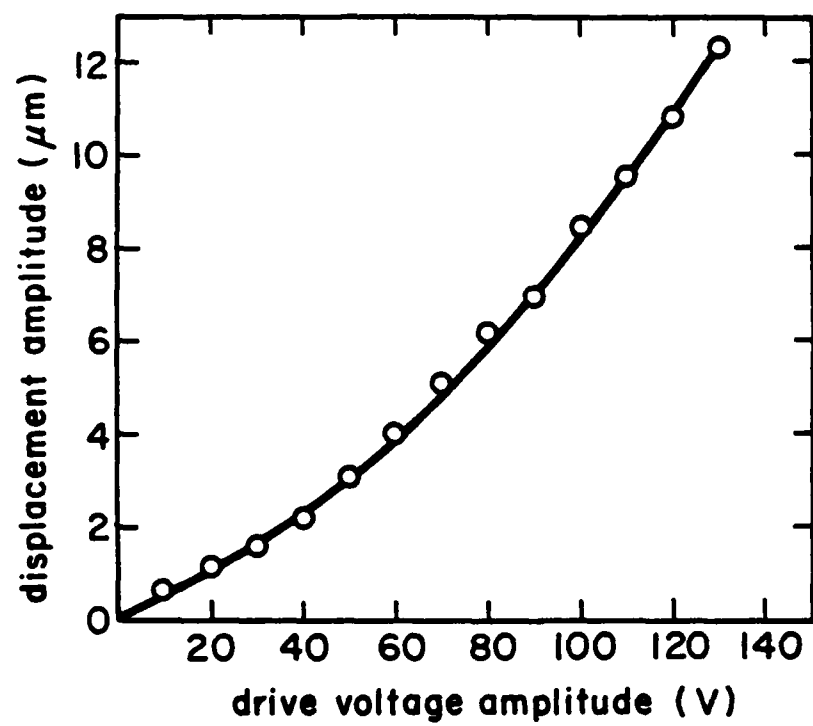


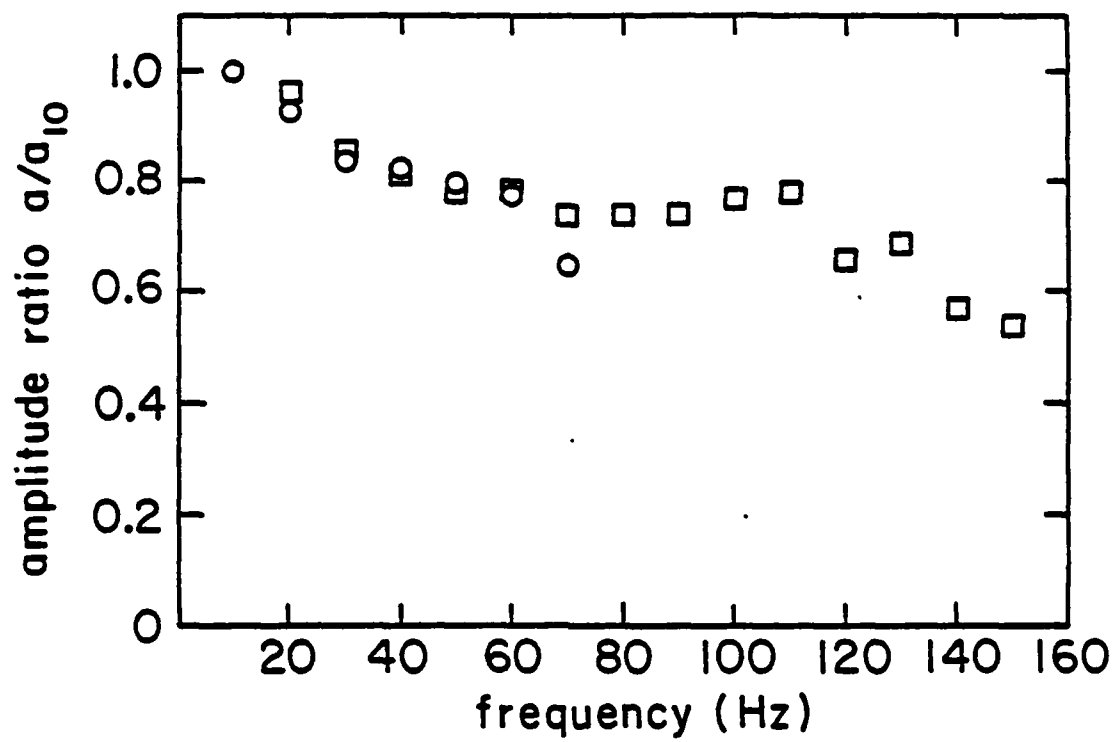


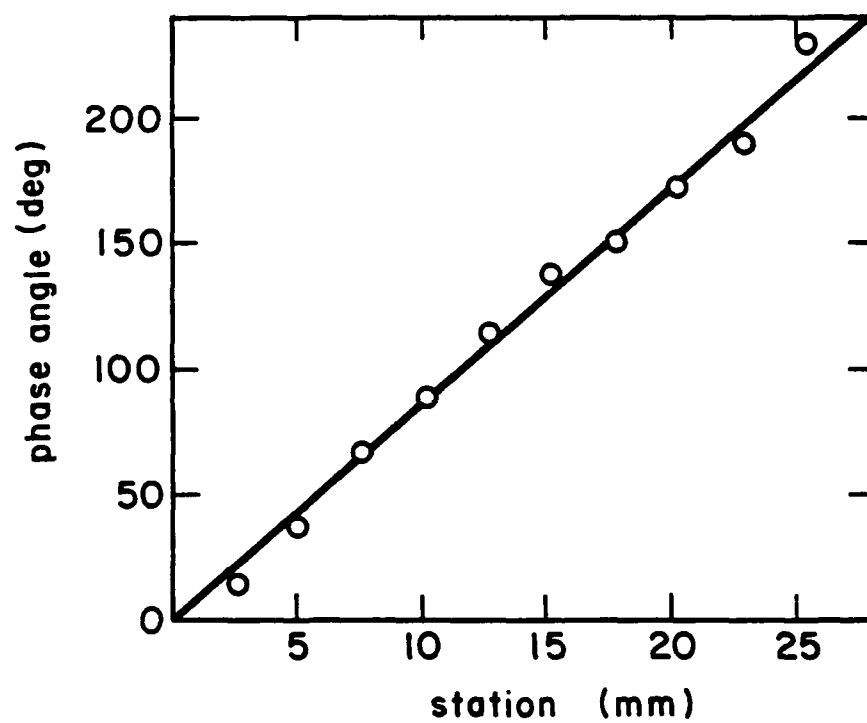












APPENDIX C

Design of a Low-Turbulence Water Tunnel

by

Joel T. Park
Southwest Research Institute

Design of a Low-Turbulence Water Tunnel

By

Joel T. Park

Southwest Research Institute

San Antonio, Texas 78284

INTRODUCTION

A low-turbulence water tunnel was designed and constructed for high velocity fluid mechanics research. A test section was constructed for boundary layer measurements with an active wall for both laminar and turbulent flows. The facility design incorporated an available pump and hydraulic drive motor. Figure 1 is a scale drawing of the water tunnel while Figure 2 is a photograph of the final assembly. The nomenclature of the various components is identified in Figure 1. The test section was nominally designed for a maximum velocity of 32.8 m/s (32.8 ft/s), and its cross section is rectangular with dimensions of 22.9 x 22.9 x 76.2 cm (9 x 9 x 30 in).

The design features of a number of facilities were reviewed for applicability to the new water tunnel. Some typical tunnels are listed in Table 1. The features of the Case tunnel, where a number of successful laminar boundary layer experiments have been performed [3,4], and the smaller Penn State tunnel [7] were included in the design. From Table 1, a reasonable design goal appeared to be a relative turbulence intensity of 0.1% in the longitudinal component. Additionally, some of the more recent concepts in contraction and settling chamber design have been incorporated to ensure optimum performance.

Since the SwRI tunnel is relatively small, the cost of the materials was not a major factor in the design. The Case tunnel [2], which is about the same size as the SwRI tunnel, is constructed from all aluminum. For the same length in the design, thinner 304 stainless plate is required; consequently, the total cost of 304 stainless steel and aluminum is nearly the same. Also, stainless steel is more corrosion resistant; therefore, it was selected as the primary material for the tunnel. The design pressure for the facility is 207 kPa (30 psi).

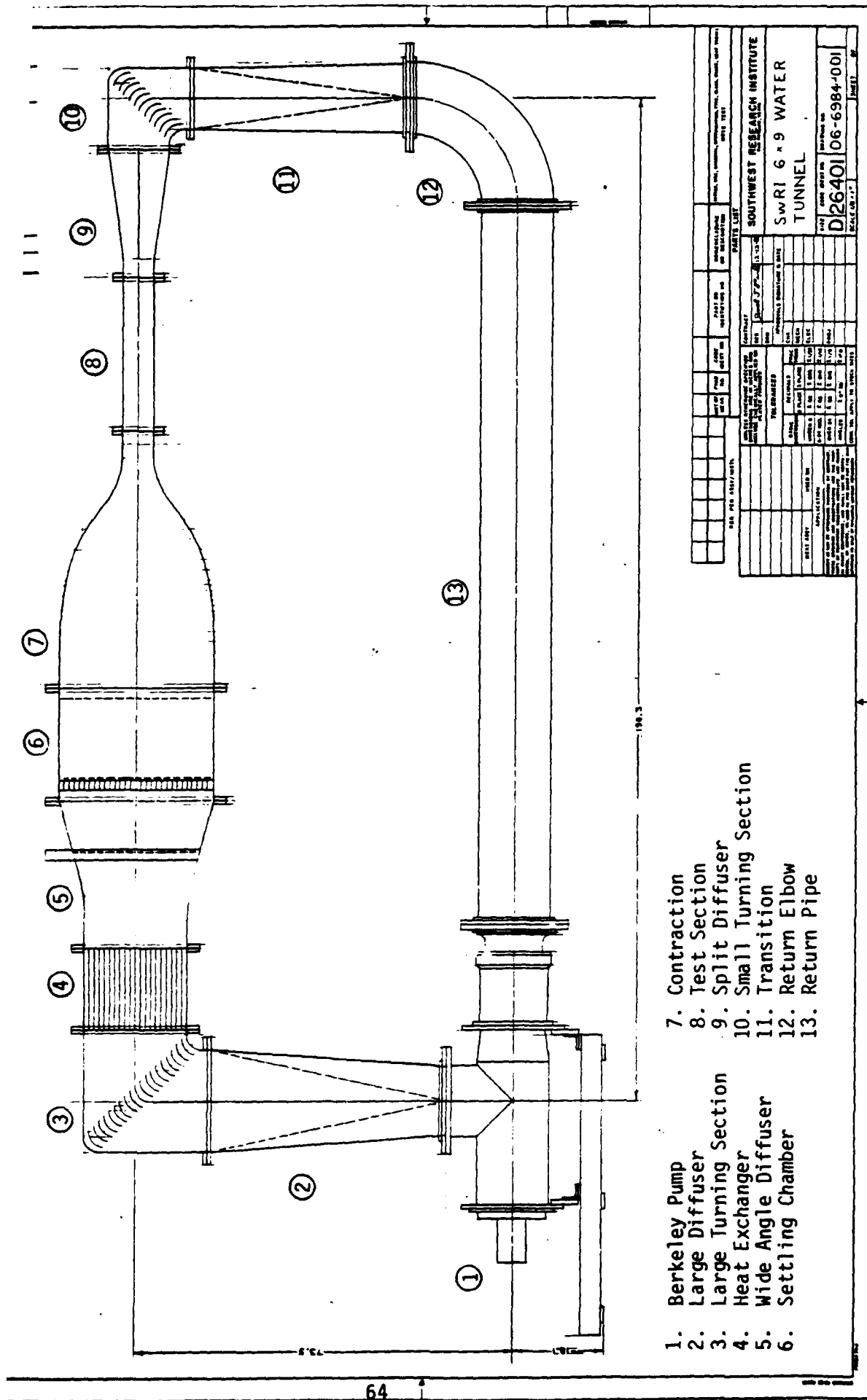


FIGURE 1. SCALE DRAWING OF LOW-TURBULENCE WATER TUNNEL AT SOUTHWEST RESEARCH INSTITUTE

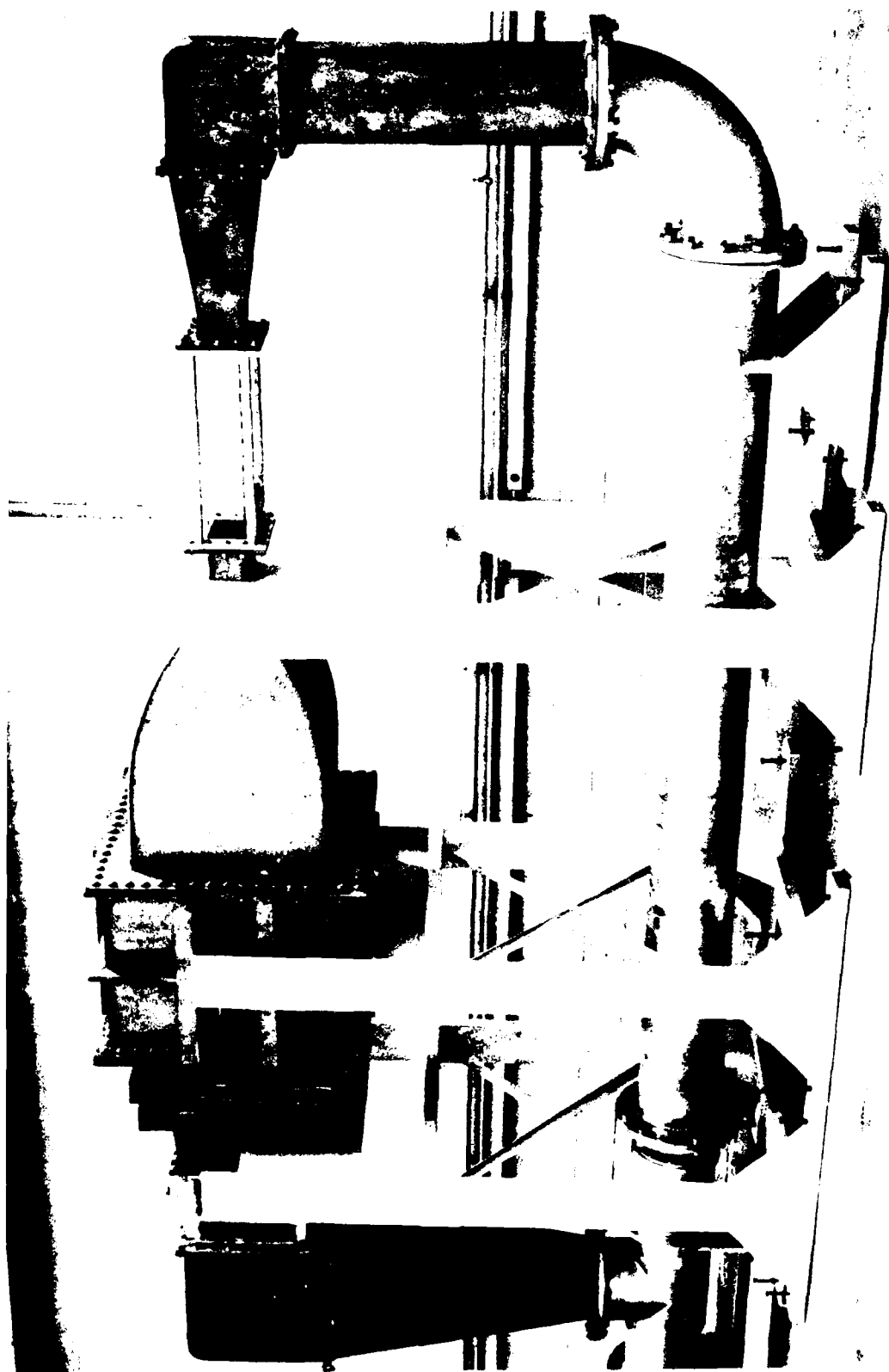


FIGURE 2. PHOTOGRAPH OF LOW-TURBULENCE WATER TUNNEL AT SOUTHWEST RESEARCH INSTITUTE

TABLE 5. INFLUENCE OF CONTRACTION ON FREESTREAM TURBULENCE
FOR A CONTRACTION AREA RATIO OF 16

Author	Ref.	Nozzle Design	L/D _i	$(\sigma_u/U)_i$ (%)	σ_{ue}/σ_{ui}	$(\sigma_u/U)_e/(\sigma_u/U)_i$
Batchelor	23	Theory			0.0255	0.002
Uberoi	24		0.83	2.5	1.11	0.069
Ramjee & Hussain	25	Batchelor-Shaw	0.75	3.8	2.26 ^a	0.142 ^a
Telapurkara & Ramjee	30	Thwaites	1.	3.1	2.33	0.145
Tan-atichat	28	Matched-Cubic	1.	2.29	1.06	0.066
				2.64	1.06	0.066
				2.90	1.16	0.073
				2.69	1.18	0.074
				2.05	1.26	0.079

^a Interpolated value

Hussain [25] reported that exit relative turbulence intensity, $(\sigma_u/U)_e$, was pendent of the inlet conditions from grid turbulence. Conclusions from the recent results of Tan-atichat [28] and Nagib, et al. [29] which were pri-ly from matched-cubic nozzles include the following:

- a. Optimum contraction ratio is 9
- b. L/D_i should be one
- c. Upstream integral scale and $(\sigma_u/U)_i$ influence $(\sigma_u/U)_e$ and other exit turbulence characteristics for large contractions
- d. Differences between matched-cubic and fifth order contours are insignificant.

ough some consensus exists among various researchers, some controversy remains the effects of contractions on turbulence.

Nagib, et al. [29] have formulated design charts for optimum turbulence ipulation with a matched-cubic nozzle of contraction ratio 9. These charts are ited to longitudinal turbulence intensities of $0.14 \leq (\sigma_u/U)_e \leq 0.32$ at the noz-exit. Although these charts overlap the range of interest, $0.1 \leq (\sigma_u/U)_e \leq 0.2$, s information became available after the contraction was designed and fabricated.

On the basis of the results of these previous investigators, a matched-ic profile was selected for the present application. The contraction ratio was sen as 16.67. This choice allows the flow within the settling chamber to be ve the critical Reynolds number for the screens and to maintain the loading on screens within their structural limits. The turbulence characteristics for ious nozzles with $C = 16$ are summarized in Table 5. Tan-atichat [28] provides following correlation for the turbulence reduction factor of a matched-cubic file

$$\sigma_{ue}/\sigma_{ui} = [(C-5)/6]^{1/2} \quad (12)$$

$$6 < C < 30.$$

- b. 6 screen frames including an entrance screen for the back pressure on the wide-angle diffuser
- c. Blank section 22.9 cm long (72 honeycomb mesh lengths)

The blank section and two screen frames, one adjacent to the honeycomb and the second downstream of the blank section, provide a decay distance of $x^+ = 120$ for the turbulence between the honeycomb-screen combination and the downstream screen. Also, each of the internal components is separated by a 3.2 mm (0.125 in) rubber gasket.

⑦ Contraction Section

A contraction section was designed in conjunction with the settling chamber for minimization of the turbulence in the test section. Linear rapid distortion theory [23] indicates that the turbulence reduction factor decreases monotonically with an increase in contraction ratio. For large contraction ratios the result is

$$(\sigma_{ue}/\sigma_{ui})^2 = [3/(4C^2)][\ln(4C^3)-1] \quad (11)$$

where C is the contraction area ratio. Since turbulence reduction factor goes to zero for large contraction ratios, eq. (11) implies that large contraction ratios are required for low-turbulence facilities.

Experimentally, Uberoi [24] and others demonstrated that the theory in eq. (11) is incorrect. The experimental results of Ramjee and Hussain [25] indicate that the optimum contraction ratio is 40 with no significant reductions in turbulence above about 20. Tsuge [26] has recently published a theory which is in agreement with experiment. His theory accounts for the amplification of large eddies which are ignored by the linear theory.

In addition to contraction ratio, other key factors in nozzle design are the length to inlet diameter ratio (L/D_i), and the characteristics of the upstream turbulence. In their experiments, Hussain and Ramjee [27] concluded that the matched-cubic contour was the best of four nozzles they tested, and Ramjee

steel screen that was purchased has a mesh size of 0.67 cm (1/38 in) and a wire diameter of 0.114 mm (4.5 mil). Thus, $\beta = 68.7\%$, $Re_d = 68.3$, and $Re_{dM} = 99.4$, while the critical Re_d from Schubauer, et al. [21] is 57.2 ($Re_{dM} = 83.2$).

The reduction in turbulence for the flow through n screens is given by the turbulence reduction factor from Dryden and Schubauer [22] as

$$\sigma_{un}/\sigma_{ui} = (1 + k)^{-n/2} \quad (9)$$

while Loehrke and Nagib [17] have observed the correlation

$$\sigma_{un}/\sigma_{ui} = (1 + k)^{-n/2.7}. \quad (10)$$

Equation (4) provides an estimate of the pressure drop coefficient. The estimates of k from this correlation and others are listed in Table 4. The turbulence reduction factors from eqs. (9) and (10) for $k = 0.662$ and four screens ($n = 4$) are, respectively, 0.362 and 0.471. On the basis of these estimates, the total turbulence reduction factor for the settling chamber is 0.061 to 0.15.

The screen frames were fabricated from 304 stainless steel square tube with sides of 7.62 cm (3 in) and wall thickness of 3.2 mm (0.125 in). The frames have sufficient strength to support the loading of the screens, and they provide a space of $l/M = 114$ for the decay of turbulence between screens. The loading of the screens was estimated from Domholdt [2]. The screens are preloaded by 1750 N/m (10 lb/in) in one direction and bonded to the frames. With this preload, the screen deflection is estimated to be less than one percent of the channel width.

The settling chamber is a square shell of 6.4 mm (0.25 in) stainless plate with flanges and ribs. The internal components are sandwiched between the flanges of the wide-angle diffuser and contraction section. The flow through area is 76.2 cm square by 76.2 cm (30 in) long. The internal components include the following:

- a. Honeycomb with hexagonal cells, 3.2 mm x 5.08 mm long

installed. The honeycomb eventually corroded away, and it was replaced by stainless steel [6]. The honeycomb at Penn State has hexagonal cells with width across flats of 0.56 cm by 47.62 cm long (0.22 x 18.75 in) or an ℓ/M of 85. The cells in the NBS tunnel [5], which are also stainless steel, are 0.32 x 61 cm (1.25 x 24 in) or an ℓ/M of 192. The theoretical requirement for the large ℓ/M [5] is based upon fully developed turbulent flow in the cells.

Since the cost of thick honeycomb appeared to be excessive for the present application, a more economical approach with a combination of screens and honeycomb suggested by Loehrke and Nagib [17,19] was adopted. This method has been applied in modifications to the Case tunnel which now contains screens, honeycomb, and foam [4].

The important design parameters in the selection of honeycomb are length to mesh size ratio (ℓ/M) and the mesh Reynolds number, $Re_M = U_s M/\nu$, where U_s is the settling chamber velocity. Honeycomb is effective in removing swirl and dampening the lateral turbulence scales, and it should have $\ell/M \geq 10$ [19]. The heat exchanger functions as a honeycomb for the removal of large scales while the honeycomb in the settling chamber manipulates primarily the smaller scales. The honeycomb in the settling chamber is fabricated from 304 stainless steel foil with a thickness of 76 μm (3 mil), and the cell size is 3.2 mm by 50.8 mm long (0.125 x 2 in). $\ell/M = 16$. The Reynolds number, Re_M , at the design test section velocity is 1900.

One of the honeycomb configurations (plastic soda straws) tested by Loehrke and Nagib [17,19] was near the design condition of the present honeycomb. In those experiments a screen near the honeycomb at $\Delta x/M < 5.7$ significantly reduced the standard deviation or rms velocity, σ_{ue}/σ_{ui} , or turbulence production factor was 0.31 without the screen and 0.17 with the screen.

According to Lumley and McMahon [18], the decay rate of turbulence through screens and honeycomb at a turbulent Reynolds number is higher. A recent review of flow through screens is by Laws and Livesey [20]. The critical Reynolds number for screens is based upon wire diameter, d . For a Reynolds number based upon grid velocity, the critical value of $Re_{dM} = U_s d/(\beta\nu)$ is 80 [12] while Schubauer, et al. [21] measured critical $Re_d = U_s d/\nu$ as a function of solidity. The stainless

23.9°C (75°F). The estimated power dissipation of the heat exchanger is 10.6 kW (36,000 Btu/hr).

The heat exchanger is constructed from all aluminum. The tube bundle consists of 247 tubes with an outside diameter of 2.54 cm (1 in), wall thickness of 0.89 mm (0.035 in), and length of 40.6 cm (16 in). The tubes are welded to 19-mm (0.75 in) thick tube sheets which also serve as flanges. The hole pattern in the tube sheet is a equilateral triangle with center to center distance of 3.18 cm (1.25 in). The shell is also 19-mm (0.75 in) plate with an inside square cross section of 48.9 cm (19.25 in).

As an effective turbulence manipulator, the heat exchanger should have the largest possible open-area ratio, β . According to Morgan [16], the open-area ratio of screen should be larger than 0.5; otherwise, a flow instability will occur. Also, Loehrke and Nagib [17] have noted anomalous behavior for low- β ($\beta = 0.30$) perforated plates. From geometry, the local open-area ratio for a perforated plate with a triangular hole pattern is

$$\beta = (\pi \sqrt{3}/6)(d/\ell)^2 \quad (7)$$

where d is the hole diameter and ℓ is the centerline distance between holes, and the average value is

$$\beta = n\pi d^2/(4A) \quad (8)$$

where n is the number of holes and A is the inside cross-sectional area of the mating ducts, the wide-angle diffuser and large turning section. The local and average values of the present design are, respectively, 50% and 42%.

⑥ Settling Chamber

More recently turbulence in water tunnels has been managed with installation of honeycomb in the settling chamber. The large water tunnel at Penn State required large wire-diameter screens on the basis of strength requirements which caused vortex shedding problems [18]. Consequently, a design criteria was developed by Lumley and McMahon [18] for honeycomb, and an aluminum honeycomb

of zero. The gap/chord ratio is slightly larger for thicker vanes [15]. Pope [9] recommends a tunnel width/gap, w/h , ratio greater than six and a large chord. For convenience, the large turning section was divided into twenty increments with 19 vanes, and the small turning section into twelve with 11 vanes. The resulting increment across the width of the turning sections is 2.54 cm (1 in). The chord was then selected as four times this value or 10.2 cm (4 in). From geometry the chord and radius are related by

$$c/r = 2 \sin (\theta / 2) \quad (6)$$

where θ is the angle of the arc which is 85° for an optimum turning vane. From eq. (6) the radius is 7.5 cm (2.96 in).

The vanes were then fabricated from 15.2 cm (6 in) diameter stainless-steel tubing with a wall thickness of 3.2 mm (0.125 in). The upper and lower walls of the turning sections were rolled from stainless-steel plate with the same corner radius. In the final assembly, the gap/chord ratio across the corners is 0.36. The tunnel width/gap ratios for the large and small turns are, respectively, 14.1 and 8.5. The plate thickness in the large turn is 9.5 mm (0.375 in), and in the small turn 6.4 mm (0.25 in).

④ Heat Exchanger

A heat exchanger was designed for removal of heat from frictional heating. The device also functions as a turbulence manipulator, i.e. coarse honeycomb, for dampening large scale turbulence. The device was designed with approximately the same area for heat transfer as that of Domholdt [2] with some additional improvements for efficiency.

The heat exchanger essentially functions as a counter-flow heat exchanger. The coolant water enters a manifold at the bottom downstream end of the heat exchanger, is routed over the tube bundle by two vertical baffle plates, and exits a second manifold at the top upstream end. Preliminary heat transfer calculations indicate that the tunnel temperature will be maintained at 26.6°C (80°F) for the maximum design speed with a coolant flow of 1.3 l/s (20 gpm) at

50.8 cm (20 in) and 76.2 cm (30 in), or the area ratio is 2.25. From eq. (3) the number of screens is then three for a $k = 0.725$. The dimensions of the first two screens were computed from eq. (2) as 58.21 cm (22.92 in) and 66.71 cm (26.27 in).

The total length of the wide-angle diffuser was chosen as 71.8 cm (28.25 in). The first screen is located at 37.5 cm (14.8 in) from the entrance. This distance, which is approximately 16 tube diameters from the heat exchanger, was selected to ensure adequate mixing of the jets from the heat exchanger before the first screen is encountered.

The diffuser was designed so that the first two screens could be removed without emptying the tunnel. The third screen is located in the entrance of the settling chamber. The wall thickness of the diffuser is 9.5 mm (0.375 in).

⑨ Split Diffuser. The diffuser downstream of the test section is similar in design to that of Domholdt [2]. The inlet and outlet inside dimensions are, respectively, 15.2 x 22.9 cm (6 x 9 in) and 30.5 cm (12 in) square. The total angle is 16° between the upper and lower surfaces with a 3.2 mm (0.125 in) splitter plate in the center while total angle for an equivalent conical diffuser is 9.9° . The length of the divergent section and splitter plate is 54.2 cm (21.35 in). A short parallel section is included upstream of the splitter plate so that the total length of the diffuser is 63.5 cm (25 in). The wall thickness is 6.4 mm (0.25 in).

⑪ Transition. The transition in the vertical return has the same inlet and outlet areas. The dimensions of the inlet and outlet are, respectively, 30.5 cm (12 in) square and 34.3 cm (13.5 in) in diameter. The section is 108 cm (42.5 in) long with a 6.4 mm (0.25 in) wall thickness.

③ & ⑩ Turning Sections

According to Bradshaw and Pankhurst [12] and Pankhurst and Holder [15], the most efficient turning section consists of turning vanes fabricated from sheet metal with a circular arc. The optimum vane has a gap/chord, h/c , ratio of 0.25 for thin vanes, a leading edge angle of 5° , and a trailing edge angle

TABLE 4. PRESSURE DROP COEFFICIENT FOR SCREENS IN
SETTLING CHAMBER OF WATER TUNNEL

Author	Ref.	k^a	C_1^a	C_1^b	K^b
Nagib	11	$C_1(1-\beta)/\beta^2$	1	1.	0.662
Bradshaw & Pankhurst	12		$9\text{Re}_d M^{-0.4}$	1.43	0.947
	12		$6.5\text{Re}_d M^{-1/3}$	1.40	0.929
Pinker & Herbert	13	$C_1(1-\beta^2)/\beta^2$	Fig. 15	0.8	0.893
Baines & Peterson	14	$C_1(1-\beta)^2/\beta^2$	1	1.	0.207
	14	Fig. 3	-----	----	0.6

$a \quad \beta = (1 - d/M)^2, \text{Re}_d M = U_s d / (\beta v)$

$b \quad d = 0.114 \text{ mm } (0.0045 \text{ in}), M = 0.668 \text{ mm } (1/38 \text{ in}),$
 $\beta = 68.7 \%, \text{Re}_d M = 99$

The wall thickness of the large diffuser is 9.5 mm (0.375 in).

⑤ Wide Angle Diffuser. A 30° wide-angle diffuser was incorporated in the design upstream of the settling chamber for a reduction in length. Screens were included to prevent flow separation and to reduce the level of turbulence. The section was designed by the method of Schubauer and Spangenberg [10] so that the pressure recovery was balanced by the pressure loss of the screen. The area ratio at the screen location is given by [10]

$$A_i/A_{i-1} = (k_i + 1)^{1/2} \quad (2)$$
$$i = 1, 2, \dots, n$$

where A_i is the area of the i th screen and k_i is the pressure drop coefficient of the screen. For n screens with the same k_i the total area ratio of the diffuser is

$$A_n/A_0 = (k + 1)^{n/2}. \quad (3)$$

The pressure drop coefficient recommended by Nagib [11] is given by

$$k = (1 - \beta)/\beta^2 \quad (4)$$

which is an unpublished result valid for $0.5 < \beta < 0.7$ where the open-area ratio of the screen is

$$\beta = (1 - d/M)^2 \quad (5)$$

d is the wire diameter and M is the mesh length. The open-area ratio is related to solidity, σ , by $\beta = 1 - \sigma$. Other available correlations for the pressure drop correlation are summarized in Table 4, but screens will be discussed in more detail in a subsequent section on the settling chamber.

For the purpose of the design calculations, a mesh size of 0.635 mm (1/40 in) and a wire diameter of 0.114 mm (0.0045 in) were selected although a slightly larger mesh was purchased. The inlet and outlet dimensions of the diffuser are

TABLE 2. PERFORMANCE CHARACTERISTICS OF
BERKELEY VERTICAL MIXED FLOW PUMP
MODEL M12-12

Flowrate	0.315	m ³ /s	(5000 gpm)
Rotational Rate	1760	rpm	
Power Required	50	kW	(67 hp)
Submergence Required	0.6	m	(2 ft)
Total Dynamic Head	125	kPa	(42 ft of water)

TABLE 3. PERFORMANCE CHARACTERISTICS OF
DENISON VANE TYPE HYDRAULIC MOTOR
MODEL M3D-138-21N

Maximum Power	65	kW	(87 hp)
Rotational Rate	2000	rpm	
Flowrate	4.7	ℓ/s	(75 gpm)
Maximum Pressure	13.8	MPa	(2000 psi)

DESIGN DETAILS

① Pump¹

The water tunnel was designed around an available Berkeley mixed flow pump. The pump is powered with a Denison hydraulic motor so that tunnel speed is controlled by hydraulics. Speed control can be accomplished with a manual valve or with a Koehring-Pegasus model 1282A two-stage servovalve for remote control. The specifications of the pump and motor are summarized in Tables 2 and 3. The total dynamic head of the pump is more than 5 times the estimated pressure loss of the tunnel.

The pump is fitted with American Standards Association (ASA B16.1 and B16.5) slip-on flanges for 14-inch diameter pipe (35.6 cm). The return leg of the water tunnel at pump inlet contains a 14-inch diameter pipe ⑬ and standard long-radius elbow ⑫. The elbow, pipe, and pump are galvanized steel.

Diffusers

② Large Diffuser. The optimum divergence angle for minimum power loss in diffuser is given by Pope [9] as

$$\tan (\alpha/2) = \sqrt{f/4.8} \quad (1)$$

where α is the total divergence angle and f is the pipe friction factor. In the present application, the optimum divergence angle is about 6°. In the opinion of Dumholdt [2], an 8° angle is adequate; consequently, the 8° value was accepted to reduce the height of the tunnel.

The diffuser also serves as a transition section from a circle to a square. The inlet and outlet inside dimensions are, respectively, 34.2 cm (13.5 in) diameter and 50.8 cm (20 in) square. The resulting length for an 8° divergence of the sides is 1.18 m (46.5 in).

¹ Circled numbers correspond to those of the tunnel drawing in Figure 1.

As Figure 2 indicates, the water tunnel is supported vertically by three large steel frames, a small steel frame, and the support stand for the pump. The dry mass of the facility excluding the support structure is 2,400 kg (5,300 lbs), the total mass excluding the support structure is 4,900 kg (10,700 lbs), and the water volume is 2.45 m³ (650 gal). The tunnel is supported on twenty Unisorb model LR750 machinery mounts with leveling screws for vibration isolation. The total height of the tunnel centerline to centerline is 1.9 m (73.5 in) while the horizontal centerline length is 5.2 m (204 in).

TABLE 1. LIST OF TYPICAL U.S. WATER TUNNELS

Organization/Location	Ref.	Test Section Dimensions (cm)	Contraction		Maximum Velocity (m/s)	Relative Turbulence Intensity (%)
			Area Ratio	Length/ Diameter		
1. California Institute of Technology Pasadena, California	1	35.6 D	20	----	----	0.04
2. Case Western Reserve University Cleveland, Ohio	2,3,4	15 x 23 x 39	25	1.09	12	0.2
3. National Bureau of Standards Gaithersburg, Maryland	5	61 D x 305	9	----	6.1	0.1
4. Pennsylvania State University State College, Pennsylvania	6 7	122 D x 427 30.5 D x 76	9 9	1.67 1.67	18.3 24.4	0.13 ---
5. Naval Ocean Systems Center San Diego, California	8	30.5 D x 91	7.5	---	19.	0.1

From the range of experimental values in Table 5, the estimated turbulence reduction factor for the contraction and settling chamber combination is $0.065 \leq \sigma_{ue}/\sigma_{ui} \leq 0.34$ or the ratio of relative intensities is $0.0039 < (\sigma_u/U)_e/(\sigma_u/U)_i < 0.020$. Thus if $(\sigma_u/U)_i$ entering the settling chamber is no more than 10%, the relative turbulence intensity of the water tunnel should be within the design goal of 0.2% in the test section for a properly designed contraction.

The contraction was designed from the procedure of Morel [31,32]. Morel's design curves for an axisymmetric nozzle [31] were from a numerical finite-difference solution of Euler's equations. He performed calculations on six power-law shapes, orders two through five, and concluded that the matched-cubic shape was the best. The design procedures have the following restrictions:

$$C_{pi} > 0.1$$

$$0.75 \leq L/D_i \leq 1.25$$

$$C_{pe} < 0.1$$

$$0.2 \leq X_m/L \leq 0.8$$

$$2 \leq C \leq 25$$

where L is the contraction length, D_i is the inlet diameter, and X_m is the match point of cubic curves. The pressure coefficients C_{pe} and C_{pi} are defined as follows:

$$C_{pe} = 1 - (U_\infty/U_{we})^2 \quad (13a)$$

$$C_{pi} = 1 - (U_{wi}/U_s)^2 \quad (13b)$$

where U_∞ is the test section velocity, U_s is the settling chamber velocity, and U_{wi} and U_{we} are the inlet and exit velocities at the wall. The pressure coefficients are a measure of the velocity profile flatness, and they are chosen in the design method.

The following is a brief summary of the design method where equation and figure numbers refer to Morel [31]:

- a. Choose C , C_{pe} , and C_{pi}

- b. Compute equivalent diameters from $D = 2\sqrt{A/\pi}$
- c. Diminish C_{pi} by 30%
- d. Determine F_e and G_i from Fig. 10 and 11
- e. Compute X_m/L from eq. (10) or Fig. 12
- f. Compute L/D_i from eq. (8b)
- g. Check pressure gradient for possible separation
- h. Add straight sections to the entrance of at least $0.2D_i$ and to the exit of $0.3D_e$.

The total nozzle length is then

$$L_t = L + a_i D_i + a_e D_e. \quad (14)$$

Since the velocity is relatively low in this application, the critical separation criterion may be the influence of an adverse pressure gradient on a laminar boundary layer. The boundary layer separation criterion is from Stratford [33], and pressure coefficient form for laminar separation in contraction coordinates is given by eq. (14) in Morel [32]. Separation criteria determined the entrance length between the contraction and last screen in the present design.

The equations for the contraction coordinates are given by eqs. (10a) and (10b) in Morel [32]. The versions of these equations in Morel [31], eqs. (5a) and (5b), are incorrect. The dimensions of the final design are as follows:

Equivalent inlet diameter	85.98 cm	33.85 in
Equivalent exit diameter	21.06	8.29
Match point	74.52	29.34
Contraction Length	103.75	40.85
Entrance Length	17.78	7.0

Exit length	6.35	2.5
Total length	127.86	50.34

The contraction section was rolled from 6.4 mm (0.25 in) stainless steel plate and welded. The profile and layout coordinates for fabrication were generated by a computer program. Obtaining the layout coordinates for the cubic curve required a numerical integration. The interior surface of the contraction was polished to a measured finish of 0.30 μm (12 μin) rms.

⑧ Test Section

The cross-sectional area of the tunnel was determined by the design speed of 10 m/s and maximum flowrate of the pump. The dimensions are 15.2 cm high by 22.9 cm wide by 76.2 cm long (6 x 9 x 30 in). The aspect ratio of the cross-section is near the $\sqrt{2}$ value for traditional wind tunnels [12], and the length is sufficient for most boundary layer research. The tunnel design will readily accommodate other test section lengths. Figure 3 is a photograph of the assembled test section.

The test section includes a flat plate with a bleed slot for removal of the tunnel boundary layer. The concept is similar to that of the Case tunnel where several successful boundary layer experiments have been performed [3,4]. This design was chosen because it will allow installation of externally bulky devices such as active-wall devices, manifolds for boundary-layer injection, surface-mounted hot-film probes, and electro-magnets for driving vibrating ribbons.

The top and sides of the test section are fabricated from Plexiglas for flow visualization and laser Doppler anemometer (LDA) measurements. The bottom flat plate was machined from aluminum and plated with Tufra L-4, a teflon coating from General Magnaplate Corporation. The flow side of the plate was polished to a finish of 0.15 μm (6 μin) rms, but the final finish with the Tufra is 0.38 μm (15 μin) rms. The nose of the plate is an ellipse with a length/thickness ratio of 2.86, and it is located 5.08 cm (2 in) from the entrance. The dimensions of the plate are 69.2 cm long by 22.9 cm wide by 1.78 cm thick (27.25 x 9 x 0.7 in). The flanges were machined from 1.9 cm (0.75 in) aluminum

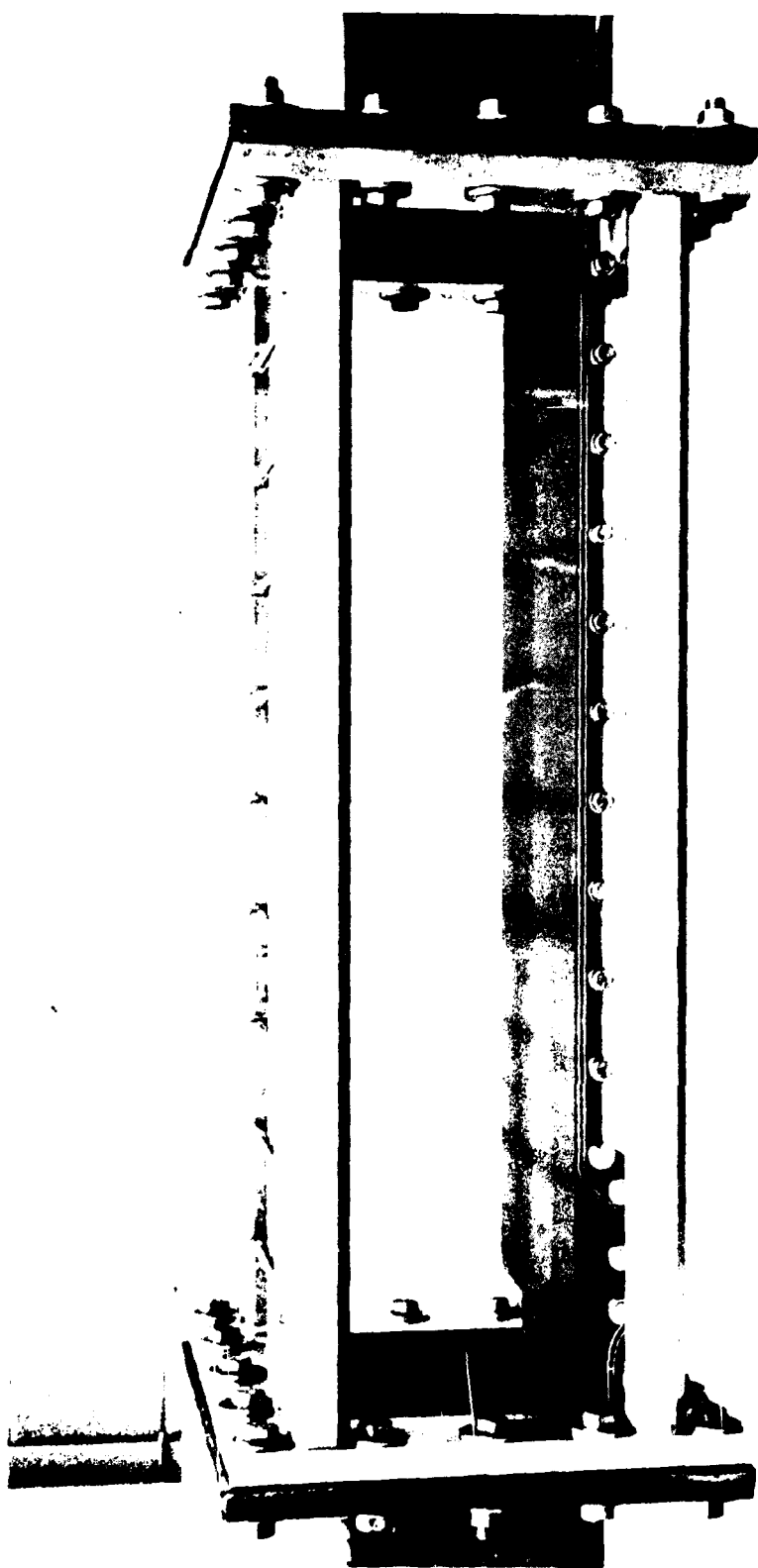


FIGURE 3. PHOTOGRAPH OF TEST SECTION IN LOW-TURBULENCE
WATER TUNNEL AT SOUTHWEST RESEARCH INSTITUTE

plate and anodized. Since the flat plate protrudes into the flow, the exit dimensions of the test section are 13.7 cm high and 22.9 cm wide (5.4 x 9 in). All mating surfaces are sealed with O-rings so that the test section can be readily disassembled.

CONCLUSIONS AND RECOMMENDATIONS

A low-turbulence water tunnel has been designed and constructed for boundary layer experiments. The latest available information on design has been incorporated in the facility. The nominal design velocity is 10 m/s (32.8 ft/s). The test section has three Plexiglas sides for flow visualization and LDA measurements, and the fourth side is a polished aluminum plate with a Tufram coating for boundary layer measurements. A bleed slot is included in the test section for removal of the tunnel boundary layer.

Turbulence in the test section and its flow profile are controlled by a settling chamber and matched-cubic contraction section. The settling chamber contains six stainless steel screens with a fine mesh and large open area ratio, and the contraction has a polished interior surface. Estimates on the basis of other experimental results indicate that the relative turbulence intensity in the test section should be between 0.04 and 0.2% if the entrance turbulence level to the settling chamber is less than 10%. According to Nagib [11] a relative longitudinal turbulence intensity of 0.2% should be readily attainable with the current design. Performance characteristics in the near future will be measured with hot-film anemometry.

An alternate approach in tunnel design would be to select a smaller contraction ratio and thicker honeycomb. As Table 1 indicates other successful facilities have been built with a contraction ratio of 9. Although the cost of the honeycomb would increase substantially, potential reductions in cost would result from the following:

- a. Smaller contraction
- b. Smaller settling chamber
- c. No wide-angle diffuser
- d. No screens.

Preliminary calculations indicate that a properly designed honeycomb without screens will produce the same relative turbulence intensity in the test

section if that which enters the settling chamber were the same. Estimates for the current design with $C = 9$ indicate that a cell size of 3.2 mm by 152 mm ($l/M = 48$) would be reasonable. The Reynolds numbers based on mesh size and length are $Re_M = 3,500$ and $Re_l = 1.7 \times 10^5$. From Fig. 2 of Lumley and McMahon [18] the pressure drop coefficient is 2.2, and from Fig. 1 the turbulence reduction factor is probably less than 0.2. From eq. (12) the turbulence reduction factor for the contraction with $C = 9$ is 0.82, or the total for the honeycomb and contraction will be less than 0.16. If the turbulence level entering the honeycomb were less than 10%, the relative turbulence intensity in the test section would be less than 0.2%, which is the maximum estimate for the present design with $C = 16.7$.

A properly designed settling chamber requires knowledge of the upstream turbulence characteristics which are not known for a new facility design. Also, the results from various experimenters which were applied in the current calculations are not in agreement. For example, the low and high values of turbulence reduction factor for the various components yield an estimated relative turbulence intensity between 0.04 and 0.2% in the current design with $C = 16.7$. Consequently, measurements in the test section of the completed facility are required for validation of a design.

The cost of the honeycomb for a $C = 9$ design with a cell size of 3.2 mm and cell length of 152 mm can be estimated from the cost of the honeycomb for the SwRI tunnel. At 65¢ per cubic inch, the cost for the $C = 9$ design would be approximately \$2000 in comparison to \$1200 for the SwRI tunnel. Although the price of the honeycomb would double, other cost benefits may be possible from the simplicity in design for a contraction ratio of 9.

REFERENCES

1. H. W. Liepmann, G. L. Brown, and D. M. Nosenchuck, "Control of Laminar-Instability Waves Using a New Technique," Journal of Fluid Mechanics, 118: 187-200 (1982).
2. Lowell C. Domholdt, "The Design and Performance of a Low-Turbulence Water Tunnel," Ph.D. Dissertation, Case Institute of Technology, Cleveland, Ohio (1963).
3. A. J. Strazisar, E. Reshotko, and J. M. Pahl, "Experimental Study of The Stability of Heated Laminar Boundary Layers in Water," Journal of Fluid Mechanics, 83: 225-247 (1977).
4. Hyoun-Woo Shin, "Experimental Study of The Effects of Surface Roughness on Laminar Boundary Layer Stability in Water," Ph.D. Dissertation, Case Western Reserve University, Cleveland, Ohio (1982).
5. P. S. Klebanoff, N. E. Mease, and W. R. Rowland, "An Experimental Investigation of Drag Reduction With Compliant Surfaces," in Drag Reduction Symposium edited by Michael M. Reischman, Office of Naval Research, Arlington, Virginia (1982).
6. Basil E. Robbins, "Water Tunnel Turbulence Measurements Behind a Honeycomb," Journal of Hydronautics, 12: 122-128 (1978).
7. Roger L. Steele, "The Design of a Small Water Tunnel," Master of Science Thesis, Department of Mechanical Engineering, The Pennsylvania State University, State College, Pennsylvania (1951).
8. R. J. Hansen, D. L. Hunston, C. C. Ni, M. M. Reischman, and J. W. Hoyt, "Hydrodynamic Drag and Surface Deformations Generated by Liquid Flows Over Flexible Surfaces," in Viscous Flow Drag Reduction edited by Gary R. Hough (American Institute of Aeronautics and Astronautics, New York, 1980) pp. 439-452.

9. Alan Pope, Wind-Tunnel Testing, Second Edition, (John Wiley and Sons, Inc., New York, 1954).
10. G. B. Shubauer and W. G. Spangenberg, "Effect of Screens in Wide-Angle Diffuser," National Advisory Committee for Aeronautics Report 949 (1949).
11. H. M. Nagib (private communication).
12. P. Bradshaw and R. C. Pankhurst, "The Design of Low-Speed Wind Tunnels," Progress in Aeronautical Sciences, 5: 1-69 (1964).
13. R. A. Pinker and M. V. Herbert, "Pressure Loss Associated With Compressible Flow Through Square-Mesh Wire Gauzes," Journal Mechanical Engineering Science, 9: 11-23 (1967).
14. W. D. Baines and E. G. Peterson, "An Investigation of Flow Through Screens," Transactions of the ASME, 73: 467-480 (1951).
15. R. C. Pankhurst and D. W. Holder, Wind-Tunnel Technique, (Sir Isaac Pitman & Sons, LTD., London, 1952) pp. 89-94.
16. P. G. Morgan, "The Stability of Flow Through Screens," Journal of the Royal Aeronautical Society, 64: 359-362 (1960).
17. R. I. Loehrke and H. M. Nagib, "Experiments on Management of Free-Stream Turbulence, AGARD Report No. 598, AD-749-891 (1972).
18. J. L. Lumley and J. F. McMahon, "Reducing Water Tunnel Turbulence by Means of a Honeycomb," Journal of Basic Engineering, 98: 764-770 (1967).
19. R. I. Loehrke and H. M. Nagib, "Control of Free-Stream Turbulence by Means of Honeycombs: A Balance Between Suppression and Generation," Journal of Fluids Engineering, 98: 342-353 (1976).
20. E. M. Laws and J. L. Livesey, "Flow Through Screens," Annual Review of Fluid Mechanics, 10: 247-266 (1978).

1. G. B. Schubauer, W. G. Spangenberg, and P. S. Klebanoff, "Aerodynamic Characteristics of Damping Screens," National Advisory Committee for Aeronautics Technical Note 2001 (1950).
2. Hugh L. Dryden and G. B. Schubauer, "The Use of Damping Screens for the Reduction of Wind-Tunnel Turbulence," Journal of the Aeronautical Sciences, 14: 221-228 (1947).
3. G. K. Batchelor, The Theory of Homogeneous Turbulence, (Cambridge University Press, London, 1967) pp. 68-75.
4. Mahinder S. Uberoi, "Effect of Wind-Tunnel Contraction of Free-Stream Turbulence," Journal of the Aeronautical Sciences, 23: 754-764 (1956)
6. V. Ramjee and A. K. M. F. Hussain, "Influence of the Axisymmetric Contraction Ratio on Free-Stream Turbulence," Journal of Fluids Engineering, 98: 506-515 (1976).
5. Shunichi Tsuge, "Effects of Flow Contraction on Evolution of Turbulence," The Physics of Fluids, 27: 1948-1956 (1984).
7. A. K. M. F. Hussain and V. Ramjee, "Effects of The Axisymmetric Contraction Shape on Incompressible Turbulent Flow," Journal of Fluids Engineering, 98: 58-69 (1976).
3. Jimmy Tan-atichat, "Effects of Axisymmetric Contractions on Turbulence of Various Scales," Ph.D. Dissertation, Illinois Institute of Technology, Chicago (1980).
9. H. M. Nagib, A. Marion, and J. Tan-atichat, "On the Design of Contractions and Settling Chambers for Optimal Turbulence Manipulation in Wind Tunnels," AIAA Paper No. 84-0536, AIAA 22nd Aerospace Sciences Meeting, Reno, Nevada (1984).
8. E. G. Tulapurkara and V. Ramjee, "Effect of Contraction on Screen-Generated Turbulence," Aeronautical Journal, 84: 290-295 (1980).

- . T. Morel, "Comprehensive Design of Axisymmetric Wind Tunnel Contractions," Journal of Fluids Engineering, 97: 225-233 (1975) and 98: 131-133 (1976).
- . Thomas Morel, "Design of Two-Dimensional Wind Tunnel Contractions," Journal of Fluids Engineering, 99: 371-378 (1977).
- . B. S. Stratford, "The Prediction and Separation of the Turbulent Boundary Layer," Journal of Fluid Mechanics, 5: 1-16 (1959).

APPENDIX D

Flow Over a Semi-Infinite Plate with
Traveling Surface Waviness and Freestream Disturbances

by

Harold L. Rogler
United Research Corporation

URC-TR-83-021

FLOW OVER A SEMI-INFINITE PLATE WITH
TRAVELING SURFACE WAVINESS AND
FREESTREAM DISTURBANCES

by

Harold L. Rogler
Consultant
Southwest Research Institute

March 1983
United Research Corporation
428 Hill Street Suite 21
Santa Monica, California 90405
United States of America

EXPERIMENTS ON THE INFLUENCE OF ACTIVE WALLS ON THE
INITIAL AMPLITUDES AN. (U) SOUTHWEST RESEARCH INST SAN
ANTONIO TX J T PARK ET AL. MAR 85 SWRI-6984

44

N00014-82-C-0199

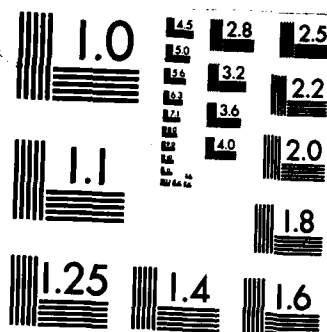
F/G 20/4

NL

END

FILED

DTIC



MICROCOPY RESOLUTION TEST CHART
NATIONAL BUREAU OF STANDARDS-1963-A

ABSTRACT

The Kelvin-Helmholtz solution for flow over a traveling wavy surface which extends to infinity upstream and downstream is extended to the case of flow over a semi-infinite wavy plate. The analytical solution is obtained by conformal mapping and integral transforms. The leading edge modifies the Kelvin solution to form a secondary flow pattern which appears to move upstream (if the surface wave moves downstream). However, this secondary flow is actually composed of a superposition of exponentially-decaying standing waves of form $v = v_0(\beta) \exp(-\beta x) \sin(\beta y) \exp(-i\omega t)$ where β and ω are real.

The surface wavinesses considered are either sinusoidal waves of form $h(x,t) = h_0 \sin[\alpha(x-ct)]$ which travel at speed c , or they are galloping waves of form $h(x,t) = [A+Bx+Ct] \cos[\alpha(x-U_0 t)]$. This wall shape induces a velocity of form $v(x,t) = v_0 \cos \alpha(x-U_0 t)$ which propagates at the freestream speed.

The solution with wavy or galloping walls is superposed on the corresponding solutions for freestream disturbances encountering a semi-infinite flat plate. The phase speed and x -wavenumber of the surface wave are matched with the phase speed and x -wavenumber of the freestream disturbance. Additionally, the phase and amplitude of the surface waviness are linked to the phase and intensity of the freestream disturbances. The freestream disturbance can propagate at any speed, c . The result of superimposing the wavy-wall solution and the freestream disturbance solution, and properly adjusting phase, wavenumber, amplitude, and propagation speed of the wavy wall is that the family of standing waves is eliminated, along with the pressure pulse at the leading edge. The traveling wave solution which remains is also modified from the flat plate case, and takes on the form of the original freestream disturbance.

The analysis is an example of using traveling wavy surfaces to modify (and in this case cancel) standing waves and the secondary flow which normally arise when freestream disturbances encounter a leading edge.

ACKNOWLEDGEMENTS

Support for this research is provided by the Office of Naval Research under Contract ONR N00014-82-C-0199 between the Office of Naval Research and Southwest Research Institute. Dr. Michael M. Reischman, ONR, is the Technical Monitor and Dr. Joel Park, SWRI, is the Principal Investigator. The author thanks Dr. Park for his comments on this manuscript.

TABLE OF CONTENTS

Abstract.....	ii
Preface.....	ii
Table of Contents.....	iii
List of Figures.....	iv
Nomenclature.....	v
1. INTRODUCTION.....	1
1.1 Introductory Comments.....	1
1.2 Objectives and organization of this analytical/numerical study..	2
2. LINEARIZED WALL BOUNDARY CONDITIONS FOR FLOW PAST WAVY AND AND GALLOPING WALLS.....	4
2.1 Sinusoidal wavy walls of form $h(x,t) = h_0 \sin[\alpha(x-ct)]$	4
2.2 Galloping surfaces of form $h(x,t) = [A+Bx+Ct]\cos[\alpha(x-U_\infty t)]$ which induce disturbances propagating at speed $c = U_\infty$	6
3. FLOW OVER A SEMI-INFINITE PLATE WITH TRAVELING WAVES.....	10
4. INTERACTION OF FREESTREAM DISTURBANCES WITH A SEMI-INFINITE FLAT PLATE.....	17
4.1 Introduction.....	17
4.2 Interaction of an oscillating vortex sheet with a semi-infinite plate.....	18
5. COMBINED EFFECT OF SURFACE WAVINESS AND FREESTREAM DISTURBANCES ON A SEMI-INFINITE PLATE.....	21
6. SUMMARY, DISCUSSION, AND CONCLUSIONS.....	22
References.....	24

LIST OF FIGURES

Figure 1. Geometry and notation for flow past a wavy or galloping semi-infinite plate.....	4
Figure 2. Galloping waves in an envelope which varies linearly in the streamwise direction. These waves induce neutral velocity disturbances which propagate at the freestream speed, $c = U_\infty$ (from Ref. 9). The amplitudes are exaggerated.....	7
Figure 3. Galloping waves in an envelope which varies linearly in time. These waves induce neutral velocity disturbances which propagate at the freestream speed (from Ref. 9).....	8
Figure 4. Galloping waves in an envelope which varies linearly in both space and time. These surface waves induce neutral velocity disturbances which propagate at the freestream speed (from Ref. 9).....	9
Figure 5. Conformal mapping of the upper half-plane onto a quarter-plane and the resultant boundary-value problem.....	11
Figure 6. Disturbance streamlines for the flow induced by a wavy or galloping surface of a semi-infinite plate for two different times (from Ref. 12 except that the phase angle of the stationary waviness is replaced by πt).....	13
Figure 7. Disturbance streamlines of the secondary flow which is superposed on the Kelvin-Helmholtz solution. This flow pattern is also one of the two effects of a semi-infinite plate on a freestream disturbance (based on Refs. 12, 16).....	15
Figure 8. Disturbance streamlines for an oscillating vortex sheet convecting downstream and alongside a semi-infinite flat plate. Three values of $\Delta\psi$ are used in this figure. Details of the flow beneath the plate and downstream of the leading edge are plotted upside down in Fig. 7 for $t = 0.5$	20

NOMENCLATURE

English

A, B, C	coefficients defined in eqns. (2.11) and (2.8)
$c = \omega/a$	phase speed
$C(z)$	Cosine Fresnel integral, $C(z) = \int_0^z \cos(\pi t^2/2) dt = C_2(\pi z^2/2)$.
$C_2(z)$	Cosine Fresnel integral(2), $C_2(z) = (2\pi)^{-1/2} \int_0^z t^{-1/2} \cos(t) dt$
$f(z)$	function related to the Fresnel integrals by $f(z) = [\frac{1}{2} - S(z)] \cos(\pi z^2/2) - [\frac{1}{2} - C(z)] \sin(\pi z^2/2)$
$F(z, t)$	function defined in Eqn. (3.5c)
$g(z)$	function related to the Fresnel integrals by $g(z) = [\frac{1}{2} - C(z)] \cos(\pi z^2/2) + [\frac{1}{2} - S(z)] \sin(\pi z^2/2)$
$h(x, t)$	displacement of the wavy or galloping wall
h_0	amplitude of the sinusoidal wall waviness
i	$(-1)^{1/2}$
$S(z)$	Sine Fresnel integral, $S(z) = \int_0^z \sin(\pi t^2/2) dt = S_2(\pi z^2/2)$
$S_2(z)$	Sine Fresnel integral(2), $S_2(z) = (2\pi)^{-1/2} \int_0^z t^{-1/2} \sin(t) dt$
t	time
u	disturbance velocity in the streamwise direction
U_∞	mean x-velocity in the freestream
v	disturbance velocity normal to the plane of the plate
$v_0^{(i)}$	characteristic disturbance velocity induced by wall motion
$v_0^{(a)}$	characteristic disturbance velocity of the freestream disturbance in the absence of the plate
x	coordinate parallel to plate and in the streamwise direction
y	coordinate normal to the plate
$z = x + iy$	complex coordinate

Greek and Script

α	x-wavenumber
β	y-wavenumber
γ	circulation/unit length of the vortex sheet (Section 4.2)
∇^2	Laplacian operator
$\lambda/2$	half-wavelength of the surface waviness
$\psi(i)$	disturbance streamfunction induced by the surface waviness
$\psi(kh)$	Kelvin-Helmholtz solution for flow past a wavy wall
$\psi(s)$	secondary streamfunction composed of a pattern of standing waves and representing the alteration to $\psi^{(kh)}$ caused by the leading edge
$\rho = \xi + i\eta$	complex coordinate
θ	phase angle of the surface waviness
$\theta(y)$	complex amplitude of the normal velocity fluctuation
ω	frequency
ξ, η	coordinates in the conformally mapped plane

Superscripts, Subscripts, and Miscellaneous Notation

a	freestream disturbance in the <u>absence</u> of the plate
f	<u>freestream</u> disturbance in the presence of the plate
i	associated with the fluctuating flow <u>induced</u> by surface waviness on a semi-infinite plate
kh	associated with the <u>Kelvin-Helmholtz</u> solution
$\text{Re}[\]$	real part of []
s	the alteration to the Kelvin-Helmholtz solution consisting of a <u>secondary</u> pattern of standing waves

1. INTRODUCTION

1.1 Introductory Comments

Wavy surfaces in engineering devices and nature do not extend to infinity upstream and downstream, of course. They have leading and trailing edges, they are bounded by non-wavy surfaces, or they connect with transition regions which smoothly flare the wavy surfaces into rigid, smooth surfaces. A general motivation for this study is to be able to predict the effects of these edges, boundaries, or transition regions.

A second motivation is associated with our awareness based on boundary-value problems by Tsugé and Rogler (Ref. 1) that at least five families of 2-D disturbances exist in a viscous, parallel-flow boundary layer along a rigid, flat wall. These families include

- (1) the discrete set of eigenmodes
- (2) exponentially-decaying standing waves
- (3) exponentially-growing standing waves
- (4) a downstream-propagating continuous spectrum
- (5) an upstream-propagating continuous spectrum

If the wall has an active wavy surface, where the wave motion can be considered to be specified and the wavenumber and phase speed do not duplicate any of those parameters of families (1) and (4), then a wave (6a) will be found in the fluid which is associated with these specified boundary conditions. However, if the wavy surface were compliant and two-way interaction could occur between the materials on either side of the interface, then this forced wave would become (6b) an eigenwave that would propagate at nearly the speed of the free wave of the surface. These are the Class B waves as categorized by Benjamin (Ref. 2). Also the fundamental eigenwave from family (1) above would be modified by such a compliant surface, and this wave forms Class A waves in Ref. 2. If two fluids are at different speeds and a shear layer forms in the interfacial region, then (8) the Kelvin-Helmholtz instability wave is a possible waveform and have been called Class C waves. These compliant or passive cases are not further considered. The wall motions considered in this report are specified, although in Section 5, those motions are linked to the freestream disturbances.

In an inviscid, uniform mean flow ($\bar{U}=1$), waves 2,3,4, and 6 remain as possible fluctuations over an active wavy wall. The versions of these waves based on the inviscid, uniform flow Rayleigh equation can be expressed in simple analytical forms. They have many properties similar to those waves found in parallel-flow, viscous boundary layers, although other important features of critical layers, sublayers, and production of unsteady vorticity inside the boundary layer are completely absent in the uniform mean flow, inviscid descriptions. These simplified versions of the waves illustrate how a wavy surface with a leading edge can initiate waves 2 and 6 along the plate. A wavy surface also can modify the traveling wave solutions associated with the freestream disturbances.

The assumptions of an inviscid, uniform mean flow have been introduced in many analytical studies in the past. Irrotational incompressible flow over a small-amplitude sinusoidal wall was analyzed by Kelvin and Helmholtz (Ref. 3).

This solution was extended by Ackeret (Ref. 4) to the linearized cases of compressible subsonic and supersonic flow. Transonic flow over a wavy wall was analyzed by Hosokawa (Ref. 5) who included the nonlinear transonic term in his analysis. He assumed that the flow was isentropic and periodic. Moore and Gibson (Ref. 6) and Vincenti (Ref. 7) analyzed inviscid compressible flow over a sinusoidal wall of a gas in vibrational or chemical non-equilibrium.

Horlock (Ref. 8) analyzed flow in an unsteady wind tunnel with small-amplitude sinusoidal wavy walls with various phase relationships between the two wavy walls. Rogler (Ref. 9) analyzed the small-amplitude cases of wall amplitudes varying as $h(x,t) = h_0 \exp[i\alpha(x-ct)]$ with α complex and $c \neq U_\infty$ and $h(x,t) = (h_0 + h_1 x + h_2 t) \exp[i\alpha(x - U_\infty t)]$. The latter wall shape is a surface wave which induces neutral disturbances that propagate at the freestream speed, $c = U_\infty$. Large-amplitude traveling wavy walls in a channel were studied in Ref. 9 also. The nonperiodic flow induced by small-amplitude traveling sinusoidal walls in a corner was analyzed by Rogler (Ref. 10).

The assumptions of an inviscid, uniform mean flow have also been usefully introduced in steady and unsteady linearized airfoil theory, and the propagation and dampening of sound in ducts. The uniform flow analyses by Benjamin (Ref. 2) and Landahl (Ref. 11) were used to study several basic waves in flows near compliant surfaces.

A companion study by Rogler (Ref. 12) considers flow over a semi-infinite plate with stationary waviness. References associated with eight other approaches which have been used to study flows over wavy walls are outlined in that report.

1.2 Objectives and organization of this analytical/numerical study

The objectives of this analytical/numerical study are to

- (a) Extend the previous analysis of flow over a semi-infinite stationary wavy wall (Ref. 12) to the case of a semi-infinite traveling wavy wall. This analysis also represents an extension of the Kelvin-Helmholtz solution for flow over a doubly-infinite wavy wall ($-\infty < x < \infty$) to the semi-infinite wavy plate ($0 < x < \infty$) with a leading edge at $x=0$.
- (b) Summarize and extend several classes of linearized boundary conditions of an inviscid, uniform mean flow past sinusoidal walls with wall shapes of form $h(x,t) = h_0 \sin[\alpha(x-ct)]$, and flow past "galloping" walls with wall shapes of the form $h(x,t) = [A+Bx+Ct] \cos[\alpha(x-U_\infty t)]$.
- (c) Summarize and extend the solutions for freestream disturbances encountering a semi-infinite plate.
- (d) Combine the following two solutions into a single theory
 - the solution for flow with a semi-infinite wavy wall

• the solution for freestream disturbances encountering a semi-infinite plate

The phase speeds and x-wavenumbers of the two cases are the same, and the amplitudes and phases are adjusted so that the dipole-like pressure pulse at the leading edge is eliminated.

The analysis serves as an example of a theory which combines the effects of freestream disturbances and surface waviness into a single analysis. The purpose of the traveling surface wave is to modify or eliminate some of the precursors of the Tollmien-Schlichting stability waves. Rather than setting up eigenvalue problems which consider the effects of waviness on stability waves, this analysis considers the effect of waviness on two other families of solutions: (1) the exponentially-varying standing waves (represented here as the counterpart described by the Rayleigh equation for a uniform mean flow) and (2) the downstream-traveling continuous spectrum. No stability waves appear in this problem with a uniform mean flow.

The plan of this report is that linearized wall boundary conditions for wavy walls and galloping walls are outlined in Section 2. The solution for flow past semi-infinite plates with wavy and galloping surfaces is presented in Section 3. The solution for flow past a semi-infinite flat plate, with disturbances in the freestream (including arrays of vortices and irrotational fluctuations) is summarized in Section 4. The case of an oscillating vortex sheet convecting downstream past the leading edge is also analyzed in Section 4. The combined case of a wavy surface and freestream disturbances is analyzed in Section 5 by superimposing the solutions from Sections 3 and 4. The results are discussed in Section 6.

2. LINEARIZED WALL BOUNDARY CONDITIONS FOR FLOW PAST WAVY AND GALLOPING WALLS

In the first part of this section, a direct analysis will be used to recover the usual linearized boundary condition for an irrotational flow past a small-amplitude sinusoidal wall. In the second part, the case of disturbances traveling at the freestream speed, $c=U_\infty$, is analyzed by an indirect method. The more generalized wall shapes which result are called "galloping".

2.1 Sinusoidal wavy walls of form $h(x,t) = h_0 \sin[\alpha(x-ct)]$

The geometry and notation for the semi-infinite plate with a wavy surface is shown in Figure 1. The displacement of the wall is the traveling sine wave

$$h(x,t) = h_0 \sin[\alpha(x-ct)] \quad (2.1)$$

where h_0 is the amplitude of the surface waviness, x is the coordinate in the streamwise direction, α is the x -wavenumber, c is the phase speed, and t is time. The relation between the surface displacement h and the normal velocity $v^{(i)}$ along the x -axis induced by that wall displacement and motion can be expressed by the linearized relation

$$v^{(i)}(x,y=0,t) = \partial h / \partial t + U_\infty \partial h / \partial x = \psi_x^{(i)} \quad (2.2a)$$

For the wall motion given by eqn.(2.1), this velocity is

$$v^{(i)}(x,0,t) = v_0^{(i)} \cos[\alpha(x-ct)] \quad (\text{for } x > 0) \quad (2.2b)$$

where the velocity amplitude and wavy wall amplitude are related by

$$v_0^{(i)} = \alpha h_0 (U_\infty - c) \quad (2.3a)$$

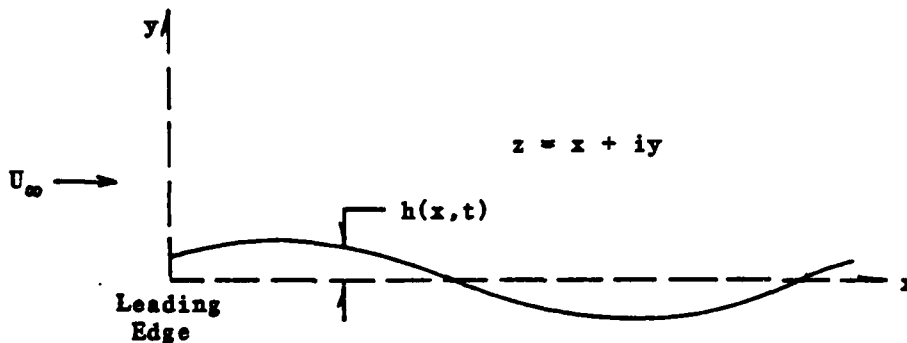


Figure 1. Geometry and notation for flow past a wavy or galloping semi-infinite plate.

terms of the streamfunction, this boundary condition is

$$\psi^{(i)}(x \geq 0, 0) = h_0(U_\infty - c) \sin[\alpha(x - ct)] + \text{function}(t) \quad (2.3b)$$

is boundary condition along the x-axis downstream of the leading edge will be used in Sections 3 and 4 for sinusoidal waves which propagate at speed c.

Although the boundary conditions (2.3a,b) are valid for $c = U_\infty$, sinusoidal surface waves in a uniform mean flow which propagate at the freestream speed do not induce any flowfield, $v^{(i)} = 0$. More generalized wall shapes which induce disturbances that propagate at speed $c = U_\infty$ are considered in the following paragraphs.

2 Galloping surfaces of form $h(x, t) = [A + Bx + Ct] \cos[\alpha(x - U_\infty t)]$ which induce disturbances propagating at speed $c = U_\infty$

Some surface wave of unknown geometry, $h(x, t)$, will be assumed to induce a velocity along the x-axis

$$v^{(i)} = v_0^{(i)} \cos[\alpha(x - U_\infty t)] \quad (2.4)$$

Used on the linearized relation (2.2a) between displacement and velocity, the equation

$$\partial h / \partial t + U_\infty \partial h / \partial x = v_0 \cos[\alpha(x - U_\infty t)] \quad (2.5)$$

is a forced equation which will admit both homogeneous and particular solutions. Only the particular solution was considered in Section 2.1.

The homogeneous solution is

$$h^{(H)}(x, t) = F(x - U_\infty t) \quad (2.6)$$

where F is any continuous function with a continuous first derivative with sufficiently small amplitude and slope such that the linearized relation (2.5) is valid. This wall shape propagates to the right at speed U_∞ without changing shape. It does not induce any disturbances. This geometry can be further analyzed and represented as a series or integral of waves of forms

$$\cos[\gamma(x - U_\infty t)] \text{ and } \sin[\gamma(x - U_\infty t)] \quad (2.7)$$

where γ is the x-wavenumber. Alternately, these are two examples of the homogeneous solutions.

By the method of undetermined coefficients, the particular integral could be assumed to be the same form as the forcing function and its derivative

$$A \cos[\alpha(x - U_\infty t)] + D \sin[\alpha(x - U_\infty t)]$$

However, these solution forms duplicate those of the homogeneous solution (2.7) when Fourier analyzed and $\gamma = \alpha$, and must be multiplied by powers of x and t. The trial solution for the particular integral is therefore

$$h(P) = [Bx+Ct]\cos[\alpha(x-U_{\infty}t)] + [Ex+Ft]\sin[\alpha(x-U_{\infty}t)] \quad (2.8)$$

By substituting eqn.(2.8) into eqn.(2.5), then the constants

$$E = F = 0 \quad (2.9a)$$

and the two remaining constants are related to the amplitude $v_0^{(i)}$ by the relation

$$U_{\infty}B + C = v_0^{(i)} \quad (2.9b)$$

in agreement with eqn.(9.11) of Ref. 9. For a given velocity $v_0^{(i)}$, either constant B or C can be specified and the other constant found. B or C can be zero.

The complete solution is the sum of the homogeneous solution (2.6) and the particular integral (2.8,2.9a,b)

$$h(x,t) = F(x-U_{\infty}t) + [Bx+Ct]\cos[\alpha(x-U_{\infty}t)] \quad (2.10)$$

The homogeneous solution can be rewritten as

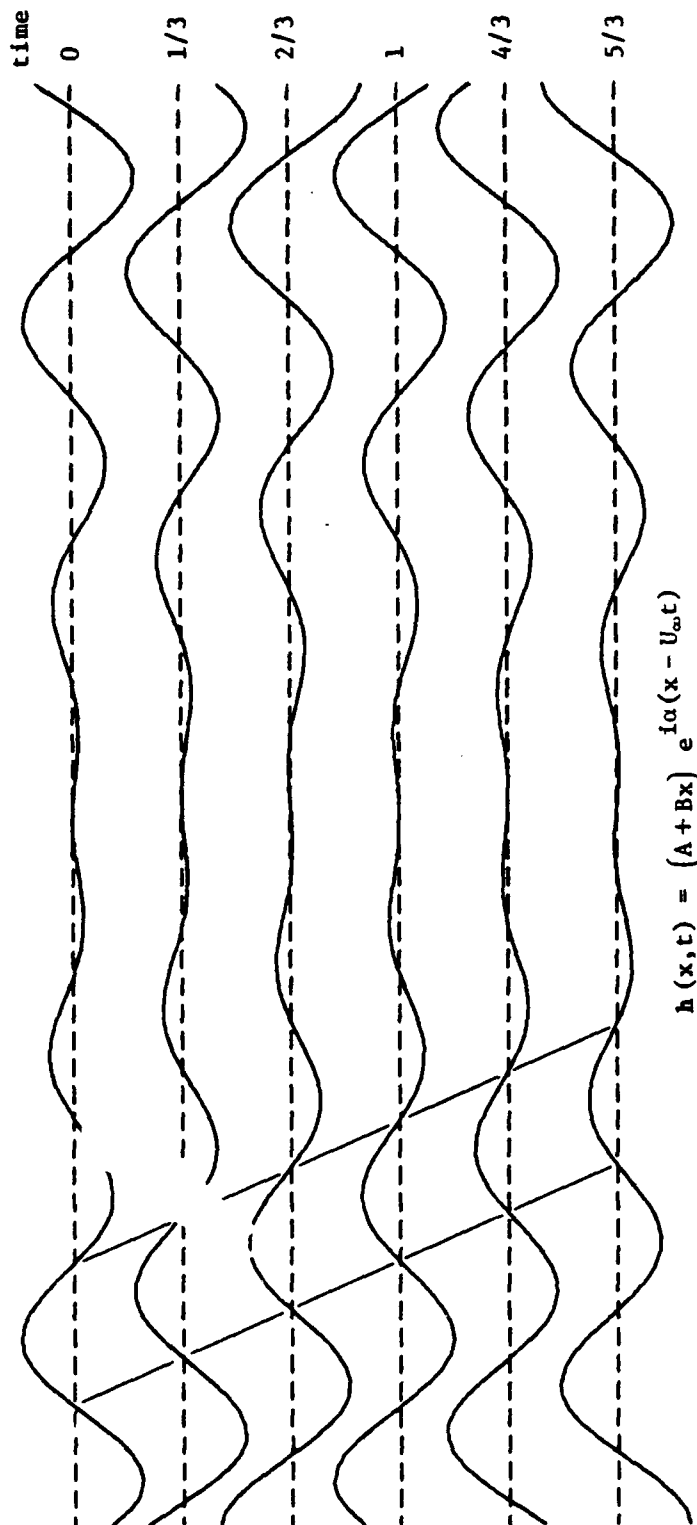
$$F(x-U_{\infty}t) = G(x-U_{\infty}t) + A\cos[\alpha(x-U_{\infty}t)] \quad (2.11)$$

where A is the appropriate Fourier coefficient; the function $G(x-U_{\infty}t)$ is what remains from the homogeneous solution after the wave $A\cos\alpha(x-U_{\infty}t)$ is subtracted from F. In this rearranged form, the complete solution is

$$h(x,t) = G(x-U_{\infty}t) + [A+Bx+Ct]\cos[\alpha(x-U_{\infty}t)] \quad (2.12)$$

The role of the constant A, which is part of the homogeneous solution, is to provide control over the initial amplitudes of the surface waves.

Neglecting the function G, several cases of solution (2.12) are possible. They include the case $C=0$, which represents waves decaying or growing in a linear envelope in space, and $B=0$ which represents waves decaying or growing in time, also in a linear fashion. The general case has both B and C nonzero. The surface geometries for these galloping cases are plotted in Figures 2-4 from Ref. 9. These figures help illustrate the role of the constant A. Only for some interval of x (if $C=0$) or only for some interval of time (if $B=0$) will the amplitudes be sufficiently small such that the linearized boundary condition is applicable. The constant A controls that interval.



$$h(x,t) = (A+Bx) e^{i\alpha(x-U_\infty t)}$$

Figure 2. Galloping waves in an envelope which varies linearly in the streamwise direction. These waves induce neutral velocity disturbances which propagate at the freestream speed, $c = U_\infty$ (from Ref. 9). The amplitudes are exaggerated.

5. COMBINED EFFECT OF SURFACE WAVINESS AND FREESTREAM DISTURBANCES ON A SEMI-INFINITE PLATE

The linear solutions presented earlier can be superposed. The cases of surface waviness and the freestream disturbances both have the dimensionless x of the normal velocity

$$v(x,0,t) = \cos[\pi(x-t)]$$

both have the same phase. The dimensional x -wavenumber and the dimensional phase speed also are required to be the same for the two cases. Also, the characteristic amplitudes, $v_0^{(a)}$ and $v_0^{(i)}$ must be the same for the cases so that the characteristic value of the streamfunctions are the same. Dimensionally, this requires that

$$v_0^{(i)} = \alpha h_0 (U_\infty - c) = v_0^{(a)} \quad (5.1)$$

in eqn. (2.3a) if the wall is sinusoidal and $c \neq U_\infty$, and

$$v_0^{(i)} = U_\infty B + C = v_0^{(a)} \quad (5.2)$$

in eqn. (2.9b) if the freestream disturbance propagates at dimensional speed $= U_\infty$. The constants B and C are described in Section 2.2; they control the slopes of the galloping wall.

If the above conditions are satisfied, then the streamfunction for the combined effect of freestream disturbances and a wavy or galloping surface is

$$\begin{aligned} \psi^{(\text{combined})} &= \psi^{(f)} + \psi^{(i)} \\ &= [\psi^{(a)} - \psi^{(i)}] + \psi^{(i)} \end{aligned}$$

$\psi^{(\text{combined})} = \psi^{(a)}$

(5.3)

With this strategy of introducing a wavy wall or a galloping wall when freestream disturbances are present, no adjustment is necessary for the freestream disturbance to satisfy impermeability at the surface of the plate.

This result can also be found directly by consideration of the boundary-value problem, without necessity to find the solution (3.3). However, in any practical device, the conditions on phase, x -wavenumber, phase speed, and amplitude cannot be exactly satisfied. Calculations with matches are possible by using the theories presented.

In summary, if the phase, x -wavenumber, phase speed, and amplitude of the surface waviness are adjusted as indicated relative to the freestream disturbance, and if the other conditions for the theories for the effects of surface waviness and freestream disturbances are valid, then the freestream disturbance will propagate past the plate as if the plate were removed from the flowfield. The important result is that the dipole-like pressure pulse at the leading edge is eliminated. The theories provide the tools useful to determine the effects of not exactly satisfying the necessary conditions.

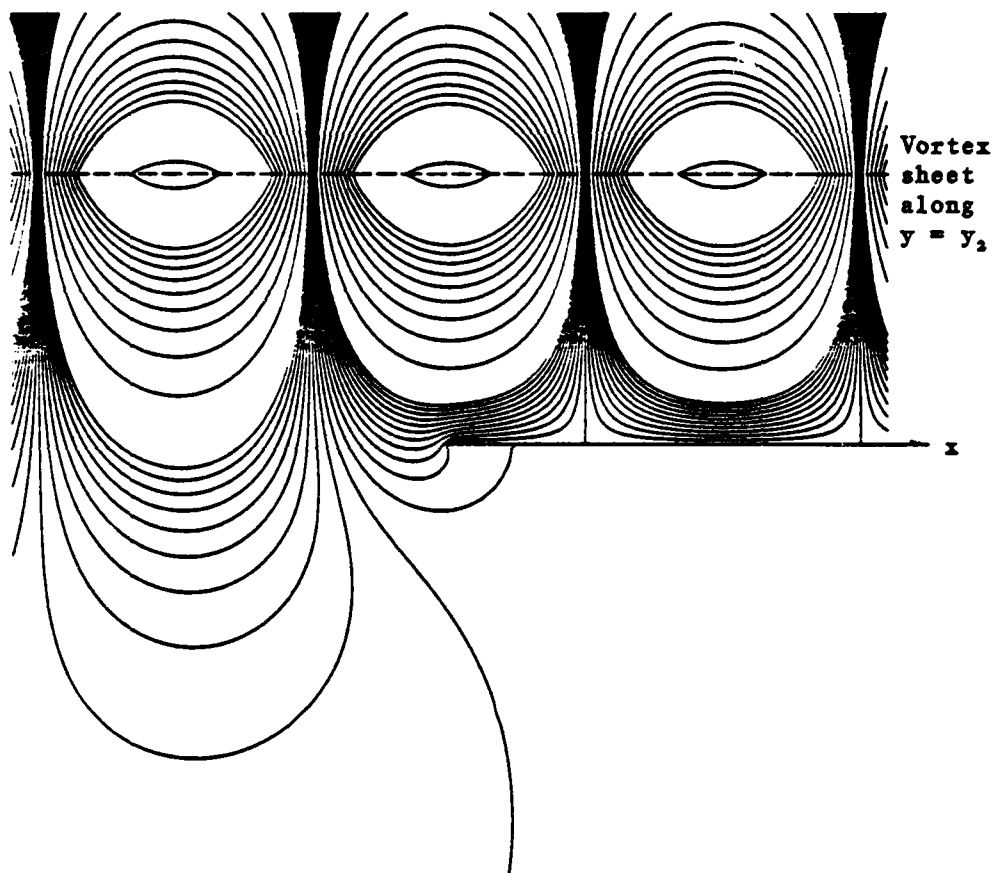


Figure 8. Disturbance streamlines for an oscillating vortex sheet convecting downstream and alongside a semi-infinite flat plate. Three values of $\Delta\psi$ are used in this figure. Details of the flow beneath the plate and downstream of the leading edge are plotted upside down in Fig. 7 for $t = 0.5$.

As noted in eqn.(4.2), the streamfunction for this vortex sheet interacting with a semi-infinite plate is given by $\varphi(f) = \varphi(a) - \varphi(i)$, where $a)$ is given by eqns.(4.4b,4.5b). The resultant streamline pattern is plotted in Figure 8.

In the next section, the cases of the flow induced by surface waviness and the flow associated with freestream disturbances interacting with a semi-infinite plate are superposed.

- Stationary surface waviness (Ref. 12)
- Traveling surface waviness (Sections 2,3 of this report)
- Combination of traveling surface waviness and freestream disturbances (Section 5 of this report)
- Quiescent freestream with a flat plate ($v_0^{(a)} = v_0^{(i)} = 0$).

4.2 Interaction of an oscillating vortex sheet with a semi-infinite plate

As an example of the procedure summarized above, the problem of an oscillating vortex sheet lying along the line $y = y_2$ will be analyzed. This sheet convects downstream at speed U_∞ past the leading edge of the semi-infinite plate.

In order to define the characteristic velocity induced by the vortex sheet, the equations of this section are in dimensional form. If a vortex sheet of strength γ per unit length

$$\gamma(x,t) = \gamma_0 \sin[\alpha(x-t)] \quad (4.3)$$

convects along the line $y = y_2$, then the streamfunction induced by that vortex sheet is

$$\psi^{(a)} = C_1 e^{-\alpha y_2} \sin[\alpha(x-t)] \quad (\text{for } y \geq y_2) \quad (4.4a)$$

$$\psi^{(a)} = C_2 e^{+\alpha y_2} \sin[\alpha(x-t)] \quad (\text{for } y \leq y_2) \quad (4.4b)$$

where C_1 and C_2 are constants which will be linked to the amplitude of the vortex sheet, γ_0 .

Since $\psi^{(a)}$ must be continuous across the sheet, then

$$C_1 \exp(-\alpha y_2) \sin[\alpha(x-t)] = C_2 \exp(\alpha y_2) \sin[\alpha(x-t)]$$

$$\text{or} \quad C_1 = C_2 \exp(2\alpha y_2) \quad (4.5a)$$

Across the vortex sheet, the jump condition must be satisfied

$$\left[-\frac{\psi^{(a)}}{y} \right]_{y_2+} - \left[-\frac{\psi^{(a)}}{y} \right]_{y_2-} = \gamma$$

$$\text{or} \quad C_2 = \gamma_0 \exp(-\alpha y_2) \quad (4.5b)$$

If the vortex sheet lies above the plate, then $y_2 > 0$, and the normal velocity along the x-axis is

$$v^{(a)} = C_2 \alpha \cos[\alpha(x-t)]$$

or the characteristic velocity is

$$v_0^{(a)} = \alpha \gamma_0 \exp(-\alpha y_2) \quad (4.6)$$

This amplitude is required in the nondimensionalization, as noted in the sentence following eqn.(4.2).

4. INTERACTION OF FREESTREAM DISTURBANCES WITH A SEMI-INFINITE FLAT PLATE

4.1 Introduction

This section summarizes the analyses of the inviscid interaction of 2-D freestream disturbances with a semi-infinite flat plate. The disturbances can have rotational and/or irrotational regions. Different disturbances propagate downstream, upstream, or are stationary in time. A number of studies have been carried out which are listed below:

- Array of square vortices convecting downstream (Ref. 14)
- Array of rectangular vortices convecting downstream (Ref. 15)
- Oblique and longitudinal plane waves of vorticity convecting downstream (Ref. 15)
- Oscillating vortex sheet convecting downstream (Section 4.2 of this report)
- One-sided irrotational wave propagating at speed c (Ref. 15)
- Double-sided irrotational waves with oblique or normal velocities along the x -axis and propagating at speed c (Ref. 15)
- Double-sided irrotational wave which produces only longitudinal velocities along the x -axis (Ref. 15, Note that $v^{(a)}(x,0,t)=0$)
- Row of potential vortices (Ref. 15)
- Karman vortex street propagating at speed c downstream (Unpublished)
- Half-plane of rectangular vortices convecting downstream (Unpublished)

With the exception of the row of potential vortices and the Karman street, the above disturbances have the velocity

$$v^{(a)}(x,0,t) = v_0^{(a)} \cos[\alpha(x-ct)] \quad (\text{along the } x\text{-axis}) \quad (4.1)$$

The superscript (a) emphasizes that this is the velocity of the freestream disturbance in the absence of the plate, i.e. if the plate were removed from the flowfield. What is the flowfield with the plate present?

Under conditions discussed in Refs. 14,15, if $\psi^{(a)}$ is the streamfunction with the plate absent, then the streamfunction with the plate present is

$$\psi(f) = \psi^{(a)} - \psi(i) \quad (4.2)$$

where $\psi(i)$ is the streamfunction given in eqn. (3.3). The nondimensionalizations are the same as before, except that the characteristic velocity is the amplitude of the normal velocity along the x -axis of the disturbance in the absence of the plate, $v_0^{(a)}$, as noted in eqn. (4.1).

The Karman street and the row of potential vortices traveling downstream have velocities which, in the absence of the plate, are periodic in x , but they are not sinusoidal. The interactions of these disturbances with a semi-infinite plate have been expressed as Fourier series.

Hence, the streamfunction $\psi^{(a)}$ plays a role in the interaction of a variety of freestream disturbances with a plate, as well as the flowfield induced by wavy and galloping surfaces. To the above list, the following cases can be added

$$v^{(s)}(x>0, y, t) = v_0^{(s)}(\beta) \sin \beta y \exp(-\beta x - i \omega t) \quad (3.8)$$

where β is a real wavenumber. Each of these waves satisfies impermeability, each decays exponentially in the streamwise direction, and each oscillates sinusoidally in time. A difference between the waveform (3.8) above and the results of Ref. 12 is that the above flow is unsteady, while Ref. 12 is steady.

An analogous result for freestream disturbances encountering a plate was presented in Ref. 16. An effect of the leading edge was to excite a spectrum of standing waves, and also modify the traveling wave solution for the freestream disturbance.

In conclusion of this section, the streamfunction and velocities of the flow induced by a semi-infinite wavy or galloping wall have been found which illustrate the flow around the leading edge and other upstream influences. Downstream of the leading edge, the flow is represented in terms of the classical Kelvin-Helmholtz solution and a secondary flow. This unsteady, irrotational, secondary flow satisfies the impermeability condition on a flat plate, and can be represented as a superposition of exponentially-decaying standing waves.

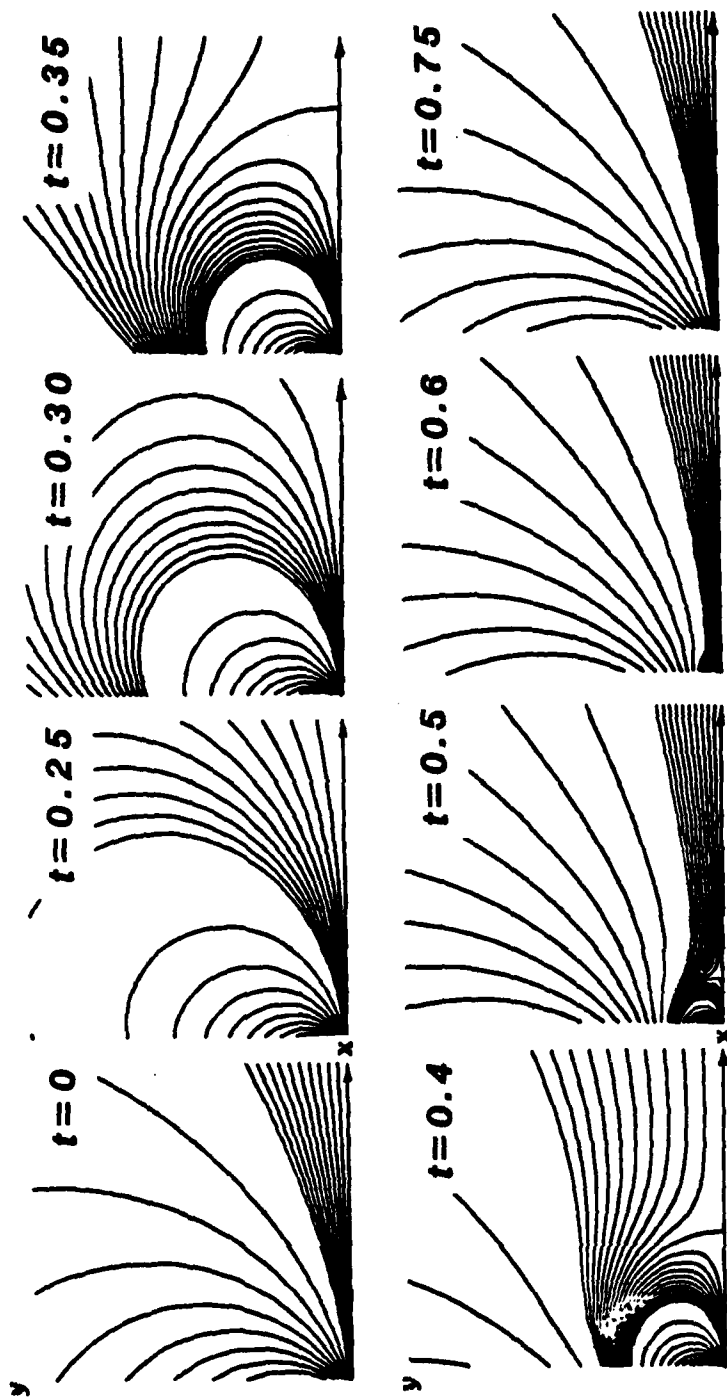


Figure 7. Disturbance streamlines of the secondary flow which is superposed on the Kelvin-Helmholtz solution. This flow pattern is also one of the two effects of a semi-infinite plate on a freestream disturbance (based on Refs. 12,16)

$$f(z) = [\frac{1}{2} - S(z)]\cos(\pi z^2/2) - [\frac{1}{2} - C(z)]\sin(\pi z^2/2)$$

$$g(z) = [\frac{1}{2} - C(z)]\cos(\pi z^2/2) + [\frac{1}{2} - S(z)]\sin(\pi z^2/2)$$

$$S(z) = S_2(\pi z^2/2); C(z) = C_2(\pi z^2/2)$$

The asymptotic series for f and g (Ref. 12, page 302) are

$$\pi z f(z) \sim 1 + \sum_{m=1}^{\infty} (-1)^m [1.3 \dots (4m-1) / (\pi z^2)^{2m}]$$

$$\pi z g(z) \sim \sum_{m=0}^{\infty} (-1)^m [1.3 \dots (4m+1) / (\pi z^2)^{2m+1}]$$

These series converge rapidly. The solution form (3.5d) avoids the problems of finding the small differences between large numbers. While the direct evaluation of solution (3.5b) was limited to about $|z|=1.8$ when 32 bit arithmetic was used, and was limited to about $|z|=5.2$ when 64 bit arithmetic was used, solution (3.5d) has been evaluated at $|z|=400$, which is 200 wavelengths from the leading edge.

A singularity occurs at the leading edge for the velocities, with the validity of the theory consistent with linearized airfoil theory. The region where the velocities are large can be made as small as desired by making the amplitude of the wall waviness smaller. Hence, this is the proper first-order solution as long as the flow is unseparated at the leading edge. Since the practical case of flows past bodies with streamlined leading edges is of interest, the assumption of unseparated flow implicitly contained in Laplace's equation appropriately models that feature without unduly complicating the analysis with details of the nose geometry and plate thickness.

Solution (3.3) with streamlines plotted in Figs. 6a,b is valid both upstream and downstream of the leading edge. As noted in Ref. 12, the leading edge modifies the Kelvin-Helmholtz solution, denoted by $\psi^{(kh)}$. Hence, the Kelvin-Helmholtz solution is subtracted from $\psi^{(i)}$, and the result is a streamfunction for a secondary flow

$$\psi^{(s)} = \psi^{(i)} - \psi^{(kh)} \quad (\text{for } x > 0) \quad (3.6)$$

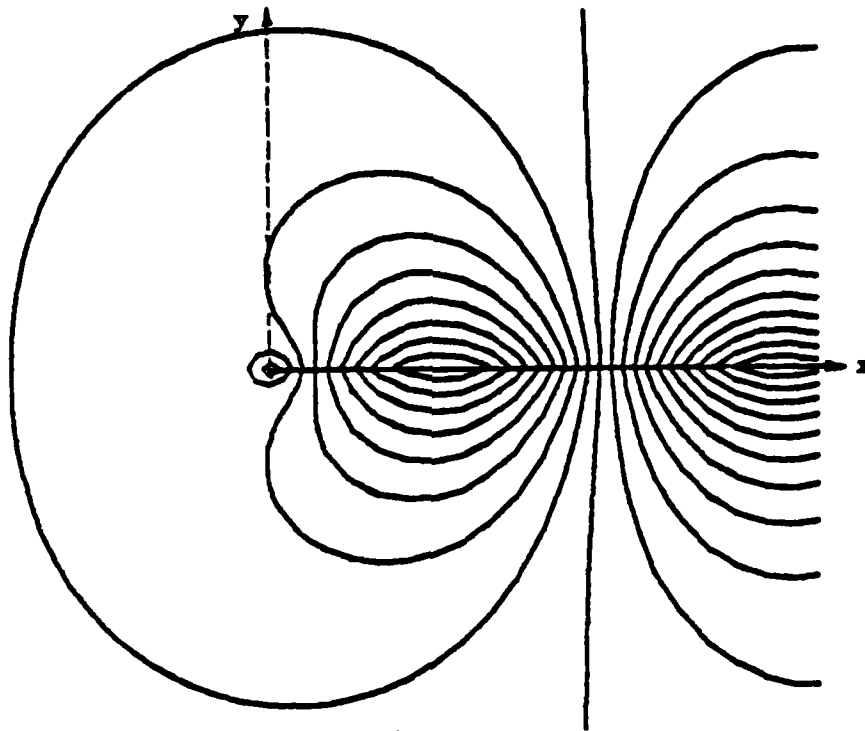
The streamlines of this secondary flow are shown in Fig. 7. Since both $\psi^{(i)}$ and $\psi^{(kh)}$ are irrotational, then $\psi^{(s)}$ is also irrotational. Since both $\psi^{(i)}$ and $\psi^{(kh)}$ have the same wall boundary conditions, then

$$\psi^{(s)}(x > 0, y=0, t) = 0 \quad (3.7)$$

This result denotes that this secondary flow satisfies the impermeability condition along a flat plate. However, it has indirectly been excited by the combined effects of the wavy wall and the leading edge.

Based on the mathematical developments of Ref. 12, the secondary flow can be represented as a superposition of exponentially-decaying standing waves of the form

(a) $t = 0$



(b) $t = 1/2$

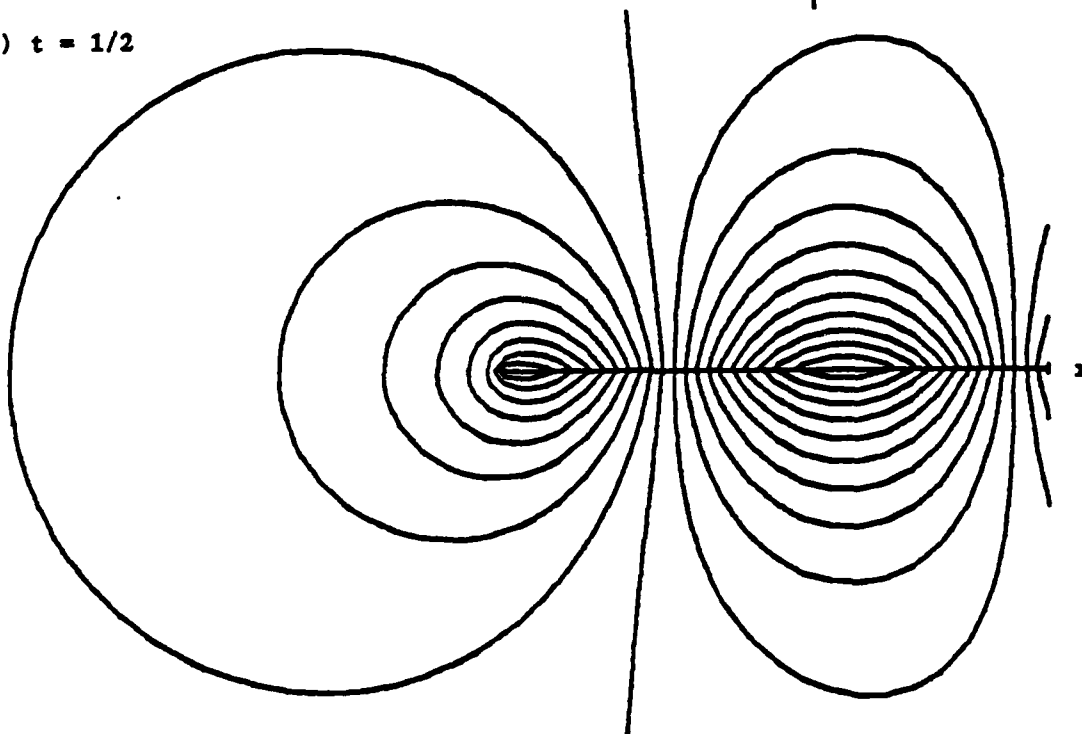


Figure 6. Disturbance streamlines for the flow induced by a wavy or galloping surface of a semi-infinite plate for two different times (From Ref. 12 except that the phase angle of the stationary waviness is replaced by πt).

problem arose associated with the interaction of freestream disturbances with a semi-infinite flat plate.

The solution for the streamfunction of the flow induced by the semi-infinite plate with a sinusoidal wall is

$$\begin{aligned} \psi^{(i)} = & \{ \cos \pi t \operatorname{Re} [-\cos \pi z S_2(-\pi z) - \sin \pi z C_2(-\pi z) \\ & + \cos \pi z C_2(-\pi z) - \sin \pi z S_2(-\pi z) + \sin \pi z] \\ & - \sin \pi t \operatorname{Re} [-\cos \pi z S_2(-\pi z) - \sin \pi z C_2(-\pi z) \\ & - \cos \pi z C_2(-\pi z) + \sin \pi z S_2(-\pi z) + \cos \pi z] \} / \pi \end{aligned} \quad (3.3)$$

where S_2 and C_2 are the Fresnel integrals

$$S_2 = (2\pi)^{-1/2} \int_0^z t^{-1/2} \sin(t) dt \quad (3.4a)$$

$$C_2 = (2\pi)^{-1/2} \int_0^z t^{-1/2} \cos(t) dt \quad (3.4b)$$

The Fresnel integrals are evaluated numerically, either as asymptotic series valid for large argument or series expansions valid for small argument (Ref. 13). The details of the evaluations are given in Ref. 12.

Figures 6a,b show the disturbance streamline patterns for the flow induced by the semi-infinite wavy wall at two times a quarter period apart. These figures, and the others, do not include the uniform mean flow. The induced flow depends on the time. In all cases, the wavy surfaces on opposite sides of the plate are in phase. The upstream influence of the waviness can be clearly seen, as expected since Laplace's equation is elliptic.

The velocities corresponding to solution (3.3) are

$$u^{(i)} = -\psi_y^{(i)} = -iF(z,t) \quad (3.5a)$$

$$v^{(i)} = \psi_x^{(i)} = F(z,t) \quad (3.5b)$$

where F is the complex function

$$\begin{aligned} F = & \sin(\pi z - \pi t) [S_2(-\pi z) - C_2(-\pi z)] \\ & - \cos(\pi z - \pi t) [S_2(-\pi z) + C_2(-\pi z) - 1] - (\sin \pi t + \cos \pi t) / [\pi(-2z)^{1/2}] \end{aligned} \quad (3.5c)$$

For large $|z|$, computational experience has shown that it is better to recast the solution as

$$F = \sin \pi t \{ f - g - 1/[\pi(-2z)^{1/2}] \} + \cos \pi t \{ f + g - 1/[\pi(-2z)^{1/2}] \} \quad (3.5d)$$

where $f(z)$ and $g(z)$ are related to the Fresnel integrals by

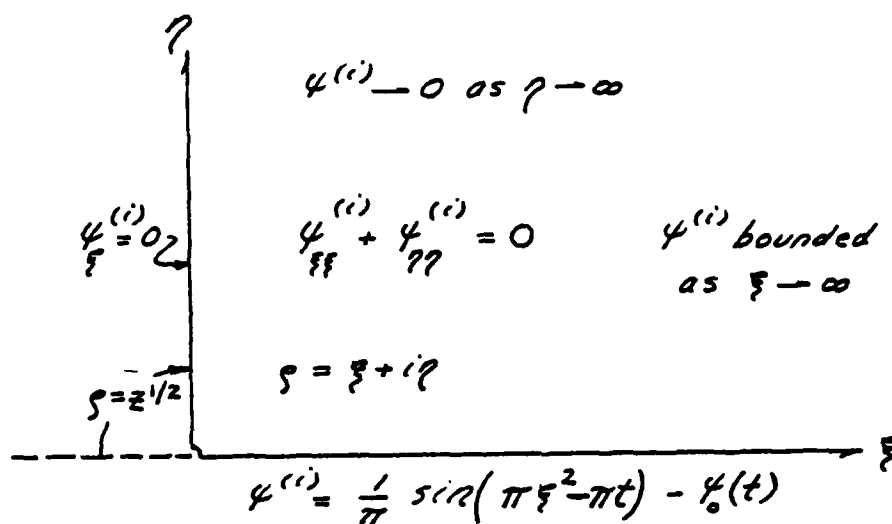


Figure 5. Conformal mapping of the upper half-plane onto a quarter-plane and the resultant boundary-value problem.

3. FLOW OVER A SEMI-INFINITE PLATE WITH TRAVELING WAVES

The analysis of this section is closely related to the analysis by Rogler (Ref. 12) for flow over a stationary wavy wall, except in the present case, the surface wave travels (downstream or upstream) at speed c . The case of galloping walls is also included.

By conformal mapping and integral transforms, the flowfield with traveling surface waviness or galloping on a semi-infinite plate will be analyzed. A solution is sought which satisfies Laplace's equation, $\nabla^2 \psi^{(i)} = 0$, where $\psi^{(i)}$ is the streamfunction for the flow induced by the surface waviness. For sign convention, the streamfunction is related to the longitudinal and normal velocities by $-\psi_y^{(i)} = u^{(i)}$ and $\psi_x^{(i)} = v^{(i)}$ respectively.

The streamfunction along the x -axis downstream of the leading edge is

$$\psi^{(i)}(x, 0, t) = (v_0^{(i)}/a) \cos[a(x-ct)] \quad (\text{for } x > 0) \quad (3.1)$$

When written in this form, the theory is applicable for the two cases described in the previous section: (1) $v_0^{(i)} = ah_0(U_\infty - c)$ for wavy walls of sinusoidal form, and (2) $v_0^{(i)} = U_\infty B + C$ for galloping walls which induce disturbances traveling at the freestream speed.

Hereafter, the streamfunction is nondimensionalized against $v_0^{(i)}\pi/a$ and the velocities are nondimensionalized against $v_0^{(i)}$. The x and y coordinates are nondimensionalized against the half-wavelength $\lambda/2 = \pi/a$ of the sinusoidal disturbance. For historical reasons, the time is nondimensionalized against the characteristic time π/ac , which is the time for a fluid particle traveling at speed c to travel a half-wavelength, $\lambda/2 = \pi/a$. Under these nondimensionalizations, the amplitude of the streamfunction is $1/\pi$, and the amplitude of the normal velocity along the plate is unity.

For the case of the waviness being in-phase on the opposite sides of the plate, the streamfunction will be symmetric about the x -axis and the homogeneous Neumann boundary condition is applicable upstream of the plate

$$\psi_y^{(i)} = 0 \quad (\text{for } y=0, x < 0) \quad (3.2)$$

The solution is assumed to vanish far-away from the plate, both far-upstream and at large distances laterally from the plate. Far-downstream of the leading edge, the solution is bounded. It will be shown that the classical Kelvin-Helmholtz solution is recovered. These exterior boundary conditions, along with the Dirichlet and Neumann conditions along the x -axis and Laplace's equation yield a well-posed elliptic mathematical system.

The half-plane above the x -axis is conformally mapped onto the quarter-plane as shown in Figure 5 by the mapping, $\rho = z^{1/2}$, where $z = x+iy$ and $\rho = \xi+i\eta$. The conformal mapping alleviates the problem of split boundary conditions along the x -axis, with a Neumann boundary condition for $x < 0$ (eqn. 3.2) and a Dirichlet boundary condition for $x > 0$ (eqn. 3.1). Under this mapping, the resultant mathematical system is defined in Figure 2. The solution is obtained by a cosine integral transform in the ξ direction. The details are presented in Ref. 14, where a closely related boundary-value

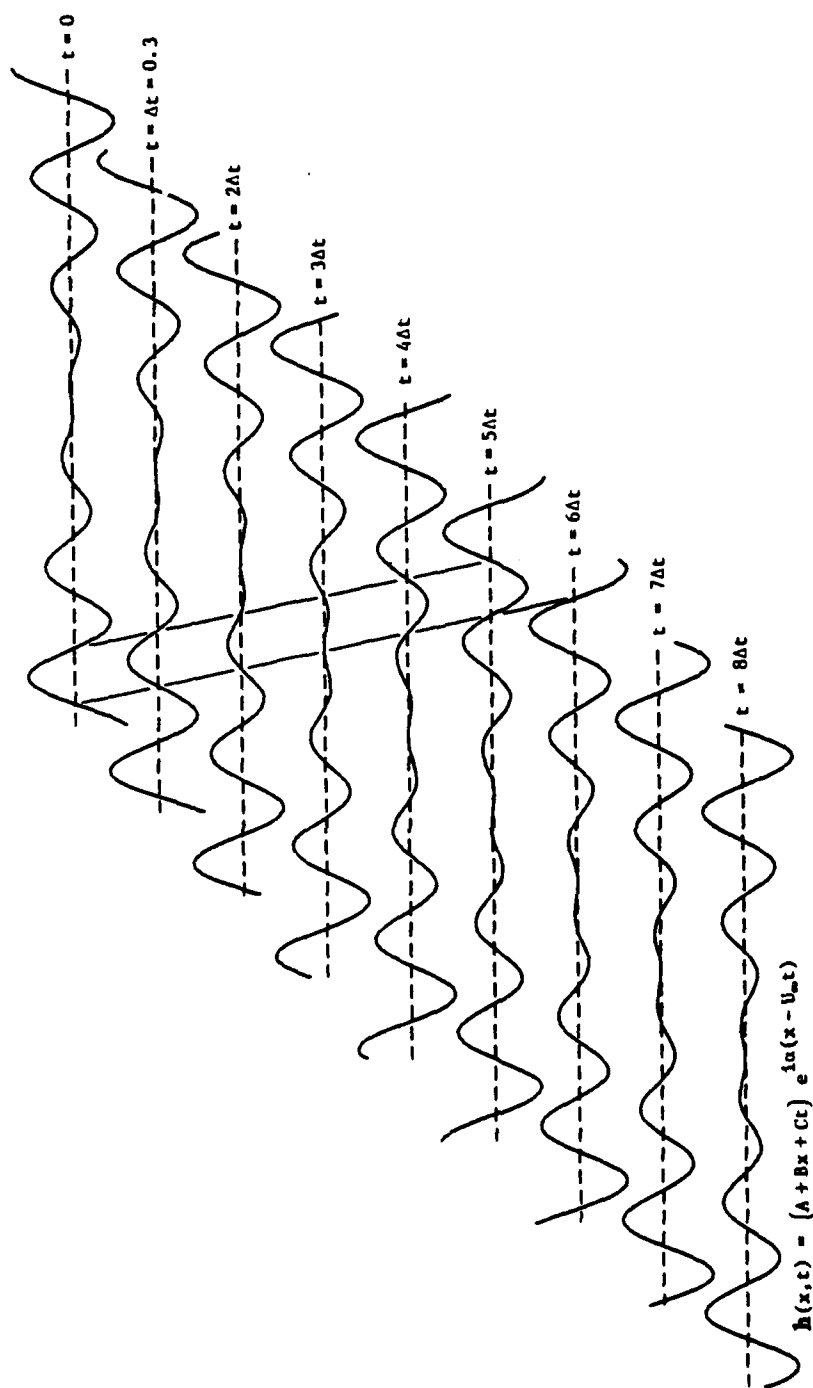


Figure 4. Galloping waves in an envelope which varies linearly in both space and time. These surface waves induce neutral velocity disturbances which propagate at the freestream speed (from Ref. 9).

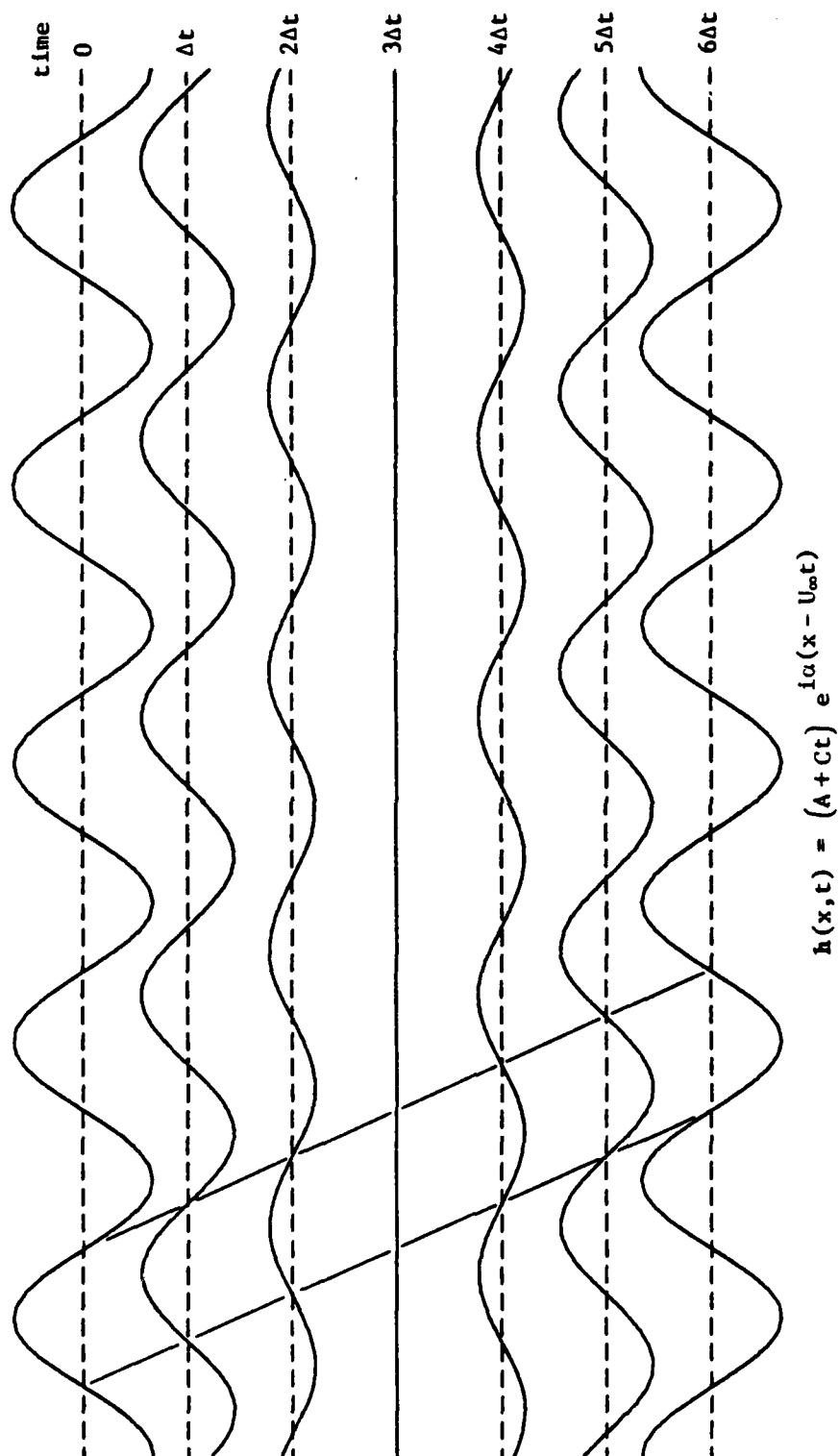


Figure 3. Galloping waves in an envelope which varies linearly in time. These waves induce neutral velocity disturbances which propagate at the freestream speed (from Ref. 9).

6. SUMMARY, DISCUSSION, AND CONCLUSIONS

Analyses of linearized perturbations from a uniform mean flow have been carried out for three cases:

- (1) Flow past sinusoidal, traveling surface waves on a semi-infinite plate, and flow past more generalized "galloping" wall shapes which induce a neutral normal velocity along the plate which propagates at the freestream speed, $c=U_{\infty}$.
- (2) Flow with freestream disturbances encountering a semi-infinite plate. An example analysis of an oscillating vortex sheet convecting downstream is given, and references for many other vortical, irrotational, and mixed rotational/irrotational disturbances are cited.
- (3) Flow with surface waviness and with freestream disturbances is analyzed by adjusting the phase, x-wavenumber, phase speed, and amplitude(s) of the surface waviness or galloping.

The results for the first two cases clearly illustrate the upstream influence of the semi-infinite plate in this elliptic problem. The classical irrotational Kelvin-Helmholtz solution is recovered downstream of the leading edge, but an effect of the leading edge is to initiate a secondary flow. This secondary flow satisfies the impermeability condition on a flat plate. This secondary flow is also irrotational.

This secondary flow appears in the first two cases. However, for the superposed cases of freestream disturbances and wavy/galloping surfaces, the secondary flow is eliminated if the phase, x-wavenumber, phase speed, and amplitude(s) of the wavy or galloping surface are adjusted to those properties of the freestream disturbances.

As shown in Refs. 12,16, this secondary flow is composed of a superposition of exponentially-decaying standing waves downstream of the leading edge. Hence, the analyses of semi-infinite wavy walls show that the motion of the wall can excite this family of waves if a leading edge is present. Upstream of the leading edge, the flowfield around the leading edge induced by wall motion can be represented as a superposition of growing standing waves.

This analysis is based on linearized versions of the impermeability boundary condition at the wavy surface, and the mean flow is assumed to be uniform. Just as the Kelvin-Helmholtz solution, linearized steady and unsteady airfoil theories, and theories of uniform flows past (doubly infinite) compliant surfaces have had a useful role in the subsequent development of those subjects, the introduction of these assumptions in a first analysis is justified. Of course, such theories cannot account for effects in the boundary layer, but they may provide useful edge boundary conditions or solution forms for the boundary layer analyses. An example of this information is the recognition that a secondary flow arises as a result of the leading edge.

Wall motions that induce disturbances which propagate at the freestream speed were found analytically in Section 2, as essentially unchanged from Ref. 9. These analyses were carried out under the context of a uniform mean flow, where the usual sinusoidal wall motion traveling at speed U_∞ would not induce any disturbances since $U_\infty - c = 0$ in eqn. (2.3a). The reason that the case of $c = U_\infty$ is a useful case is that low-intensity vortical fluctuations in a viscous flow propagate at nearly that speed.

However, if a parallel-flow boundary layer were present and viscous effects were incorporated, then the linearized wall boundary conditions along the x-axis would be (e.g. Ref. 18)

$$u(x,0,t) = -\bar{U}_y(0)h_0$$

$$v(x,0,t) = ch_0$$

Hence, the effect of the mean boundary layer is to provide relative motion between the mean flow and the surface wave traveling at U_∞ . These boundary conditions indicate that disturbances are induced by a sinusoidal wave propagating at speed U_∞ if a mean boundary layer is present. Further examination of the boundary conditions for c near U_∞ is necessary to understand the relationship between the uniform flow, inviscid boundary condition and the viscous boundary conditions with a mean boundary layer as the Reynolds number becomes infinite and all viscous layers have a vanishing thickness.

In conclusion, the analyses for semi-infinite wavy walls show that the motion of the surface wave induces a secondary flow near the leading edge which is superposed on the classical Kelvin-Helmholtz solution for flow over a traveling wavy surface. This secondary flow is composed of a superposition of exponentially-decaying standing waves. When freestream disturbances are present, the corresponding secondary flow associated with the disturbances interacting with the leading edge can be eliminated if the phase, x-wavenumber, phase speed, and amplitude(s) of the wavy or galloping surface are properly adjusted. Further studies of these effects on boundary layers are warranted, and additional studies of traveling or galloping surface waves are needed when the phase speed is exactly or nearly the freestream speed.

REFERENCES

- 1a. Tsugé, Shunichi and Rogler, Harold L., "An asymptotic solution of the Orr-Sommerfeld equation based on a special coordinate stretching", Bull. American Physical Society, vol.25, no.9 (1980).
- 1b. —, "The two-dimensional, viscous boundary-value problem for fluctuations in boundary layers", AIAA-83-0044, AIAA 21st Aerospace Sciences Meeting, Reno, Nevada (10-13 January 1983).
2. Benjamin, T. Brooks, "The threefold classification of unstable disturbances in flexible surfaces bounding inviscid flows", J. Fluid Mechanics, Vol.16, p.436 (1963).
3. Lamb, H., Hydrodynamics, 6th Edition, Cambridge U. Press (1932).
- 4a. Ackeret, J., "Leiftkrafte and Flugel, die mit grosserer als Schallgeschwindigkeit bewegt werden", Zeitschrift fur Flugtechnik und Motorluftschiffahrt, vol.16, pp.72-74 (1925); translated as NACA-TM-317 (1925).
- 4b. —, "Uber Luftkrafte bei sehr grossen Geschwindigkeiten insbesondere bei ebenen Stromungen", Helvetica Physica Acta 1, pp.301-322 (1928).
5. Hosokawa, I., "Transonic flow past a wavy wall", J. Physical Society of Japan, Vol. 15, No. 11, pp.2080-2086 (1960).
6. Moore, F.K. and Gibson, W.E., "Propagation of weak disturbances in a gas subject to relaxation effects", Inst. Aero. Sci. Rep. no. 59-64 (1959).
7. Vincenti, Walter G., "Non-equilibrium flow over a wavy wall", J. Fluid Mechanics, Vol. 6, Part 4, pp.481-496 (November 1959).
8. Horlock, J.H., "An unsteady flow wind tunnel", Aeronautical Quarterly, Vol.25, pp. 81-90 (May 1974).
9. Rogler, Harold L., "Galloping, Wavy and Porous Wall Tunnels Which Introduce Irrotational Traveling-Wave, Unsteady Flows", FTAS/TR-76-119, Case Western Reserve University (June 1976).
10. Rogler, H., "Free-Stream Vorticity Disturbances Adjusting to the Presence of a Plate - A Quarter-Plane Problem", J. Applied Mechanics, Vol.44, No.4 (December 1977).
11. Landahl, Marten T., "On the stability of a laminar incompressible boundary layer over a flexible surface", J. Fluid Mechanics, Vol. 13, pp.609-632 (1962).
12. Rogler, Harold L., "Nonperiodic fluctuations induced by stationary surface waviness on a semi-infinite plate", AEDC-TR to be published (1983)
13. Abramowitz, Milton and Stegun, Irene A., Handbook of Mathematical

Functions, NBS Applied Math. Series 55 (March 1965).

14. Rogler, H., "The Interaction between Vortex-Array Representations of Freestream Turbulence and Semi-Infinite Flat Plates", J. Fluid Mechanics, Vol. 87, Part 3, pp. 583-606 (1978).
15. Rogler, Harold L. and Reshotko, Eli, "Rotational and Irrotational Freestream Disturbances Interacting Inviscidly with a Semi-Infinite Plate", AEDC-TR to be published (1983).
16. Rogler, Harold L. and Reshotko, Eli, "The excitation of growing and decaying standing waves", Bull. American Physical Society, vol.27, No.9 (1982).
17. Rogler, Harold L., "Unsteady, exponentially-varying standing waves in boundary layers", AIAA-83-0045, AIAA 21st Aerospace Sciences Meeting, Reno, Nevada (10-13-January).
18. Benjamin, B., "Shearing flow over a wavy boundary", J. Fluid Mechanics, Vol. 6, Part 2, pp.161-204 (August 1959).

END

FILMED

7-85

DTIC